# FLOATABILITY OF JAROSITES IN THE PRESENCE OF ANIONIC SURFACTANTS

by

Avery Payne

B.ASc., The University of British Columbia, 2015

A THESIS SUBMITTED IN PARTIAL FULFILLMENT OF

THE REQUIREMENTS FOR THE DEGREE OF

MASTER OF APPLIED SCIENCE

in

THE FACULTY OF GRADUATE AND POSTDOCTORAL STUDIES

(Mining Engineering)

THE UNIVERSITY OF BRITISH COLUMBIA

(Vancouver)

December 2018

The following individuals certify that they have read, and recommend to the Faculty of Graduate and Postdoctoral Studies for acceptance, a thesis/dissertation entitled:

Floatability of Jarosites in the Presence of Anionic Surfactants

submitted by Avery Payne in partial fulfillment of the requirements for the degree of Master of Applied Science in Mining Engineering

**Examining Committee:**

Dr. Marek Pawlik
Supervisor

Dr. Sanja Miskovic
Supervisory Committee Member

Dr. Maria Holuszko
Supervisory Committee Member

**Abstract**

Five jarosite samples were synthesized and their surface properties relevant to froth flotation were examined. Sodium jarosite, low-silver sodium jarosite (3.47 % Ag), high-silver sodium jarosite (12.84% Ag), potassium jarosite, and high-silver potassium jarosite (5.56% Ag) were synthetized in an autoclave. No significant differences in zeta potential characteristics [pH 2-10] were observed between the samples, with a common isoelectric point at pH 5.

Reagent adsorption and Hallimond tube (single mineral) flotation experiments were conducted with three anionic surfactants at pH 3.5 and at pH 10. The three reagents were: sodium laurate, sodium dodecyl sulfate, and octanohydroxamic acid. These surfactants represented different classes of flotation collectors: weak-electrolyte type (lauric acid and hydroxamic acid), strong-electrolyte type (dodecyl sulfate), highly soluble in water (dodecyl sulfate and hydroxamate) and poorly soluble in water (lauric acid).

The experimental results were analyzed in terms of correlations between zeta potential, surfactant adsorption, and flotation results in order to enhance the fundamental understanding of surfactant-jarosite interactions. It was found from the adsorption and flotation results that the floatability of jarosites in the presence of the tested reagents followed two main trends. For several jarosite-reagent-pH combinations, the floatability of the mineral increased steadily with the increasing adsorption density of the reagent. In other cases, a minimum concentration of the reagent was required to initiate flotation even though the adsorption density of the surfactant continuously increased. It was postulated that in the latter case, the transition from poor to good flotation coincided with a change in the adsorption mechanism of the surfactant, while in the former case, one mechanism dominated the interaction. It was concluded that the adsorption of the anionic surfactants was driven by chemical interactions with iron sites on the jarosite surfaces regardless of the jarosite type. When analyzing the adsorption data, it was recognized that the jarosite surface at pH 10 was coated by a goethite (FeO(OH)) layer, while at pH 3.5 the surfactants adsorbed on a clean jarosite surface. No systematic trends were observed as a function of the silver content. Based on all the data, recommendations on the most promising flotation conditions were also made.

## Lay Summary

The term "jarosite" refers to a group of minerals that form during high-pressure acid leaching of base and precious metal ores. The general formula of jarosite can be given as $MFe_3(SO_4)_2(OH)_6$, where M can be a number of metal cations, including silver (Ag). The formation of jarosite in hydrometallurgical systems often results in deportment of silver to this secondary mineral phases. In order to avoid such losses of silver, a need arises to develop a process that could recover the silver-bearing jarosite minerals. It is hypothesized that a froth flotation approach should be an attractive solution. Therefore five jarosite minerals with varying amounts of silver were synthesized, and their surface properties examined to better understand their flotation properties in the presence of three selected surfactants. The experimental program involved reagent adsorption, small scale flotation, and surface charge measurement under a range of conditions. Recommendations on reagent selection were also made.

## Preface

This dissertation is original, unpublished, independent work by the author, A. Payne.

## Table of Contents

## List of Tables

## List of Figures

**Acknowledgements**

A big thanks to Dr. Pawlik, Dr. Ji, and Eldorado Gold for providing me with this opportunity. I owe particular thanks to Dr. Pawlik for his academic guidance, as well as his patience and support through this extended process. I would also like to thank Sally Finora for assistance with all lab related questions.

I would like to thank everyone who has been there for me during this time as it has been an exceptionally difficult process. Special thanks are owed to my parents for their emotional and financial support over these years and to Kira for giving me the determination I needed to finish through her unwavering love and support.

## 1.0 Introduction and Research Objectives

The general objective of this thesis was to investigate the potential of froth flotation for the separation of silver jarosite [$AgFe_3(SO_4)_2(OH)_6$] from leaching residues. The formation of jarosite in hydrometallurgical systems often results in deportment of silver to those secondary mineral phases. In order to avoid such losses of silver, a need arises to develop a process that could recover metal values from leaching residues by targeting the silver-bearing jarosite minerals. It is hypothesized that a froth flotation approach should be an attractive solution. The only areas of research surrounding recovery of lost silver in jarosite residues is through a two stage process consisting of breaking down the jarosite compounds followed by recovery of the liberated silver. Many of these methods are not economically viable in an industrial setting due to their high operational costs (Mukherjee et al. 2016). A direct flotation process is viewed by many as the most effective solution for the problem, but a full scale application does not exist at present (Han et al, 2014). One of the main obstacles is the identification of appropriate surfactants to render silver jarosite sufficiently hydrophobic for flotation. That step, however, requires a thorough understanding of the surface properties of the target mineral, and so far no systematic studies have been published on the fundamentals of jarosite flotation.

For the purposes of this thesis the following five jarosite samples were synthesized in a Parr Autoclave: Sodium jarosite, low-silver sodium jarosite (3.47 % Ag), high-silver sodium jarosite (12.84% Ag), potassium jarosite, and high-silver potassium jarosite (5.56% Ag)). Characterization of the jarosite samples was performed by scanning electron microscopy (SEM) coupled with elemental surface mapping using energy-dispersive X-ray spectroscopy (EDX). The surface charge of the jarosite particles was determined through measurements of zeta potential distributions based on the micro-electrophoretic technique. Particle size analysis was carried out on the Malvern Mastersizer 2000 and the surface area was determined by the Quantachrome Autosorb-1. Surfactant adsorption and Hallimond tube flotation experiments were conducted with three chemical surfactants at an unadjusted pH of 3.5 and pH 10. The amount of surfactants adsorbed on the jarosite particles was measured from total organic carbon contents in the aqueous phase before and after contacting with jarosite particles.

The three tested surfactants were: A sodium salt of lauric acid, sodium dodecyl sulfate, and octanohydroxamic acid. Lauric acid is a fatty acid. Fatty acids are commonly used as

collectors for salt-type, sulfate minerals and was selected as a representative of this group. Lauric acid is a weak electrolyte collector (similar to hydroxamate but in contrast to dodecyl sulfate) with low solubility (in contrast to both hydroxamate and dodecyl sulfate). In this case speciation is a function of pH and the low solubility may lead to precipitation of lauric acid. This is the most complex case. Dodecyl sulfate was selected due to the common sulfate anion. The assumption being that the sulfate group will show strong adsorption affinity towards the jarosite surface. Dodecyl sulfate is a strong electrolyte with high solubility in water, whose speciation is independent of pH. In other words, it is always 100% dissociated and does not form colloidal precipitates. This is the simplest case. Lastly, a hydroxamate was chosen due its popularity as a collector for non-sulfide minerals containing heavy metals. Hydroxamate is a weak electrolyte collector with high solubility. So in contrast to dodecyl sulfate, its' speciation is a function of pH, but (similar to dodecyl sulfate) the solubility is still high enough to prevent precipitation. This is a more complex case than dodecyl sulfate.

Considering the available literature data on the froth flotation of jarosites, especially silver jarosites, this research aims to characterize the fundamental surface properties of jarosite minerals relevant to the froth flotation process. Of primary interest are the surface charge characteristics of jarosites, and the flotation response of Ag-jarosites to selected surfactants. The specific objectives of this research can be summarized as follows:

1) To characterize the surface charging properties of the tested jarosites as a function of pH.
2) To determine the adsorption behavior of several anionic surfactants as collectors of jarosites.
3) To identify the most promising collectors among the tested surfactants.
4) To assess the floatability of the jarosite samples as a function of pH and reagent type.
5) To determine the effect of substitution by silver in the jarosite crystal on the surface properties of jarosites.

## 2.0 Literature Review

### 2.1 Jarosite Compounds

Jarosite minerals belong to the alunite super-group, which contains over 40 minerals. The general formula of an alunite mineral is $MG_3(TO_4)_2(OH,H_2O)_6$, where M represents a cation, G, an octahedral occupation site, and T a tetrahedral occupation site. The alunite super-group is characterized by G-site occupation by $Fe^{3+}$ or $Al^{3+}$ ions (Najorka et al, 2016). Alunite minerals are layered structures containing corner connected central octahedral sites with tetrahedral sites located above and below, and the M cations packed between the layers (Smith et al, 2006; Brand et al, 2012). When the G-site of an alunite mineral is dominated by $Fe^{3+}$, the mineral is referred to as jarosite. All jarosite minerals contain sulphur in the T-site. Jarosite minerals have rhombohedral symmetry and hexagonal cell parameters with similar unit cell dimensions (Dutrizac & Kaiman, 1976; Brand et al, 2012). Having hexagonal unit cell parameters means that the unit cell of jarosite has dimensions $a = b \neq c$. Table 2-1 lists the unit cell dimensions of various jarosite minerals (Dutrizac & Jambor, 2000).

Table 2-1: Hexagonal Cell Dimensions for Various Jarosite Species (Dutrizac & Jambor, 2000).

| Species | a-dimension (Å) | C-dimension (Å) |
|---|---|---|
| Potassium Jarosite | 7.29 | 17.19 |
| | 7.32 | 17.13 |
| | 7.30 | 17.27 |
| Sodium Jarosite | 7.31 | 16.62 |
| | 7.33 | 16.70 |
| | 7.34 | 16.75 |
| Silver Jarosite | 7.35 | 16.55 |
| | 7.35 | 16.58 |
| | 7.34 | 16.56 |

The crystal structure of jarosite is shown along the a-dimension in Figure 2-1 and along the c-dimension in Figure 2-2. Figure 2-3 shows co-ordination of the M-site in the crystal structure.

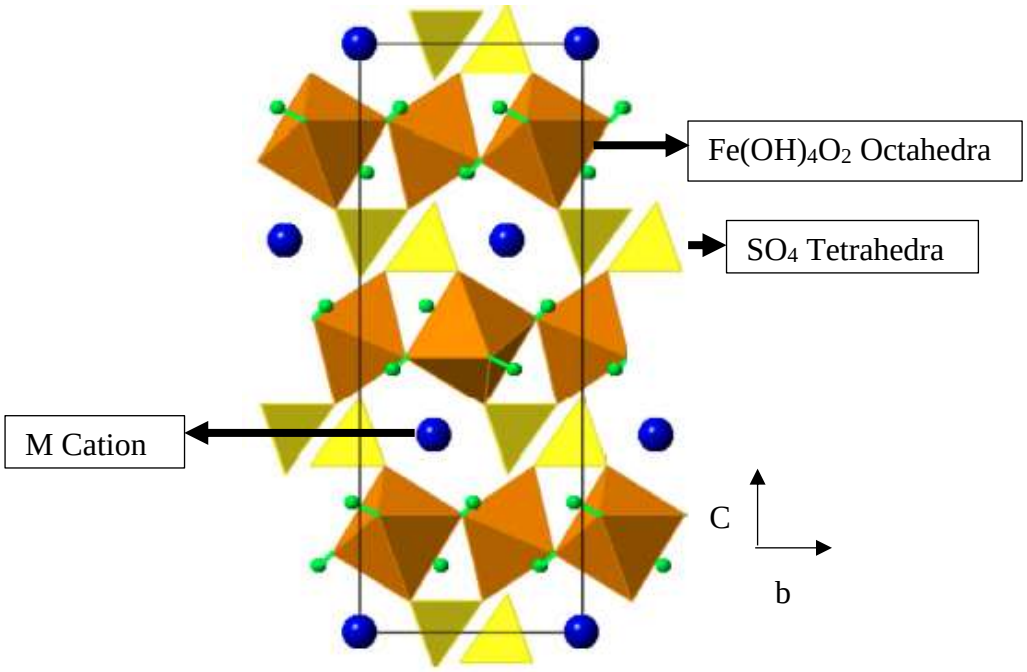


Figure 2-1: Crystal Structure of Jarosite Group Along a-dimension (© Najorka et al, 2016, by permission).

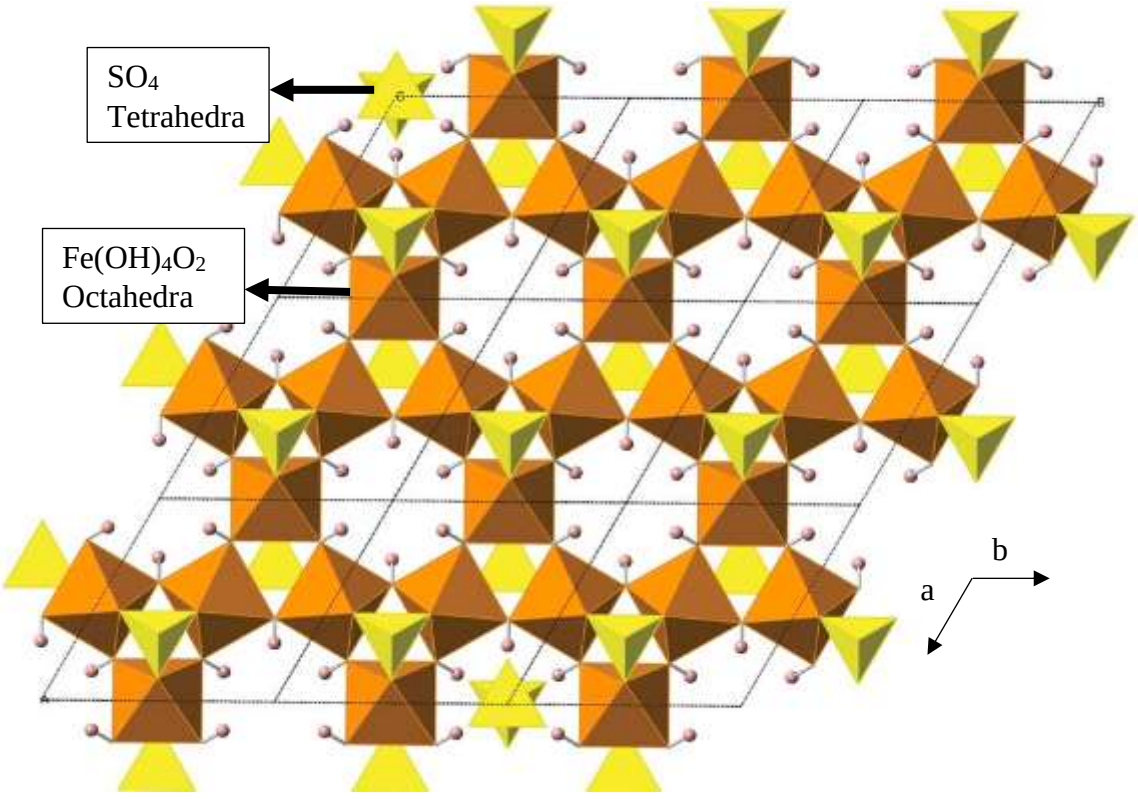


Figure 2-2: Crystal Structure of Jarosite Group Along c-dimension (© Mills et al, 2013, by permission).

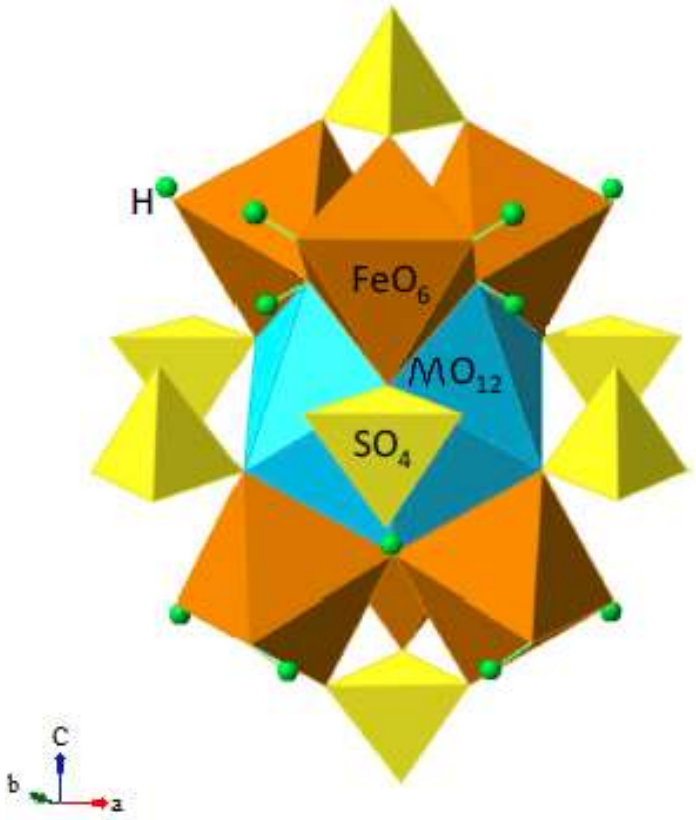


Figure 2-3: Jarosite M-site Location in the Crystal Structure (© Najorka et al, 2016, by permission).

The general formula of a jarosite mineral is $MFe_3(SO_4)_2(OH)_6$, where M represents a metal cation as shown in Table 2-2 (Grey et al, 2013; Najorka et al, 2016).

Table 2-2: Jarosite Minerals (Dutrizac & Jambor, 2000).

| Formula | Natural Mineral Name | Synthetic Mineral Name |
|---|---|---|
| $KFe_3(SO_4)_2(OH)_6$ | Jarosite | Potassium Jarosite |
| $NaFe_3(SO_4)_2(OH)_6$ | Natrojarosite | Sodium Jarosite |
| $RbFe_3(SO_4)_2(OH)_6$ | - | Rubidium Jarosite |
| $AgFe_3(SO_4)_2(OH)_6$ | Argentojarosite | Silver Jarosite |
| $(NH_4)Fe_3(SO_4)_2(OH)_6$ | Ammoniojarosite | Ammonium Jarosite |
| $TlFe_3(SO_4)_2(OH)_6$ | Dorallcharite | Thallium Jarosite |
| $PbFe_6(SO_4)_4(OH)_{12}$ | Plumbojarosite | Lead Jarosite |
| $HgFe_6(SO_4)_4(OH)_{12}$ | - | Mercury Jarosite |
| $Pb(Fe,Cu)_3(SO_4)_2(OH,H_2O)_6$ | Beaverite | Lead-copper Jarosite |
| $(H_3O)Fe_3(SO_4)_2(OH)_6$ | Hydronium Jarosite | Hydronium Jarosite |

## 2.2 Formation of Jarosite

Jarosite is formed in sulfide-rich, acidic, oxidizing, iron rich environments (Smith et al, 2006; Najorka et al, 2016). Jarosite formation takes place through the following hydrolysis reaction (Dutrizac, 1983):

$$M_2SO_4 + 3Fe_2\left(SO_4\right)_3 + 12H_2O \rightarrow 2MFe_3\left(SO_4\right)_2\left(OH\right)_6 + 6H_2SO_4 \qquad (2.1)$$

Jarosite minerals are commonly found in weathered zones of sulfide ore deposits. It is however, in acidic soils, such as mine drainage, where the majority of natural jarosite is found (Jones et al. 2018). Jarosite formation can be attributed to a variety of sources such as acid mine drainage, sulfide oxidation, and volcanic alteration (Elwood Madden et al, 2004).

### Natural Jarosite Deposits

The earliest documented mining of argentojarosite occurred in Rio Tinto, Spain during the Roman Empire. It is estimated that nearly 2 million tonnes of an argentojarosite ore was mined during this time. Elsewhere, the Incas mined both argentojarosite and plumbojarosite in Matagente, Peru prior to Spanish invasion (Dutrizac & Jambor, 2000). The first modern day investigation of argentojarosite took place at the Tintic Standard Mine in Dividend, Utah in 1922. A fault containing a yellow streak of finely disseminated, high-grade silver material was discovered and examined. It was believed that silver sulfide had been dissolved in a solution of ferric sulphate in order to form this new mineral (Schempp, 1923).

Jarosite deposits in the Warkalli Formation; located in Kerala, South India; have been extensively studied by Singh et al (2016). Characterization of the formation has been carried out by hyperspectral analysis, X-ray diffraction, Fourier transform infra-red reflectance, electron probe microanalysis, and laser Raman spectroscopy. Other deposits containing naturally forming jarosite minerals include, but are not limited to: The Golden Deposit in Canada's Northwest Territories (Frederick & Everdingen, 1987), the Veladero Deposit in the El Indio-Pacua Belt of Argentina (Holley et al, 2016), along the Iberian Pyrite Belt that stretches from

Portugal to Spain (Velasco et al, 2013), the Vera Epithermal gold deposit in Australia (Murphy & Gilkes, 2010), the Kerman copper belt in southeastern Iran (Zadeh et al, 2014), the Bahariya iron deposits in the Bahariya Oasis of Egypt (Dabous, 2002), and the Lerokis and Kali Kuning deposits on Wetar Island, Indonesia (Sewell & Wheatley, 1994).

Jarosites on Mars

A recent spike in jarosite interest has been brought on by the discovery of jarosite on Mars by the MER rover Opportunity. The mineral is widely recognized as a key indicator of previous water on the Martian planet (Brand et al, 2012) since water is required for jarosite formation (Elwood Madden et al, 2004). Both K-Na-$H_3O$ jarosites as well as $H_3O$, Fe-deficient jarosites were discovered.

## 2.3 Jarosites in Hydrometallurgy

When processing a variety of sulfide ores, primarily sphalerite (ZnS), a high amount (5-12%) of iron is usually present. This iron is problematic as it can interfere with the recovery of zinc during processing. Jarosite minerals form during the process of precipitating this unwanted iron out of solution (Arregui et al, 1979; Dutrizac & Jambor, 2000).

Zinc sulfide ores undergo roasting, oxidizing most of the zinc to zinc oxide (ZnO), with a fraction combining with oxidized iron to produce zinc ferrite ($ZnO\text{-}Fe_2O_3$). The material then undergoes a sulfuric acid leach, dissolving the zinc oxide and forming zinc sulfate ($ZnSO_4$), which can easily be recovered through purification and electrolysis. This process leaves the zinc ferrite untreated. In order to recover this lost fraction, the remaining residue is put through a hot, concentrated sulfuric acid leach which dissolves the zinc ferrite. Iron is then precipitated out of solution through the formation of jarosite (Dutrizac & Jambor, 2000). Jarosite forms quickly when an alkali metal, usually sodium, is introduced into the warm, acidic system and settles rapidly and is easily filterable (Gonzalez-Ibarra et al, 2016). Since zinc does not form a jarosite compound it remains in solution and is recycled in the system to be recovered upstream (Dutrizac & Chen, 2004).

The jarosite precipitation method is the cheapest method of iron removal and yields a high recovery of zinc (Dutrizac & Jambor, 2000). It is the most widely adopted method for zinc production via hydro metallurgy in the world, with hydro-metallurgical methods accounting for 85% of zinc production (Mombelli et al., 2018). In addition to zinc hydrometallurgy, jarosite precipitation has been used in flowsheets of nickel, cobalt, copper, and uranium (Dutrizac & Jambor, 2000).

A secondary use of the jarosite precipitation method is during the processing of refractory sulphide gold ores, such as gold-bearing pyrite ($FeS_2$) deposits, as an intermediary step for the removal of lime-consuming basic iron sulphate (BFS). Gold cannot be recovered via conventional leaching from these refractory ores. This material is subjected to pressure oxidation at high temperatures (190$^oC$) in order to avoid elemental sulphur formation. Iron is dissolved into solution as ferrous sulphate ($FeSO_4$) and then oxidized to ferric sulphate ($Fe_2(SO_4)_3$), from which iron precipitates out either as; hematite ($Fe_2O_3$), BFS ($FeOHSO_4$), or jarosite. Following pressure oxidation, the precipitate would typically undergo a neutralization stage, where the pH would be increased for cyanidation. However, BFS consumes a large amount of lime ($Ca(OH)_2$), which is costly. It is therefore advantageous to have a "hot cure" between these stages. This "hot cure" uses highly acidic conditions and temperatures <140$^oC$ in order to dissolve the BFS back into solution as ferric sulphate, which in the presence of jarosite-forming metal ions, will now form a jarosite precipitate (Gunaratnaam et al, 2018).

### 2.3.1 Limitations of the Jarosite Method

The jarosite method of removing unwanted iron is not without flaws. Industrially produced jarosite poses a significant environmental threat due to the presence of toxic heavy metals, such as arsenic (As), cadmium (Cd), chromium (Cr), and lead (Pb) (Riley et al., 2018), and produces an enormous mass of material to be stored in waste disposal facilities (Bedi et al., 2018). The process can also incorporate valuable metals, such as silver, in waste streams (Dutrizac & Jambor, 2000). For every 150 tonnes of metallic zinc it is estimated that 125 tonnes of jarosites are produced (Smeaton, 2012). In 2007 it was reported that a total of 2.5 million tonnes per year (MT/y) of jarosite was produced in the world (Asokan, 2007) with China alone producing >1 MT/y of jarosite residue (Ju et al, 2011; Liu et al, 2016). The world leaders of

jarosite generation, in no particular order, are China, Canada, USA, Japan, Australia, Spain, Holland, France, Yugoslavia, Korea, Brazil, Mexico, Norway, Germany, Argentina, Belgium, and India (142,000 T/y) (Pappu et al, 2007; Pappu et al, 2011).

During jarosite precipitation, other dissolved ions, besides the added metal cation can form stable jarosite minerals. Prior to jarosite precipitation any silver-bearing minerals, such as silver sulfide ($Ag_2S$), will be oxidized, releasing silver ions into solution. The aqueous silver may be precipitated out of solution by the formation of silver jarosite ($AgFe_3(SO_4)_3(OH)_6$). Silver precipitation occurs more rapidly than iron during this process, which leads to silver encapsulation in the structure. Due to this encapsulation, extraction via cyanidation of residues is ineffective (Bolorunduro et al., 2003). The major silver losses associated with the jarosite method are due to the substitution of silver into the structure of natro/plumbojarosite ($(Na/Pb)Fe_3(OH)_6(SO_4)_2$). No successful methods have been developed to avoid these silver losses while precipitating iron (Dutrizac & Jambor, 1987; Gonzalez-Ibarra et al, 2016). This lost silver cannot be recovered by leaching due to its association with other elements (Gonzalez-Ibarra et al, 2016). In the presence of silver a mixture of multiple M-site jarosites (K or Na with Ag and $H_3O^+$) is formed within individual particles during jarosite precipitation. Hydronium jarosite is always present in some quantity during precipitation (Dutrizac & Jambor, 1987; Cogram, 2016).

### 2.3.2 Handling of Jarosite Residues

Jarosite waste is classified by the European Waste Catalogue as a hazardous waste (Mombelli et al, 2018) and is typically stored in geo-membrane lined tailings ponds due to toxic elements, such as arsenic, cadmium, lead, and zinc (Hage & Schuiling, 2000; Liu et al, 2016). These tailings ponds require large areas of land (Han et al., 2014) and, due to the liners limited life span, can begin leaking pollutants into the surrounding groundwater (Hage & Schuiling, 2000; Mombelli et al, 2018). Because of the high concentrations of metals as well as the low pH, the failure of a jarosite waste facility would be detrimental to any downstream ecological populations (Riley et al, 2018). Hage and Schuiling (2000) cited a zinc plant in the Budelco, Netherlands, in the year 2000, that had four jarosite ponds, two of which were leaking. Two other methods for the storage of jarosite residues are deep-ocean deposition and mountain

burial. These methods of disposal are viewed unfavourably due to the associated environmental concerns. From 1973 to 1997 it is reported that Pasminco EZ Metals disposed of 4 million tonnes of jarosite residue with significant concentrations of lead and arsenic off the coast of Tasmania at a depth of 2000 meters (Gwyther, 2004; Smeaton, 2012). In Odda, Norway it was reported that disposal of jarosite residues in a granite mountain cave resulted in seepage and contamination of the area (Smeaton, 2012). Due to the temporary nature of jarosite residue storage solutions, worldwide disposal of jarosite residues has come to the forefront of environmental concerns (Mombelli et al, 2018).

Methods of jarosite destruction, as opposed to storage, include a fuming furnace process and bioleaching, such as myconanomining (fungal mediated bioleaching and conversion of bulk metallic elements into nanostructures) (Bedi, 2018), and most recently, through the use of an arc transferred plasma reactor (ATP) (Mombelli et al., 2018). In the fuming furnace process, jarosite residues are mixed with coal and subjected to temperatures over 1000$^{o}$C. Zinc and lead turn into a metal vapour and simultaneously oxidize to oxide dust. This process is extremely costly (Liu et al, 2016). In the ATP process, jarosite residue is dried and calcined at 1000$^{o}$C before being reduced at 1600-1700$^{o}$C in the ATP reactor (metallurgical coke as a reducing agent + limestone, $CaCO_3$, as flux) to produce a metallic magnetic fraction (cast iron), a non-magnetic fraction (slag – Si, Al, Na, Ca), and a dust fraction (Zn, Pb, Ag). The slag produced is a glassy structure, which is inert to leaching and can be safely disposed of. (Mombelli et al., 2018).

Lastly, alternative uses for jarosite waste were also investigated, mainly for use in the construction industry. For example, when mixed with 10% lime, jarosite has demonstrated strength surpassing requirements for certain building usages in cold climates with constant freeze/thaw cycles (Gupta, & Prasas, 2018). It has also been used as a substitute for gypsum in cement production (Katsioti et al, 2005), and mixed with granite to produce a glass type material (Pelino, 2000). Hage and Schuiling (2000) investigated pressure reduction of jarosite residues into immobile oxides using a cellulose type material in an autoclave for use in construction. This process was initially developed in the Brite Euram Program of the European Community in 1998 and involves autoclaving residues at 250$^{o}$C for 10 minutes, using the sewage sludge as a means of gaining energy and creating a reducing environment. The process results in a solid containing iron and metal oxides (hematite, magnetite, anglesite, galena), with

sulfate being dissolved. Solid-liquid separation is required due to the liquid containing toxic elements that need to be treated. Test-work of this process revealed that, while successful in treating jarosite residues and eliminating many toxic elements, the product still did not meet construction industry standards (Hage & Schuiling, 2000). Smeaton (2012) reported on a technology, called Jarofix, developed alongside the Canadian government, which utilizes Portland cement, lime, and water to produce a compound that has long-term stability.

## 2.4 Jarosite Synthesis - Methods and Conditions

Sasaki and Konno (2000) listed 3 different methods for potential jarosite synthesis (Table 2-3). The first, most efficient, and prominently used method in a laboratory setting is conducted by heating iron sulfate, and an alkali metal sulfate under acidic conditions for a temperature dependent length of time. Most literature revolving around this method comes from research Dr. J.E. Dutrizac and his coworkers. Methods II and III require lengthy aging periods of >100 days.

Table 2-3: Jarosite Synthesis Methods (Sasaki & Konno, 2000).

| Method | Description |
|---|---|
| I | Heating of iron (III) sulfate, and an alkali sulfate under acidic conditions. Synthesis time varies on temperature (~1-15 hours). |
| II | Thiobacillus ferrooxidans used to oxidize $Fe^{2+}$ ions in a gas-permeable Erlenmeyer flask (~56 days) at 30$^{o}$C and pH 2. An alkali salt is then added and aged for 168 days under similar conditions (Jones et al., 2018) |
| III | Chemical oxidation of $Fe^{2+}$ ions by addition of $H_2O_2$ |

Dutrizac (1984) listed the major conditions affecting the synthesis of jarosite under method I as: temperature, pH, iron concentration, alkali metal cation concentration, and reaction time. These will be discussed in detail below since method I was used for the preparation of jarosite samples in this thesis. It was also established that a minimum amount of agitation and mixing is necessary to precipitate jarosite. During precipitation, rotational speeds above 400 rpm were found to increase jarosite formation, with further increases having little effect. Baffles in lab-scale autoclaves were found to produce satisfactory mixing conditions (Dutrizac, 1983). Basciano (2008) and Grey et al (2013) stated that even in pure jarosite synthesis there is always

a level of hydronium ($H_3O^+$) substitution in the cation M-site, particularly at temperatures exceeding 100$^o$C (Jones et al, 2018), creating a complete solid solution. Najorka et al (2016) listed hydronium substitution in their synthesized jarosite sample to be 0.36 atoms per formula unit and Alpers et al (1989) observed jarosite residues containing between 10-32% of hydronium jarosite. If synthesized jarosite is not excessively washed it will almost certainly contain residual acid (Gunaratnam et al, 2018). Jarosite suspensions have an equilibrium pH of ~3.9, and due to their amphoteric nature, will gradually produce acidic pH values even when placed in a basic solution (Sadowski et al, 2001).

Jarosite Seeding

It was found that the precipitation of jarosite could be accelerated through seeding (Dutrizac, 1996). Dutrizac (1999) showed that the rate of precipitation increased linearly with seed addition and that seeding increased the range of temperatures and pH that precipitation occurred at. He also showed that any jarosite species could be used in the seeding process, with no effect on the resulting jarosite formed. The majority of commercial operations that employ the jarosite method use seeding (Dutrizac, 1999). The seeding process also produces jarosite that is coarser and filterable. The use of seeding, however, cannot increase the maximum amount of iron precipitated. If given a long enough timeframe, seeding ultimately has no effect on the amount of iron precipitated, merely speeding up the initial period of precipitation (Dutrizac 1996).

Temperature

Dutrizac (1983) found that higher temperatures leads to increased yields of sodium jarosite, up until 130$^o$C. He believed the largest impact of temperature on precipitation is from 70 to 110$^o$C (Dutrizac 1996). However, Dutrizac and Kaiman (1976) discovered when precipitating silver jarosite, if temperatures fell below 140$^o$C, hydronium substitution began to occur, leading to lower silver values. At 97$^o$C Dutrizac (1983) established that jarosite yield increases up until a reaction time of 15 hours with little change after that point. He states that synthesis can be sped up to a 1 hour equilibrium at 140$^o$C.

Grey et al. (2013) showed that jarosite synthesis performed at elevated temperatures (140$^{o}$C+) produces crystalline and stoichiometric samples and those that are conducted at temperatures below 100$^{o}$C are increasingly iron deficient, with the excess negative charge being balanced by replacement of $OH^-$ by $H_2O$. The structure however remains rhombohedral.

pH

Dutrizac (1983) discovered that the precipitation of jarosite was retarded by increasing concentration of acids, with little to none jarosite formed above 0.5 M $H_2SO_4$. Dutrizac (1996) stated that in the absence of seeding no jarosite will be formed below pH 1.0 and that other compounds begin to form above pH 2.0. With seeding, he was able to extend the range of precipitation pH down to 0.6. Dutrizac (1983) stated that pH plays no role in which M-site cation will precipitate out as a jarosite mineral if competing ions exist.

Metal Cation Concentration

The presence of specific metal cations is the decisive factor of which jarosite mineral will precipitate. Dutrizac (1983) found that at 97$^{o}$C jarosite yield increases until twice the required stoichiometric amount of alkali metals are present. Dutrizac (1996) later stated that at an iron concentration of 0.3 M, sodium jarosite precipitation increases until a concentration of 0.3 M of $Na_2SO_4$, after which further increases have a negative effect. The presence of non-jarosite forming metal cations plays no role in jarosite composition or yield (Dutrizac 1983).

Pure Sodium Jarosite Synthesis

Dutrizac and Kaiman (1976) prepared sodium jarosite with a 1 L solution of 64 grams sodium sulfate (0.451 M $Na_2SO_4$), 10 grams ferric ions ($Fe^{3+}$) introduced as ferric sulfate (0.09 M $Fe_2(SO_4)_3$), and 0.01 M sulfuric acid ($H_2SO_4$). The solution was heated to 95$^{o}$C for 1.5-3 hours before being filtered, washed, and dried with acetone.

Dutrizac (1996) demonstrated that low ferric iron concentrations of < 0.035 M lead to low precipitation of sodium jarosite and that raising concentrations above 0.15-0.4 M begins to have negative effects on the results (0.2 M sodium sulfate).

Dutrizac (1999) prepared sodium jarosite in a 1 L solution of 0.3 M iron sulfate, 0.3 M sodium sulfate, and an initial pH of 1.5. The solution was heated to 98$^{o}$C for 7 hours before being filtered, rinsed, and dried.

Dutrizac (2004) listed the ideal conditions for sodium jarosite synthesis to be 0.3 M $Fe_2(SO_4)_3$, 0.2 M $Na_2SO_4$, and an initial pH of 1.6 (modified with $H_2SO_4$).

Pure Potassium Jarosite Synthesis

Dutrizac and Chen (2004) synthesized potassium jarosite with 0.3 M ferric iron ($Fe^{3+}$), 0.2 M potassium sulfate ($K_2SO_4$), and an initial pH of 1.60 (adjusted with $H_2SO_4$). These concentrations were listed as near ideal conditions for potassium jarosite synthesis.

Dutrizac and Kaiman (1976) synthesized potassium jarosite with a 1 L solution of 30 g/L (0.3 M) potassium nitrate ($KNO_3$), 8 g/L (0.14 M) of ferric iron ($Fe^{3+}$) as ferric sulfate ($Fe_2(SO_4)_3$), and 0.01 M $H_2SO_4$. The solution was heated to 95$^{o}$C for 1.5-3 hours before being filtered, washed, and dried with acetone.

Pure Silver Jarosite Synthesis

Silver jarosite synthesis was first attempted by Fairchild in 1933. Fairchild (1933) prepared solutions of silver sulfate ($Ag_2SO_4$) in 0.75-1.5 M $H_2SO_4$. A 1:3 molar ratio of silver sulfate to iron sulfate was used and the solutions were heated to 110-200$^{o}$C in a sealed tube for three days. This procedure produced poor results with only small amounts of silver jarosite. It was later established that the high acid concentration used by Fairchild led to these poor results (May et al, 1973).

May et al (1973) were able to produce results with better yields of silver jarosite. 0.0244 M of silver sulfate ($Ag_2(SO_4)_2$) was added to 430 mL of boiling water. 63 mL of hot 0.5 M iron sulfate ($Fe_2(SO4)_3$ along with 5.7 mL of 17.6 M $H_2SO_4$ were added to the solution. These values equate to total test concentrations of 0.063 M $Fe_2(SO_4)_2$, 0.021 M $Ag_2SO_4$, and 0.2 M $H_2SO_4$. The mixture was kept at 97$^o$C for 200 hours before being filtered, washed, and dried over anhydrous calcium sulfate.

A procedure requiring less time was recorded by Dutrizac and Kaiman (1976). They used 20 g/L (0.064 M) silver sulfate, 20 g/L (0.36 M) $Fe^{3+}$ as ferric sulfate, and 25 g/L (0.25 M) $H_2SO_4$. The 1 L solution was heated to 140$^o$C for 2 hours before being filtered, washed, and dried with acetone. The silver content was increased from 17.1% (May et al., 1973) to 18% in the final jarosite product. The lower synthesis time and higher silver content can be attributed to the higher temperature used.

Roca et al (1993) synthesized silver jarosite by heating 0.3 M $Fe_2(SO_4)_3$, 0.048 M $Ag_2SO_4$, and 0.01 M $H_2SO_4$ in 1 L at 97$^o$C for 24 hours. The synthesized silver jarosite had the following formula: $Ag_{0.78}(H_3O)_{0.22}Fe_3(SO_4)_2(OH)_6$.

Silver precipitation as argentojarosite is, on its own, not very significant. It is, however, enhanced in the presence of another jarosite mineral when it begins to rapidly co-precipitate (Gunaratnam et al., 2018).

Combined Jarosite Precipitation

Dutrizac and Jambor (1987) conducted sodium-silver jarosite synthesis at 97, 130, and 150$^o$C in order to determine the inclusion of silver into sodium jarosite. Solutions of 0.2 M iron sulfate, and 0.06 M of sodium + silver sulfate at pH 1.6 were heated for 24 hours before being filtered and dried. The concentrations of sodium and silver sulfate were varied but always kept at a total of 0.06 M. Results showed a complete solid solution forming between silver and sodium jarosite. During the synthesis of a multi-species jarosite, the silver bearing phase precipitated before the sodium/potassium jarosite phase (Sasaki & Konno, 2000).

Patino et al (1998) synthesized a sodium-silver jarosite containing 0.115% Ag by heating 0.2 M $Fe_2(SO_4)_3$, 4.8 x $10^{-4}$ M $Ag_2SO_4$, 0.3 M $Na_2SO_4$, and 0.01 M $H_2SO_4$ in a total volume of 1 L, at 97°C for 24 hours. The synthesized jarosite had the following formula: $Na_{0.675}Ag_{0.005}(H_3O^+)_{0.32}Fe_3(SO_4)_2(OH)_6$.

Cruells et al (2000) synthesized a potassium-silver jarosite containing 0.135% Ag by heating 0.2 M $Fe_2(SO_4)_3$, 1.44 x $10^{-3}$ M $Ag_2SO_4$, 0.3 M $K_2SO_4$, and 0.01 M $H_2SO_4$ in a total volume of 1 L, at 97°C for 24 hours. The synthesized jarosite had the following formula: $K_{0.91}Ag_{0.007}(H_3O)_{0.083}]Fe_3(SO_4)_2(OH)_6$.

## 2.5 Recovery of Valuable Minerals from Jarosite

The only areas of research surrounding valuable metal recovery from jarosite residues is through a two stage process consisting of the breaking down of jarosite compounds followed by recovery of liberated material by leaching (Ju et al, 2011; Challa-Choque et al, 2016; Liu et al, 2016), flotation (Han et al, 2014), or cyanidation (Gonzalez-Ibarra et al, 2016). Many of these methods of silver recovery from jarosite residues are not economically viable in an industrial setting due to their high operational costs (Mukherjee et al, 2016). A single stage flotation process is viewed by many as the most effective solution for the problem, but little research on the topic has been conducted (Han et al, 2014).

Liu et al (2016) listed the optimal conditions for sulphuric acid roasting of jarosite to be; $H_2SO_4$/jarosite ratio of 0.36 by weight, 250°C roasting for 30 minutes followed by 1 hour of leaching at 50°C with a liquid-solid ratio of 4:1. Silver recovery was recorded as 61.3%. The increase in metal extraction above 250°C was found to be small while the amount of released sulfur dioxide ($SO_2$) gas during the process still increased.

Han et al (2014) examined the roasting of jarosite compounds followed by sulfidization flotation. Roasting of the residue took place at 600-700°C in order to release the encapsulated valuable minerals. Silver was transformed to silver sulfate which was easily sulfidized (activated) with sodium sulfide ($Na_2S$) to form a silver sulfide layer on the surface, modified to pH 5-6 with sodium carbonate ($Na_2CO_3$) or sulfuric acid, and recovered in a 3 stage froth flotation process using ammonium dibutyl dithiophosphate ($C_8H_{19}O_2PS_2$),

diethyldithiocarbamate ($C_5H_{10}NS_2$), and 2-mercaptobenzothiazole ($C_7H_5NS_2$). Silver recoveries of 81.6% were achieved with final concentrate grades of 1300 g/t.

Challa-Choque et al (2016) examined the decomposition of jarosite minerals followed by leaching of silver using thiourea. Leaching took place in acidic pH at 90°C. The process was able to recover 70-90% of silver depending on if leaching was carried out simultaneously with, or as a separate step to decomposition. Two separate steps typically offered better results. Thiourea was selected as a lixiviant due to its increased silver leaching kinetics in comparison to cyanide.

Dutrizac and Jambor (2000) stated that high temperatures (> 400°C) are not necessarily needed for jarosite decomposition, with natural breakdown occurring at 325°C over several days. With the addition of 0.3 M $H_2SO_4$ the temperature can be lowered to 180-190°C and further to 100°C with 0.5 M $H_2SO_4$.

Further research showed that a strong alternative to acid is an alkaline dissolution. Unlike acidic solutions, alkaline ones allow for the simultaneous breakdown of crystal structure while precipitating iron as goethite (FeO(OH)) leaving a solution of recoverable valuable metal-sulfates. It was shown that jarosite can be broken down in 1 hour at pH 11-12 (60°C), producing a solution of highly recoverable silver (Dutrizac & Jambor, 2000).

In a process patented by Sherrit, called the "Lime Boil", silver jarosite is broken down into a cyanide soluble silver precipitate by treating the material in a lime slurry at 80-95°C for up to 4 hours, according to the reaction (Gunaratnam et al., 2018):

$$AgFe_3(SO_4)_2(OH)_6 + 2CaO + 4H_2O \rightarrow AgOH + 3Fe(OH)_3 + 2CaSO_4.2H_2O \qquad (2.2)$$

Ju et al (2011) were able to develop a complex process demonstrating the use of alkaline leaching. The jarosite residue is initially broken down by sintering at 650°C for 1 hour before being leached in 6.0 M ammonium chloride ($NH_4Cl$) at 105°C. The process achieved Ag recoveries on the order of 70% and nearly complete recoveries (97-98%) of lead and zinc. The exposed valuable minerals are precipitated out using a cementation process. The residue of the

leach is subjected to a treatment process which produces a clean, arsenic- and silica-free iron concentrate.

Gonzalez-Ibarra et al (2016) also investigated the use of an alkaline media (NaOH, $Ca(OH)_2$) for the decomposition of silver-bearing jarosite, followed by recovery via cyanidation. Temperatures varied from 30-70°C and pH 8-11. Recovery of silver via cyanidation from the decomposed residues was 74.8%, compared to 18.2% if the breakdown stage was omitted. The decomposition of jarosite during this process proceeds according to the reaction (Gonzalez-Ibarra et al, 2016):

$$AgFe_3(SO_4)_2(OH)_{6(s)} + 4OH^-_{(aq)} \rightarrow Ag(OH)_{(s)} + 3Fe(OH)_{3(s)} + 2SO_4^{2-}{}_{(aq)} \quad (2.3)$$

## 2.6 Jarosite Solubility and Dissolution Rates

In highly acidic conditions (pH < ~3.8), jarosite minerals react with hydrogen ions ($H^+$) according to the following dissolution reaction (Baron & Palmer, 1996; Zahrai et al, 2013), where M is a cation listed in Table 2-2:

$$MFe_3(SO_4)_2(OH)_6 + 6H^+ \rightarrow xM^+ + yFe^{3+} + zSO_4^{2-} + 6H_2O \quad (2.4)$$

When pH > ~3.8, jarosite minerals tend to react with hydroxyl ions ($OH^-$), which forms a secondary iron oxide-hydroxide, goethite (FeO(OH)), on the surface of jarosite according to the following reaction (Smith et al, 2006):

$$MFe_3(SO_4)_2(OH)_6 + 3H_2O \rightarrow xM^+ + yFeO(OH) + zSO_4^{2-} + 3H^+ \quad (2.5)$$

Smith et al (2006) state that goethite, with small particle size and poor crystallinity, is the iron oxide/hydroxide phase that is present during the dissolution of potassium jarosite at pH 8, and forms on the surface of jarosite grains. The dissolution of potassium jarosite at both pH 2 and 8 was found to be incongruent, with selective dissolution of $K^+$ and $SO_4^{2-}$ occurring over Fe due to the high stability of the iron octahedra (Smith et al, 2006; Gasharova et al, 2005). This uneven dissolution is why equations 2.4 and 2.5 contain the factors x, y, z. In an ideal system

with congruent dissolution, the values of these coefficients would be: x = 1, y = 3, z = 2 (Baron & Palmer, 1996; Smith et al, 2006). Hydronium jarosite ($H_3OFe_3(SO_4)_2(OH)_6$) dissolution results in a release of hydronium ions ($H_3O^+$), which acidifies a solution (Basciano 2008; Grey et al. 2013). In alkaline solutions, silver ions react with hydroxide to form silver hydroxide [Ag(OH)], which rapidly passes to silver oxide ($Ag_2O$) according to the following reaction (Ganguly, 2012):

$$\begin{aligned} Ag^+ + OH^- &\rightarrow Ag(OH) \\ 2Ag(OH) &\rightarrow Ag_2O + H_2O \end{aligned} \tag{2.6}$$

Jarosite minerals will raise the pH of highly acidic solutions (pH < ~3.8) and lower the pH of slightly acidic/neutral/alkaline solutions (pH > ~3.8) until an equilibrium state between dissolution reactions (2.4 and 2.5) and an equilibrium pH value of 3.8 is reached (Zahrai et al, 2013).

An induction time, during which no dissolution occurs, was reported in acidic, neutral, and alkaline conditions for potassium and sodium jarosite (Reyes et al, 2016; Reyes et al, 2017) as well as in alkaline media for silver jarosite (Roca et al, 1993; Cruells, 2000; Patino et al, 2010). The induction period of silver jarosite varied between 10 and 60 minutes at pH values of 10.6-11.9 (30$^o$C). The time was shortened to 2.0-9.0 minutes when temperature was increased to 60$^o$C (Patino et al, 2010). Reyes et al (2016) determined induction times on the order of 20 hours at pH 10.8, around 4 hours at pH 11.7, and only 9 or so minutes at pH 12.5 (29.9$^o$C) for potassium jarosite samples containing ~38% of $CrO_4$ substitution for $SO_4$, demonstrating that increases in alkalinity result in shorter induction times. Induction times of 15 hours at pH 1.4 (29.9$^o$C) and 1.2 hours at pH 0.4 (29.9$^o$C) for potassium jarosite samples containing arsenic (Reyes et al, 2017) demonstrate that increasing acidity also leads to shorter induction times. Reyes et al (2017) deduced the pH of instantaneous dissolution to be 0.005 at 30$^o$C for potassium jarosite samples containing arsenic. No literature exists on the pH of instantaneous dissolution for pure jarosite minerals. However, based on similarities existing between jarosite minerals, it is likely to be very low. Results from Reyes et al (2016; 2017) demonstrate increased induction times for jarosite minerals containing contaminants or variations in the crystal structure (As, $CrO_4$). This is reinforced by Welch et al (2008) study which shows that

jarosite collected from acid sulfate soils (containing many contaminants), have dissolution rates 1-3 orders of magnitude lower than those reported for synthesized jarosite. Roca et al (1993) state that the end of the induction period for silver jarosite was marked by a colour change, moving from the original yellowish-orange to red.

Potassium jarosite dissolution mechanisms were closely investigated by Gasharova et al (2005) demonstrating that it is via localized dissolution leading to formation of etch pits as opposed to uniform dissolution over the entire particle surface. The data obtained for potassium-silver jarosite by Cruells et al (2000) show dissolution fitting to the shrinking core model. The reported dissolution rates in Table 2-4 are highly comparable between K/Na/Ag/$H_3O^+$ jarosites. Jarosite dissolution rates appear to follow a V-shaped curve as a function of pH, reaching minimum values around an equilibrium pH of 3.8 confirming that the dissolution kinetics are driven by a departure from the equilibrium conditions. Dissolution rates from Patino et al (2008; 2010) were reported in $min^{-1}$. These values were converted to $mol/m^2s$ using an average of the two high silver jarosite samples surface areas (Table 4-5) obtained from testing completed for the purposes of this thesis along with the molar mass of silver jarosite (569.57 g/mol).

Table 2-4: Previously Recorded Jarosite Dissolution Rates.

| Jarosite Mineral | pH | Dissolution Rate ($mol/m^2s$) | Source |
|---|---|---|---|
| Na | 2.0 | $1.3\times10^{-7}$ to $7.9\times10^{-8}$ (at 22°C) | Zahrai et al. (2013) |
| | 3.8 | $1.3\times10^{-9}$ to $1.6\times10^{-9}$ (at 22°C) | Zahrai et al. (2013) |
| | 4.0 | $5.2\times10^{-10}$ (at 23°C) | Elwood Madden et al. (2012) |
| | 8.0 | $4.5\times10^{-8}$ to $8.9\times10^{-8}$ (at 22°C) | Zahrai et al. (2013) |
| | 10.0 | $1.1\times10^{-7}$ to $2.6\times10^{-7}$ (at 22°C) | Zahrai et al. (2013) |
| K | 3.8 | $6.3\times10^{-12}$ (at 23°C) | Welch et al. (2008) |

| Jarosite Mineral | pH | Dissolution Rate ($mol/m^2s$) | Source |
|---|---|---|---|
| K | 5.5 | $1.5\times10^{-7}$ (at room temp.) | Gasharova et al. (2005) |
| Ag | 10.62 | $2.8\times10^{-7}$ (at 30°C) | Patino et al. (2010) |
| | 10.3 | $1.1\times10^{-7}$ (at 50°C) | Patino et al. (2010) |
| | 10.7 | $1.6\times10^{-7}$ (at 50°C) | Patino et al. (2010) |
| | 11.6 | $1.7\times10^{-7}$ (at 35°C) | Patino et al. (1998) |
| $H_3O^+$ | 5.5 | $4.4\times10^{-7}$ (at room temp.) | Gasharova et al. (2005) |

Temperature, followed by pH, was found to have the most significant effect on jarosite dissolution rates (Reyes et al, 2016; Reyes et al, 2017). Zahrai et al (2013) demonstrated that an increase in temperature results in higher dissolution rates of sodium jarosite, for all pH values from 2-10. Very similar data on the role of temperature were presented for potassium jarosite by Pritchett et al (2012). The dissolution of jarosite is strongly favoured at extreme pH values ($1 < pH > 12$) and temperatures above 50°C (Reyes et al, 2017). At pH 10.8 and at a temperature of 30°C, a steady-state dissolution of potassium jarosite was reached after ~1.5 days, compared to only 2 minutes at pH 12.3 at 60°C. At pH 1.69 (30°C) the steady-state dissolution of potassium jarosite was reached after ~10 days, compared to 8 minutes at pH 0.21 but at 80°C (Reyes et al, 2016). The effects of particle size on dissolution rates were also investigated, with smaller particles experiencing slightly higher dissolution rates, but these effects are small when compared to temperature and pH, and have no effect on the induction time (Reyes et al, 2017).

The selective incongruent dissolution of $K^+$ and $SO_4^{2-}$ leads to complications in determining the solubility product constant, $K_{sp}$, for jarosites (Desborough, 2010). The $K_{sp}$ of synthesized potassium jarosite at 25°C was experimentally determined to be $10^{-11}$ by Baron and Palmer (1996) and $10^{-11.3}$ by Smith et al (2006) and $10^{-11.34}$ (Smith, 2004). These $K_{sp}$ values were

obtained by using the ion activities to calculate the log{ion activity product (IAP)} (Equation 2.8) (Baron & Palmer, 1996; Smith et al, 2006). The ion activity is the effective ion concentration and often differs from the measured ion concentration (Table 2-5) due to ion interactions with each other as well as with water. The IAP was stated by Baron and Palmer (1996) to represent the $K_{sp}$ at dissolution equilibrium. The formula for log(IAP) (Equation 2.8) is the solubility product formula (Equation 2.7) rearranged and with [ion concentration] replaced with the {ion activity}. Baron and Palmer (1996) noted that on average the log[ion concentration] was 0.5 units less negative, or larger, than the log{ion activity}.

$$K_{SP} = \frac{[K^+] \times [Fe^{3+}]^3 \times [SO_4^{2-}]^2}{[H^+]^6} \tag{2.7}$$

$$\log(\text{IAP}) = \log\{K^+\} + 3\log\{Fe^{3+}\} + 2\log\{SO_4^{2-}\} + 6\,pH \tag{2.8}$$

Equilibrium ion concentrations from various studies on potassium jarosite dissolution are shown in Table 2-5.

Table 2-5: Jarosite Dissolution Equilbirium Ion Concentrations.

| pH | Concentrations (mol/L) | | | Dissolution Time (months) | Source |
|---|---|---|---|---|---|
| | $[K^+]$ | $[Fe^{3+}]$ | $[SO_4^{2-}]$ | | |
| 2 | $4.7\times10^{-4}$ | $1.6\times10^{-4}$ | $6.3\times10^{-4}$ | 4.7 | Smith (2004) |
| 2 | $2.0\text{-}2.1\times10^{-4}$ | $3.9\times10^{-4}$ | $3.3\times10^{-4}$ | 4 | Smith et al. (2006) |
| 2 | $2.1\times10^{-4}$ | $4.9\times10^{-4}$ | $3.4\times10^{-4}$ | 3-4 | Baron and Palmer (1996) |
| 8 | $2.0\text{-}2.1\times10^{-4}$ | $2.3\times10^{-6}$ | $3.3\text{-}3.4\times10^{-4}$ | 5.5 | Smith et al (2006) |

The results from Baron and Palmer (1996) and Smith et al (2004) are displayed as an average of 3 dissolution tests conducted at pH 2. The lowered concentration of iron ions at pH 8 shows that iron is precipitating out as goethite. This is confirmed by the high iron content that was displayed in the residual solids. All studies assigned sulfate ions a coefficient of 2 for calculations of the molecular formula, a convention which is frequently used for jarosite dissolution.

Using the equilibrium concentration and molar ratio of sulfate ions, along with the molar mass of potassium jarosite (500.81 g/mol), it is possible to estimate jarosite solubility (g/L) based on sulfate dissolution at both pH 2 and 8 (Equation 2.9). The same can be done with the equilibrium concentration and molar ratio of potassium ions. The estimations of solubility are shown in Table 2-6.

$$\text{Solubility}\left(\frac{g}{L}\right)=\frac{\left[\frac{K^+}{SO_4^{2-}}\right]\left(\frac{mol}{L}\right)}{\text{Molar Ratio }(K^+/SO_4^{2-})}\times\text{Potassium Jarosite Molar Mass}\left(\frac{g}{mol}\right) \qquad (2.9)$$

Table 2-6: Estimated Jarosite Solubility from Steady-state Dissolution.

| Source | Ion Used in Calculation | Solubility of Jarosite at pH 2 (g/L) | Solubility of Jarosite at pH 8 (g/L) |
|---|---|---|---|
| Smith et al. (2006) | $SO_4^{2-}$ | 0.083 | 0.082-0.085 |
| | $K^+$ | 0.082-0.084 | 0.082-0.085 |
| Baron and Palmer (1996) | $SO_4^{2-}$ | 0.085 | - |
| | $K^+$ | 0.104 | - |
| Smith (2004) | $SO_4^{2-}$ | 0.117 | - |
| | $K^+$ | 0.079 | - |

Goethite precipitation at pH 8 is dependent on jarosite dissolution (Equation 2.5). It is possible to estimate the amount of goethite (g/L) that has precipitated at steady-state conditions by using an average of the estimated solubility at pH 8 (Equation 2.10).

$$\text{Goethite Precipitation}\left(\frac{g}{L}\right)=\frac{\text{Jarosite Solubility}\left(\frac{g}{L}\right)}{\text{Potassium Jarosite Molar Mass}\left(\frac{g}{mol}\right)}\times \frac{\text{Goethite Molar Ratio}}{\text{Goethite Molar Mass}\left(\frac{g}{mol}\right)} \quad (2.10)$$

This calculation results in an estimated goethite precipitation of 0.0346 g/L at steady-state dissolution of potassium jarosite. Additional analysis of these results, in relation to the data from this thesis, will be presented in the discussion section.

## 2.7 Surface Charges on Minerals

All solids acquire an electrical surface charge when placed in a polar solvent (Delgado, 2002). These surface charges are very difficult to experimentally measure (Cosgrove, 2010). The development of a surface charge on a particle can be due to multiple, complex phenomena (Delgado, 2002). These mechanisms responsible can be classified into four main groups: ion adsorption, dissolution of ionic solids, ionisation of surface groups, and isomorphous ion substitution (Delgado, 2002; Cosgrove, 2005; Cosgrove 2010). Charging through ion adsorption takes place when a certain ionic species adsorbs onto the surface of a mineral, imparting an electrical charge. This is typically the case when a strong ionic surfactant, with a high affinity to the mineral surface, is added (eg. adsorption of dodecyl sulfate on goethite (FeO(OH)) above goethite's isoelectric point). The isoelectric point is a pH value at which the zeta potential of a mineral particle is zero, implying that the particle surface is net-zero charged. Polyvalent cations and anions are also capable of imparting surface charges to mineral surfaces. Surface charging due to dissolution of ionic solids occurs when a solution contains an ion also present in the crystal lattice. This causes a preferential release of ions into solution by the mineral in order to satisfy the solubility product (eg. silver iodide in a solution of silver ions will preferentially release iodine, imparting a positive charge on the particle). Several mineral types, for example all oxide/hydroxide minerals (including goethite) react with water to form surface functional groups. In the case of oxide minerals, their surfaces in aqueous solutions show the presence of hydroxyl groups (-OH) that can then react with acids or bases depending on the pH to give positive or negative surface charges. For example, aluminum oxide below the isoelectric point

will be positively charged due to surface hydroxyl groups (Al-OH) accepting a hydrogen cation to form positively charged Al-$OH_2^+$ sites on the oxide surface. As the pH moves above the isoelectric point, the surface hydroxyl groups will dissociate to generate negatively charged Al-$O^-$ sites. Isomorphous substitution is when one atom in the crystal lattice is substituted for another of similar size but of different valency. This mechanism is most commonly found in aluminosilicate (clay) minerals, where $Si^{4+}$ is readily substituted for $Al^{3+}$, $Al^{3+}$ by $Mg^{2+}$, $Zn^{2+}$, or $Fe^{2+}$. This results in a permanent net negative charge (pH-independent) on the basal plane of a clay mineral (Cosgrove, 2005).

Ions that adsorb on mineral surfaces and determine the difference in potential between the solid and liquid phase are known as potential determining ions (pdi). Inert ions are those which do not alter the surface charge density or interfere with the adsorption of potential determining ions (Cosgrove, 2010).

Whichever mechanism(s) are responsible for the origin of a surface charge on a particle, when placed in an electrolytic solution, the charges on the particle surfaces will be balanced by surrounding ions adsorbing from solution. This surrounding region is known as the electric double layer (EDL). The thickness of the EDL is defined as the Debye length ($\kappa^{-1}$) and can be calculated for cases in water at room temperature with the following equation, where I is the ionic strength of the solution in mol/L (Israelachvili, 1985):

$$\kappa^{-1}(nm) = \frac{0.304}{\sqrt{I\left(\frac{mol}{L}\right)}} \tag{2.11}$$

Electro-neutrality is achieved when the layer near the solid/liquid interface contains a net charge equal and opposite to that of the solid (Cosgrove, 2010). The EDL is made up of a dense inner region called the Stern Layer and an outer more diffuse layer (Delgado, 2002). The Stern Layer is made up of the Inner and Outer Helmholtz planes (IHP and OHP). The formation of the EDL helps to stabilize colloidal suspensions by creating repulsive electrostatic forces between particles that overcome the attractive van der Waals forces under certain conditions (pH, T, or ion concentration). The distribution of ions in the diffuse layer is reliant upon the electrolyte concentration, the charge of the ions, the solvent type, and the potential at the

boundary between the Stern Layer and the diffuse layer of the EDL (Cosgrove, 2010). The potential at this boundary is often equated to the zeta potential, which can readily be determined experimentally. The zeta potential, denoted by the Greek symbol ζ, is a term used to describe the electric potential at the "slipping plane" or "shear layer" (Drzymala, 2007), which is located in the diffuse layer, at a distance equal to the thickness of the Stern Layer plus the radius of the particle (Cosgrove, 2010).

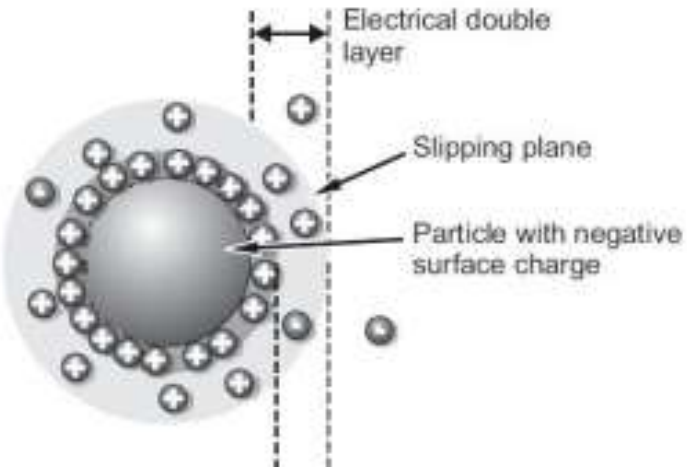


Figure 2-4: Potential of a suspended particle (NanoComposix, 2012).

Due to the charge gathered around a particle, the particle will be set into motion when exposed to an electric field. This phenomenon is known as electrophoresis and is the basis for the measurement of the zeta potential (Ohshima, 2002). The zeta potential is determined by examining the relationship between the applied current/voltage and the relative flow of ionic solution with respect to the charged particle (Cosgrove, 2005). The velocity of a moving particle is directly measured, and the electrophoretic mobility ($\mu_e$ [$m^2$/Vs]) is calculated with Equation 2.12, where $V_e$ is equal to the particle velocity [μm/s] and $\underset{\infty}{E}$ is the applied electric field [V/cm] (Delgado, 2002).

$$\mu_e = \frac{V_e}{\underset{\infty}{E}} \tag{2.12}$$

Assuming particles of spherical shape, the zeta potential can be calculated from the electrophoretic mobility using Equation 2.13, where $F(\kappa a)$ is Henry's function, $\varepsilon_{(rs)}$ is the

relative permittivity of the solution [$A^2s^4/kgm^3$], $\varepsilon_{(0)}$ is the permittivity of a vacuum [$A^2s^4/kgm^3$], and $\eta$ is the liquid viscosity [Pa s] (Swan & Furst, 2012).

$$\mu_e = F(\kappa a)\frac{\varepsilon(rs)\varepsilon(0)}{\eta}\zeta \tag{2.13}$$

Henry's function is dependent on the relationship between particles radius ($a$) and the thickness of the EDL, also known as the Debye length ($\kappa^{-1}$). A simplified version of Henry's function is shown in Equation 2.14. This version was found to mathematically deviate from the original by less than 0.1% (Swan & Furst, 2012):

$$F(\kappa a) = \frac{16 + 18\kappa a + 3(\kappa a)^2}{16 + 18\kappa a + 2(\kappa a)^2} \tag{2.14}$$

If $a << \kappa^{-1}$ then Henry's function approaches 1 and Equation 2.13 becomes the Huckel formula (Equation 2.15) (Swan & Furst, 2012). This limit applies to suspensions of small particles or those with low electrolyte concentrations that have a large Debye length (Delgado, 2002). If $a >> \kappa^{-1}$ then Henry's function approaches 1.5 and Equation 2.13 becomes the Smoluchowski's formula (Equation 2.16) for calculating the zeta potential (Swan & Furst, 2012). The Smoluchowski equation is used for thin EDLs with respect to particle size, and is typically valid when $\kappa a$ is greater than approximately 200-300 (Hunter, 1981). This situation applies to suspensions with relatively large particles or those with a high electrolyte concentration, and a smaller Debye length (Delgado, 2002).

$$\mu_e = \frac{\varepsilon(rs)\varepsilon(0)}{\eta}\zeta \tag{2.15}$$

$$\mu_e = \frac{3}{2}\frac{\varepsilon(rs)\varepsilon(0)}{\eta}\zeta \tag{2.16}$$

These calculations are based upon the assumption that liquid viscosity jumps from an infinite value in Stern's layer to a finite value in the diffuse layer. This model, while not

accurate, works reasonably well for the calculation of the zeta potential (Delgado, 2002). These calculations are also conducted under the assumption of a static electric field (Ohshima, 2002).

A set of conditions (e.g., a pH value, or ion concentration) at which the electrical surface charge equals zero is known as the point of zero charge (pzc). In the absence of specifically adsorbing ions the pzc is identical to the isoelectric point or iep (Drzymala, 2007). Particles with a zeta potential between -10 and +10 mV are approximately neutral, while those greater than +/-30 mV are strongly charged (Clogston & Patri, 2010).

Xu et al. (2013) state that the surface charge of jarosite is amphoteric with synthesized samples having one pzc at pH 5.6 with a positive surface charge <5.6 and a negative surface charge >5.6.

Experiments conducted by Sadowski et al. (2001) on a sample of potassium jarosite resulted in 2 isoelectric points, similar to those obtained by Smeaton (2012), of pH ~3.9 and 5.7, being negatively charged between these two values, and positive otherwise. However, when a dispersant was used to prevent particle coagulation, the zeta potential results gave only one pzc, continuing to decrease towards more negative values as pH was increased.

## 2.8 Contact Angle and Wetting Properties

When a small liquid drop is placed on a solid surface it will either spread and completely wet the surface or form a droplet. The contact angle ($\theta$) is the angle that the droplet forms at the interface of the solid/liquid/gas phases, and is measured from the inside of the droplet (Figure 2-5) (Cosgrove, 2010). Wetting of particles plays an important role in mineral flotation, oil recovery, lubrication, liquid coating, printing, and spray quenching. Wettability tests measure the contact angle between a solid and liquid. In the case of water, the higher the contact angle of water the more hydrophobic the solid (Yuan & Lee, 2013). A perfectly hydrophilic solid is described as being completely wetted by water, not attaching to air bubbles when submerged in water. A perfectly hydrophobic solid is the opposite, repelling water. Perfect wetting results in a contact angle of $0^o$ while perfect de-wetting (total hydrophobicity) gives a contact angle of $180^o$ (Leja, 1982; Cosgrove, 2010).

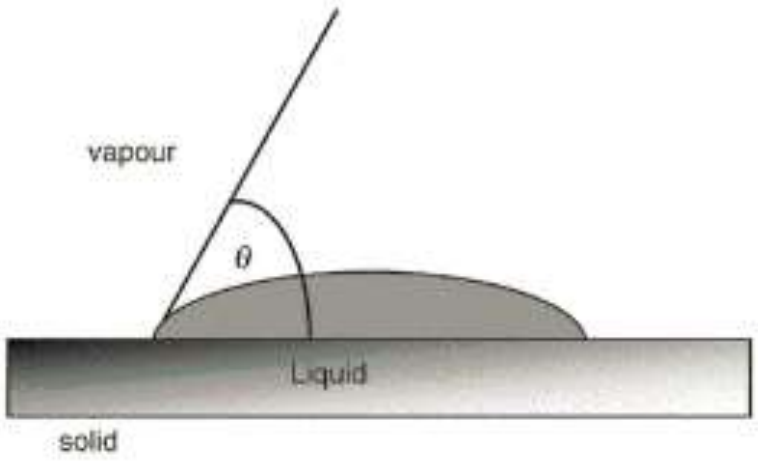


Figure 2-5: Contact Angle (© Reynolds, 2010, by permission).

Adhesion between a solid and liquid can be quantified in terms of the work required [W(a)] to separate a specific area of the solid from the liquid (Reynolds, 2010). It is defined by the following equation (Leja, 1982; Fuerstenau & Raghavan, 2007; Reynolds, 2010):

$$W(a) = \gamma(s.v) + \gamma(l.v) - \gamma(s.l) \tag{2.17}$$

Where $\gamma(s.v)$ is the surface energy between solid and vapour phases, $\gamma(l.v)$ is the surface tension between liquid and vapour phases, and $\gamma(s.l)$ is the surface energy between solid and liquid phases (Leja, 1982; Reynolds, 2010). Reynolds et al (2010) state, "even though surface energy and surface tension are dimensionally the same, they are defined and measured differently." Surface energy ($J/m^2$) is the minimum work required per unit area to increase or create a new solid/liquid or solid/vapour interface. Surface tension (N/m) is measured as the force applied per unit length in parallel with a liquid surface and can be interpreted as the minimum work per unit area ($J/m^2$) required to increase the liquid/vapour interface. Surface tension originates from the missing intermolecular forces imposed on liquid molecules at the interface in the direction of the vapour. This imbalance results in liquid molecules packing closely together at the interface and pulling inwards, giving them an increased cohesiveness at the surface. Cohesion within a liquid can be expressed as the work of cohesion, or the work required [W(c)] to separate a specific cross-sectional area of the liquid from itself, or in other words, the creation of two new liquid/vapour interfaces (Fuerstenau & Raghavan, 2007; Reynolds, 2010; Leja, 1982):

$$W(c) = 2\gamma(l.v) \tag{2.18}$$

Surface energy values can be related to each other through Young's Equation (Leja, 1982):

$$\gamma(s.v) = \gamma(s.l) + \gamma(l.v)\cos(\theta) \tag{2.19}$$

Substituting Young's Equation (2.19) into Equation 2.17 and then dividing by the work of cohesion (2.18) results in the following equation relating the work of adhesion and cohesion to the contact angle between the solid and the liquid (Leja, 1982; Reynolds, 2010):

$$\cos(\theta) = 2\frac{W(a)}{W(c)} - 1 \tag{2.20}$$

Equation 2.20 shows that when W(a) = W(c) the contact angle is $0^o$ and perfect wetting occurs. If W(a) << W(c) (or when Wa/Wc ≈ 0) the contact angle will approach $180^o$ and perfect non-wetting will occur (Leja, 1982). In other words, water strongly adheres to hydrophilic solids (the work of adhesion is high), and weakly, if at all, adheres to hydrophobic solids so the work of adhesion in this case is very low.

The spreading coefficient (S) is defined as (Leja, 1982):

$$S = W(a) - W(c) \tag{2.21}$$

When S is positive, a liquid will tend to completely spread on the solid surface into a thin film. When S is negative spreading is non-existent, and a droplet will form on the solid surface indicating a level of hydrophobicity (Leja, 1982). By substituting the work of adhesion (Equation 2.17) and the work of cohesion (Equation 2.18) into Equation 2.21, results in S also to be defined as:

$$S = \gamma(s.v) - \gamma(l.v) - \gamma(s.l) \tag{2.22}$$

Substituting Young's Equation (2.19) into Equation 2.22 for S, the following relationship between S and the contact angle (θ) can be developed:

$$S = \gamma(l.v)\left[\cos(\theta) - 1\right] \tag{2.23}$$

This equation demonstrates that for the spreading coefficient to be negative, the cos(Θ) must be less than 1, and the contact angle must be larger than zero. Thought about in terms of flotation, S < 0 is required to induce mineral hydrophobicity, and therefore the minimum conditions to achieve particle/bubble attachment are (Fuerstenau and Raghavan, 2007):

$$\gamma(s.v) - \gamma(s.l) < \gamma(l.v) \tag{2.24}$$

In reality, a minimum contact angle exists to induce flotation of various minerals. Therefore, a more negative S value is required in reality (Fuerstenau and Raghavan, 2007). The contact angle is dictated by the cohesion of the liquid within itself and the adhesion of the liquid to the solid. In most cases, to utilize froth flotation for mineral separation, the surface characteristics of particles must be altered to render them hydrophobic. This modification can occur through a rearrangement of surface atoms or by surfactant adsorption. These interfacial phenomena lead to a decrease in the work of adhesion and induce hydrophobicity.

In the absence of surfactants, maximum hydrophobicity of a solid occurs at the pzc. However, the contact angle at the pzc may still be too low to provide sufficient conditions for flotation. Once a surfactant is introduced and renders a minerals surface hydrophobic, flotation will proceed even when the surface is highly charged.

## 2.9 Flotation Reagents

Surface active agents or more commonly, surfactants, are organic molecules that have the ability to adsorb at an interface, therefore modifying the physical properties of the surface (Eastoe, 2010). Flotation surfactants are usually composed of a non-polar, hydrophobic,

hydrocarbon radical [R], and a polar, hydrophilic head group (Casandra et al, 2017). The head group can be charged or neutral, small (eg. Sulfate R-$OSO_3$) or a polymeric chain (eg. polypeptide R-NH-CHR-CO-NH-$CHR^I$-CO-…-$CO_2H$). The hydrocarbon radicals are grouped into three main classes (Leja, 1982):

1) Alkanes: all carbon atoms are joined by single bonds.
2) Alkenes: at least two carbon atoms are joined by a double bond.
3) Alkynes: at least two carbon atoms are joined by a triple bond.

Based on the type of the hydrophilic functional group, flotation surfactants can further be divided into (Leja, 1982):

1) Thio compounds: Polar groups contain at least one sulfur atom not bonded to oxygen. Usually used as collectors for metallic sulfides.
2) Non-thio, ionizable compounds: Represented by alkyl carboxylates, such as fatty acids, alkyl sulfates/sulfonates, alkyl phosphates, alkyl hydroxamates, and amines.
3) Non-ionic compounds: Alcohols, aldehydes, amides, esters, and water-insoluble oils.

Surfactants capable of converting a minerals surface from hydrophilic to hydrophobic are referred to as collectors. Collectors must be adsorbed on the mineral surface in such a way that they can withstand movement of liquid along the shear plane, without experiencing displacement. There are three main mechanisms through which surfactants adsorb on mineral surfaces and act as a collector (Leja, 1982):

1. Chemisorption – chemical bond is formed between the surfactant and the mineral surface.
2. Physical Adsorption – when the interaction between the surfactant and the surface is due to weak forces, such as Van der Waals.
3. Electrostatic Adsorption – when the interaction between the surfactant and the collector occurs through coulombic attractive forces. This mechanism takes place when the surfactant and the mineral surface are oppositely charged. Since no chemical bond

forms between the surfactant and the surface, this types of adsorption is also viewed as physical adsorption.

All three reagents selected for this thesis are classified as non-thio, ionizable surfactants (Leja, 1982). Non-thiol collectors adsorb onto minerals through chemisorption, physical, and electrostatic adsorption (Bulatovic, 2007). The three reagents selected were: a sodium salt of lauric acid, sodium dodecyl sulfate, and octanohydroxamic acid. These reagents are discussed individually in the following sections.

### 2.9.1 Lauric Acid

Lauric acid ($C_{12}H_{24}O_2$), with the systematic name dodecanoic acid, is a fatty acid consisting of 12 carbon atoms in the hydrocarbon chain (Quast, 2015).

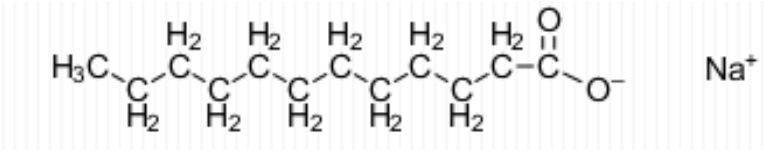

Figure 2-6: 2-D Structure of Sodium Laurate.

Fatty acids are primarily used for flotation of non-sulfide minerals, such as phosphates (apatite, $Ca_3(PO_4)_2$), carbonates (e.g., calcite, $CaCO_3$), or sulfates (e.g., barite ($BaSO_4$). Fatty acids are weak electrolyte collectors, and their behaviour is strongly dependant on pH, with colloidal precipitates of the poorly soluble acid form forming under acidic conditions. The pH of precipitation is dependent upon the total concentration of lauric acid added to solution. The reversible dissociation reaction of lauric acid is shown in Equation 2.25 and the formation of the precipitate is shown in Equation 2.26 (Vurdela & Laskowski, 1987; Laskowski, 1999).

$$RCOOH_{Aqueous} \leftrightarrow RCOO^{-} + H^{+} \tag{2.25}$$

$$RCOOH_{Solid} \leftrightarrow RCOOH_{Aqueous} \tag{2.26}$$

The pH of precipitation can be calculated as follows (Vurdela & Laskowski, 1987):

$$pH_{Precipitate} = pK_a - \log S + \log(C_T - K_{sp}) \tag{2.27}$$

Where $pK_a$ represents the negative base 10 logarithm of the acid dissociation constant, $K_a$, and S represents the solubility of the RCOOH molecule ($1.2\times10^{-5}$ M). The $pK_a$ is the pH at which concentrations of $RCOO^-$ and RCOOH species are equal. Lauric acid has a $pK_a$ of about 5. The acid dissociation constant is defined as (Vurdela & Laskowski, 1987; Laskowski, 1999):

$$K_a = \frac{[RCOO^-]\times[H^+]}{[RCOOH]_{Aqueous}} \tag{2.28}$$

As soon as the concentration of aqueous RCOOH increases above the solubility limit, any excess acid will form a colloidal precipitate according to reaction 2.26. Below the pH of precipitation, the concentration of the aqueous RCOOH species is equal to the solubility limit. For any total acid concentration, $C_T$, the concentration of each species in solution can be calculated (Equations 2.29, 2.30) (Vurdela & Laskowski, 1987):

Above $pH_{Precipitation}$

$$\begin{aligned} [RCOO^-] &= \frac{C_T \times K_a}{K_a + [H^+]} \\ [RCOOH]_{Aqueous} &= \frac{C_T \times [H^+]}{K_a + [H^+]} \\ [RCOOH]_{Solid} &= 0 \end{aligned} \tag{2.29}$$

Below $pH_{Precipitation}$

$$\begin{aligned} [RCOO^-] &= \frac{K_a \times S}{[H^+]} \\ [RCOOH]_{Aqueous} &= S \\ [RCOOH]_{solid} &= C_T - S - \frac{K_a \times S}{[H^+]} \end{aligned} \tag{2.30}$$

### 2.9.2 Sodium Dodecyl Sulfate

Sodium dodecyl sulfate ($C_{12}H_{25}SO_4Na$), which is also referred to by the common name sodium lauryl sulfate, is an alkyl sulfate (Leja, 1982). Alkyl sulfates are oxyhedral, non-thiol, anionic collectors. If the hydrocarbon group is connected to sulfur via an oxygen bridge, the compound is classified as a sulfate. If connected directly to the sulfur atom, it is a sulfonate (Bonda et al, 2015). Alkyl sulfates in general are considered to be strong electrolytes, i.e., they are fully dissociated above a pH value of 3 (Leja, 1982), and have much longer carbon chains (10-18) than thiol collectors (Bulatovic, 2007). They are primarily used for the flotation of oxide ores, carbonaceous material, and sulfur bearing minerals. The structure of sodium dodecyl sulfate can be seen in Figure 2-7.

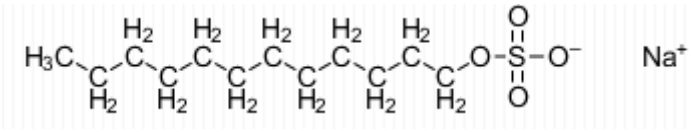

Figure 2-7: 2-D Structure of Sodium Dodecyl Sulfate.

Han et al (1973) showed physisorption of sodium dodecyl sulfate on the surface of hematite ($Fe_2O_3$) at pH values lower than the pzc. Adsorption was shown to be limited when pH was above the pzc, due to the surface becoming negatively charged and consequently repelling the sodium dodecyl sulfate ions. Quast (2000) also showed physical adsorption of dodecyl sulfate on the surface of hematite below the pzc. Iwasaki et al (1960) demonstrated flotation of goethite with dodecyl sulfate below the pzc (6.7), and no flotation above the pzc, even when conditioned with $10^{-3}$ M (222.3 mg/L) dodecyl sulfate. Concentrations as low as $10^{-6}$ M (0.22 mg/L) were able to successfully float goethite at pH 4, with higher concentrations being required as the pH became closer to the pzc.

### 2.9.3 Octanohydroxamic Acid

Octanohydroxamic acid ($C_8H_{17}NO_2$, or $C_7H_{15}$-CONH-OH ), which is also referred to by the common name caprylohydroxamic acid, is an anionic straight chain surfactant. All

hydroxamates are known to be chelating agents (Fuerstenau, 2007b). The structure of octanohydroxamic acid can be presented as in Figure 2-8.

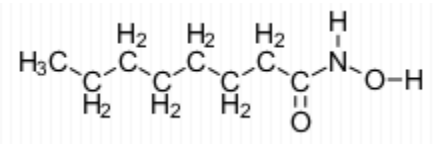

Figure 2-8: 2-D Structure of Octanohydroxamic Acid.

A chelating agent contains at least two electron donor atoms capable of bonding to a single metal ion. Five different classes of chelating agents containing two donor atoms can be distinguished. These are based on the elements available for bonding. The 5 classes are N-O, O-O, S-N, S-S, and N-N. Octanohydroxamic acid is classified as an O-O type chelating agent due to the carbonyl (=O) and ester (-O-) groups (Fuerstenau et al, 2000). Hydroxamates have a high affinity to form metal chelates with divalent, trivalent, and tetravalent transition metals, in particular iron (Beccia, 2014). The hydrophobic metal complexes formed by metal chelation are believed to be characterized by a ring structure (Figure 2-9) (Wasan et al, 1988).

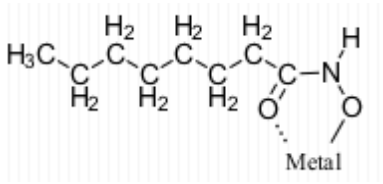


Figure 2-9: Chelation of Metal Cation Octanohydroxamic Acid.

The solubility of octanohydroxamic acid was reported to be 1.55 g/L ($9.73\times10^{-3}$ M). (Toxicology Risk Assessment Consulting, 2016). The reversible dissociation reaction of octanohydroxamic acid is shown in Equation 2.31. The solubility of the RCONHOH molecule is much larger ($9.75\times10^{-3}$ M) than that of the lauric acid RCOOH molecule ($1.2\times10^{-5}$ mol/L) and precipitates of hydroxamate are not expected to form at hydroxamate concentrations used for the purpose of this thesis.

$$RCONHOH \rightarrow RCONHO^{-} + H^{+} \tag{2.31}$$

The $pK_a$ of octanohydroxamic acid was experimentally determined to be around 8.6 to 9.4 (Kragen and Decnop-Weever, 1987). This pKa values indicates that hydroxamic acid, RCONHOH, is the dominant form in solution at pH values lower than 9. At pH values higher than 9, the hydroxamate anion, $RCONHO^-$, is the dominant species.

Hydroxamates were first introduced as flotation collectors in Germany in 1940 for oxide copper and iron ores but saw fairly limited use (Natarajan, 2013). Over the past few years hydroxamates have begun to garner higher interest due to an increasing amount of refractory, non-sulfide, oxide-type, and rare-earth type ores to be processed (Hope et al, 2010; Zhang et al., 2014) as well as cheaper methods developed for producing the reagent (Jordens et al, 2014). Hydroxamates are known to have a strong ability to selectively bond to minerals containing elements such as titanium, yttrium, lanthanum, cerium, iron, manganese, copper, and tin (Fuerstenau, 2007b). Hydroxamic acids have also successfully been used as a collector in flotation circuits containing clay, oxide copper, cassiterite ($SnO_2$) (Fuerstenau et al, 2000), wolframite ($(Fe, Mn)WO_4$), and pyrochlore ($(Ce, Ca)Nb_2O_6$-$(Ti, Th)O_3$) (Leja, 1982).

## 3.0 Experimental Procedure

### 3.1 Materials

#### 3.1.1 Equipment

A 600 mL stainless steel Parr 5100 autoclave (Figure 3-1) was used for jarosite synthesis with a single turbine type impellor located at the bottom of the reaction vessel. The vessel temperature and the rotational speed of the impellor were controlled by a Parr 4848 controller.

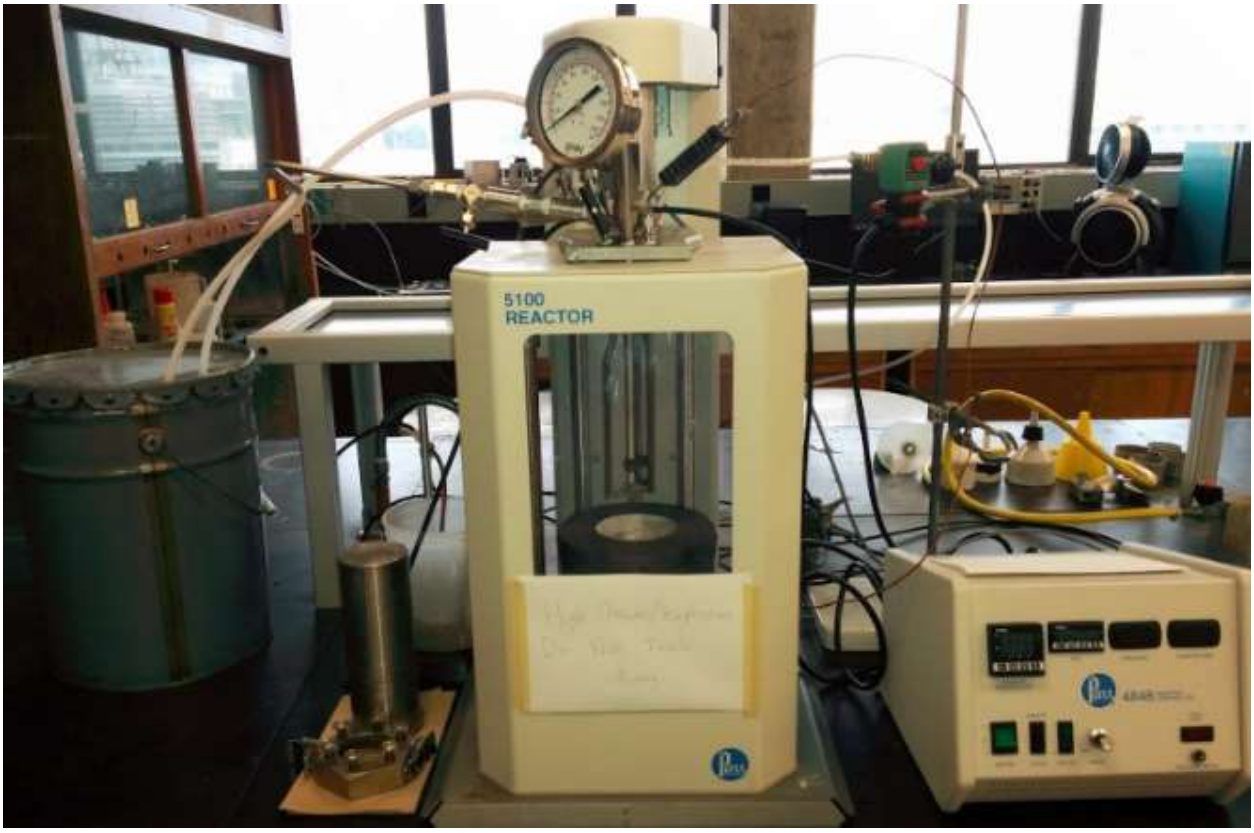


Figure 3-1: Parr 5100 Autoclave and Parr 4848 Controller.

A ParticleMetrix Zeta View PMX 100 (Figure 3-2) was used for zeta potential measurements of jarosite samples. A Shimadzu total organic carbon analyzer (TOC-V) with an ASI-V loading tray (Figure 3-3) was used for analysis of residual surfactant concentrations left in solution after adsorption on the jarosite samples. A Quantachrome Autosorb-1 (Figure 3-4) was used for surface area and porosity analysis, and the particle size distribution analysis of samples was carried out using the Malvern Mastersizer (Figure 3-6). A First Ten Angstroms

FTA 1000 drop shape instrument (Figure 3-5) was used for contact angle testing. An IKA KS 4000 ic control shaking table (Figure 3-5) was used for all sample preparation and conditioning.

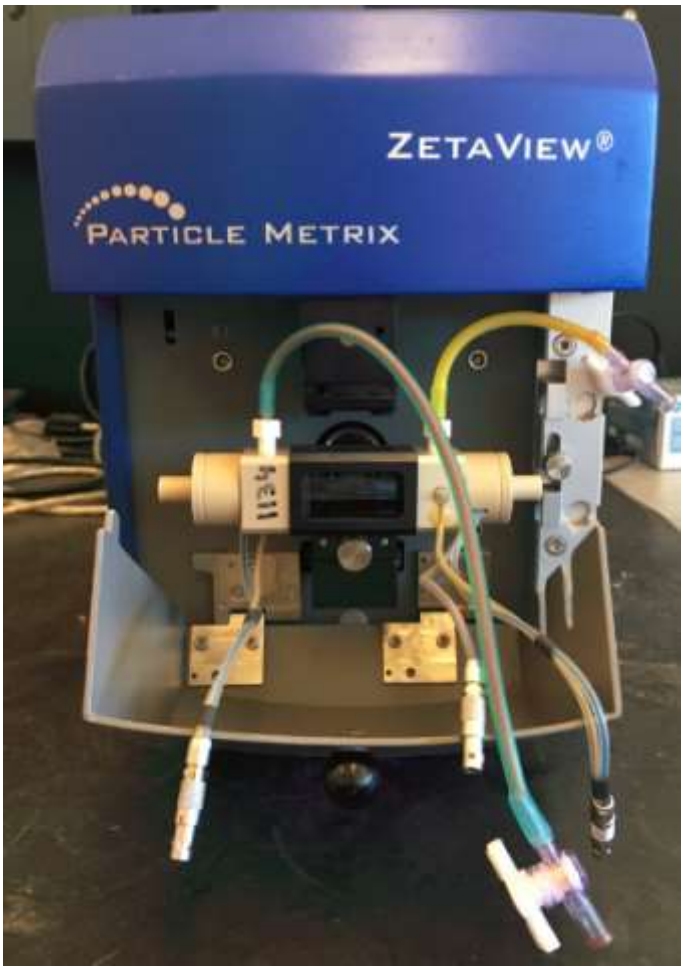


Figure 3-2: ParticleMetrix Zeta View PMX 100.

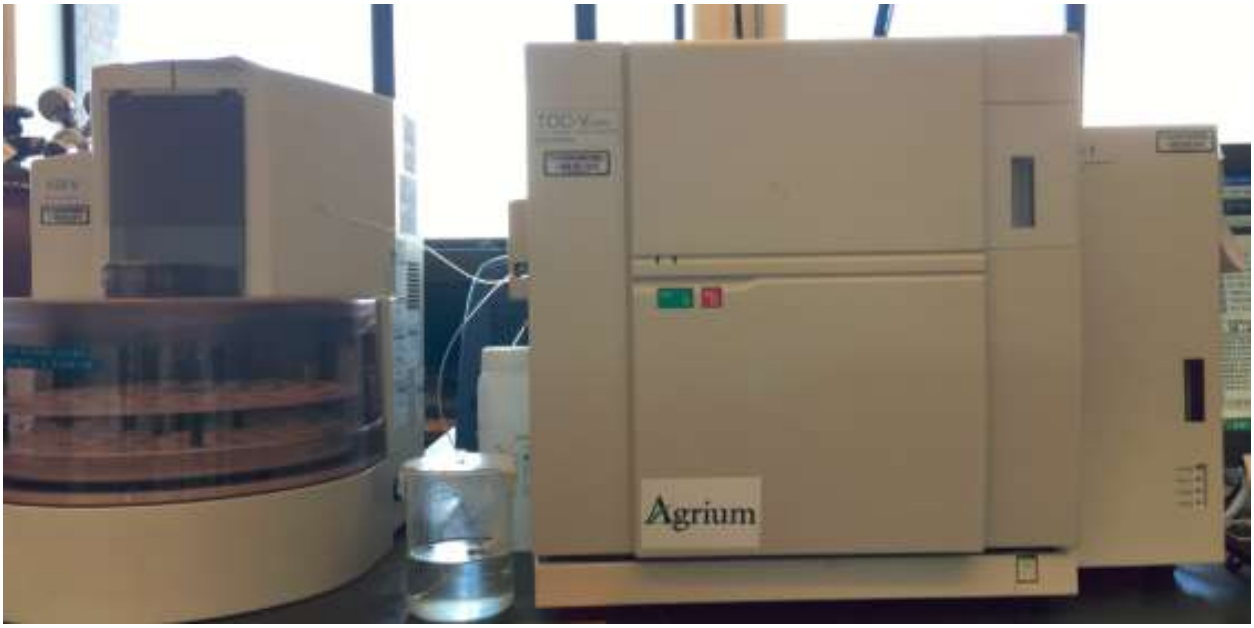


Figure 3-3: Shimadzu total organic carbon analyzer (TOC-V) with an ASI-V loading tray.


Figure 3-4: Quantachrome Autosorb-1.

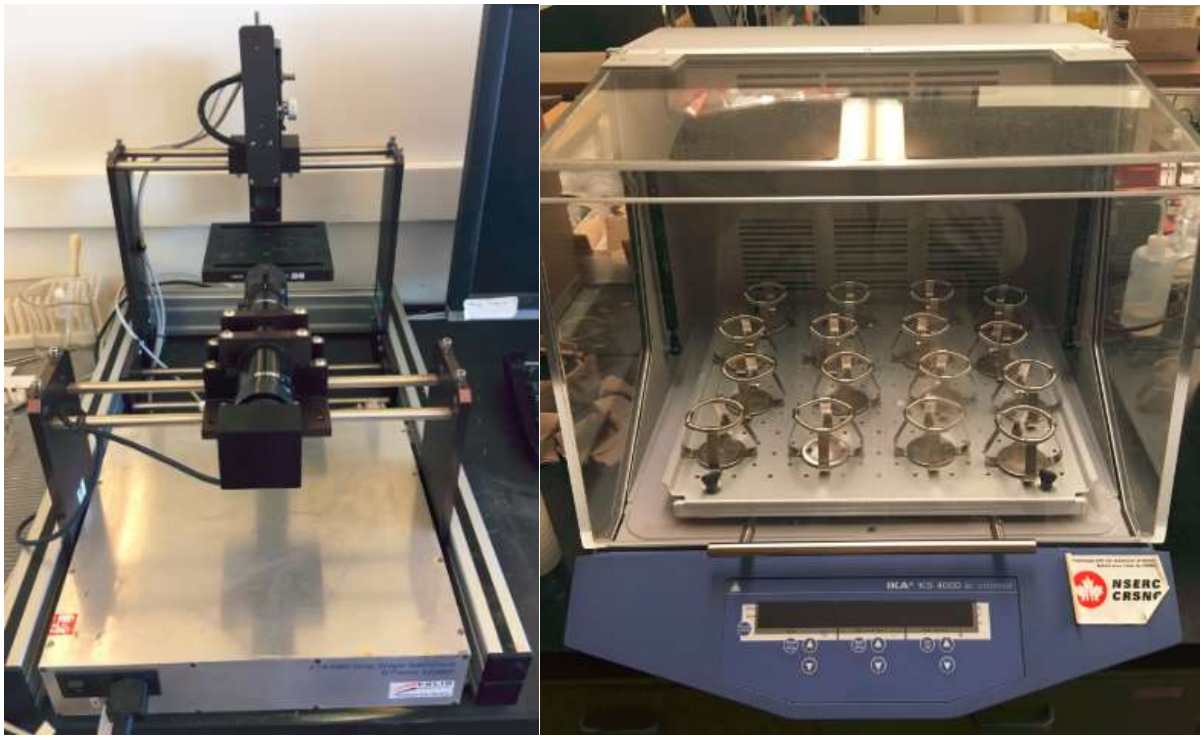

Figure 3-5: First Ten Angstroms FTA 1000 Drop Shape Instrument (left). IKA KS 4000 ic Control Shaking Table (right).

Figure 3-6: Malvern Mastersizer.

### 3.1.2 Reagents

Reagent grade powders of iron (III) sulfate ($Fe_2(SO_3)_4$), sodium sulfate ($Na_2SO_4$), and potassium sulfate ($K_2SO_4$) from Fisher Chemical, silver sulfate ($Ag_2SO_4$) from Alfa Aesar, and sulfuric acid ($H_2SO_4$) from Anachemia (95-98%) were used for jarosite synthesis.

Reagent grade powders of lauric acid ($C_{12}H_{24}O_2Na$) and dodecyl sulfate ($CH_3(CH_2)_{11}OSO_3Na$) sodium salts from ACROS Organics, and octanohydroxamic acid ($C_8H_{17}NO_2$) from Tokyo Chemical Industry were used for adsorption and flotation test-work. Pellets of sodium hydroxide (NaOH) from Fisher Chemical and Nitric Acid ($HNO_3$) from Anachemia were used for all pH adjustments. Sodium nitrate ($NaNO_3$) from Fisher Chemical was used as a background electrolyte (0.01 M) for all tests.

## 3.2 Methods

### 3.2.1 Jarosite Synthesis

Jarosite synthesis was performed using reagent grade chemicals following a modified version of procedures laid out in Dr. J.E. Dutrizac's literature (Dutrizac, 1983; Dutrizac, 1999; Dutrizac, 2004; Dutrizac & Chen, 2004; Dutrizac & Jambor, 2000; Dutrizac & Kaiman, 1976), details of which were given in Section 2.4. Five jarosite types were synthesized in a 600 mL autoclave reaction vessel at an initial acid concentration of 0.01 M $H_2SO_4$. The synthesis conditions were as follows:

Table 3-1: Jarosite Synthesis Conditions.

| Species | $Fe_2(SO_4)_3$ (M) | $Ag_2SO_4$ (M) | $Na_2SO_4$ (M) | $K_2SO_4$ (M) |
|---|---|---|---|---|
| Baseline Na-Jarosite | 0.3 | - | 0.2 | - |
| Low Silver Na-Jarosite | 0.3 | 0.01 | 0.09 | - |
| High Silver Na-Jarosite | 0.3 | 0.04 | 0.06 | - |
| Baseline K-Jarosite | 0.3 | - | - | 0.2 |
| High Silver K-Jarosite | 0.3 | 0.04 | - | 0.06 |

Dutrizac (1983) stated an optimal concentration of iron sulfate for jarosite precipitation is in the range 0.15-0.4 M. A concentration of 0.3 M iron sulfate was arbitrarily selected from this range and kept constant for all 5 synthesized samples. As also recommended by Dutrizac (1983), double the stoichiometric amount of sodium and potassium sulfate (0.2 M) was used for baseline (no silver) sample synthesis. Exact stoichiometric amounts (0.1 M), instead of double, of combined silver/sodium/potassium sulfate were selected for synthesis of samples containing silver in order to try and obtain better silver inclusion. In previous literature, synthesized jarosites with mixed phases containing low amounts of silver [0.115% (Patino et al, 1988); 0.135% (Cruells et al, 2000)] were obtained through the use of $1.44 \times 10^{-3}$ and $4.8 \times 10^{-4}$ M $Ag_2SO_4$. Since jarosite samples with a higher silver content were targeted, an increased concentration of $Ag_2SO_4$ was used during synthesis. The concentrations of silver sulfate (0.04 M for high-silver samples, 0.01 M for low silver samples) were arbitrarily selected, with the remainder of the 0.1 M being made up by potassium or sodium sulfate depending on the sample. 500 mL of distilled water was used for each solution, which was loaded into the autoclave, before being sealed and heated to 140$^{o}$C for 2 hours, while mixed at 500 rpm by a single, bottom impeller. The autoclave was allowed to cool down to room temperature, and the precipitate was vacuum filtered. The filter cake was water-washed 4 times (500 mL per wash), and dried at 70$^{o}$C for 24 hours. Every batch test produced approximately 25 grams of material. 500 grams of each jarosite sample was synthesized through multiple synthesis steps, and products from individual runs were blended together.

### 3.2.2 Scanning Electron Microscope (SEM)

SEM tests were conducted to examine the crystallinity and give a qualitative visual representation of the particle size and shape of the synthesized jarosite material. A representative 1 gram sample of each jarosite was obtained for SEM work. No pulverizing of the jarosite material was required as the samples were generally very fine. Samples were taken to the SEM lab, located in the Department of Materials Engineering. A single layer of jarosite powder was placed onto the surface of a large, flat pin before coating with a layer of gold/palladium under pressure, which was thinned using argon gas.

Additionally, a representative 1 gram sample of each synthesized jarosite was obtained for elemental distribution analysis (EDX) of the mineral forming elements: silver, iron, and

potassium/sodium. This experiment was done to examine if distributions of the elements, particularly silver, were uniform, clustered, or layered, etc. Samples were placed in a small plastic container and mixed with graphite (of the same particle size) in order to prevent clumping of the particles. Resin was poured over the sample and allowed to set overnight. The hardened pieces of resin were then polished in 4 stages, followed by a final diamond polish, and a carbon coating.

### 3.2.3 X-ray Diffraction

The samples were mounted "as is" in standard Bruker sample holders. Step-scan X-ray powder-diffraction data were collected over a range 3-80°2θ with CoKα radiation on a Bruker D8 Advance Bragg-Brentano diffractometer equipped with an Fe monochromator foil, 0.6 mm (0.3°) divergence slit, incident- and diffracted-beam Soller slits and a LynxEye-XE detector. The long fine-focus Co X-ray tube was operated at 35 kV and 40 mA, using a take-off angle of 6°. The X-ray diffractograms were analyzed using the International Centre for Diffraction Database PDF-4 and Search-Match software by Bruker. X-ray powder-diffraction data of the samples were refined with Rietveld program Topas 4.2 (Bruker AXS).

### 3.2.4 Surface Area and Porosity Analysis

Surface area and porosity analysis was carried out on the Quantachrome Autosorb-1MP. The Autosorb operates by measuring the quantity of gas, usually nitrogen, adsorbed/desorbed from the solid surface. The test is conducted by admitting/removing a known amount of gas into a sample cell at a constant temperature, below the critical point of the gas. The pressure in the sample cell changes until equilibrium is established. At equilibrium, the quantity of gas adsorbed/desorbed is obtained from the difference between the amount added/removed and the amount required to fill the void space. The resulting gas volume/pressure data can be processed by the software to provide information such as the adsorption/desorption isotherms, surface area, and the pore size and volume distributions. For these calculations a reference value, $P_0$, is used. This pressure is the vapour pressure of the gas used as an adsorbent, or the pressure exerted by a gas when in contact with its liquid form. This reference value was measured by the Autosorb-1 on the $P_0$ station. The sample cell station pressure is referred to as P. Varying $P/P_0$

values in the range from 0 to 1 can be used by the Autosorb-1, depending on the type of analysis to be conducted. Nitrogen gas was used for all experiments carried out for the purpose of this thesis.

A 12-point nitrogen adsorption test was conducted for jarosite samples. Data points at relative pressures of $P/P_o$ = 0.1, 0.15, 0.2, 0.25, 0.3, 0.4, 0.5, 0.6, 0.7, 0.8, 0.9, and 0.995 were gathered. A more complex 132-point nitrogen adsorption/desorption analysis extending down to $P/P_o = 8.81 \times 10^{-7}$ was conducted on the two potassium jarosite samples. Such very low pressures can reliably be reached and measured with the instrument thanks to a 1-mm Hg pressure transducer. The 12-point adsorption isotherms were used for the calculation of the multipoint Brunauer–Emmett–Teller (BET) surface area ($m^2/g$) as well as for the pore radius and volume using the Barrett-Joyner-Halenda (BJH) method. The extended analysis was able to provide a more accurate model of pore volume and surface area distribution using the Density Functional Theory method (DFT). This approach allows for a better analysis of meso-pores. Both the specific surface area and the porosity tests followed the same procedure listed below.

A clean sample tube was accurately weighed. An approximate amount of sample was loaded into a large bulb of the 9-mm diameter tube. Samples were outgassed for 24 hours ($10^{-6}$ mmHg) at room temperature and backfilled with nitrogen. After outgassing, sample cells were weighed again, in order to determine the actual mass of jarosite. For the 5 samples, the mass varied from 3.5 to 4 grams. The sample cell was loaded onto the analysis port of the Autosorb-1. Each 12-point adsorption test took approximately 1 hour to run, while the more complex 132-point analysis took 24 hours. Care was taken when attaching tubes to both outgassing and analysis ports, using a small amount of high pressure sealant grease in order to ensure a tight seal.

### 3.2.5 Particle Size Analysis

All 5 jarosite samples underwent particle size analysis using the Malvern Mastersizer 2000. The Malvern Mastersizer is a laser scattering instrument that uses the known refractive index of a material (jarosite $n_\omega$=1.8175 $n_\varepsilon$=1.7145) and an optical unit to capture multiple snapshots of the light scattering pattern from a field of particles. Jarosite has two refractive index due to being a uniaxial mineral with a single optical axis. Then, using the Mie theory

developed for spherical particles, the software is able to calculate the size of particles that created a given scattering pattern.

To prepare a sample for analysis, 0.5 g of mineral was added to 100 mL of distilled water and continuously mixed using a magnetic stir bar. Using an eye dropper, small aliquots were carefully taken from various depths and locations in the suspension (to ensure the representativeness of the sampling) while continuously mixing, and added to the Malvern sampling cell. Samples were run with 30 seconds of ultrasound treatment between readings, and the readings continued until the difference in size for the volume average particle size became less than 0.1 microns between consecutive runs. This procedure was followed to eliminate false results obtained from agglomerates and to ensure that a statistically-representative particle size distribution was obtained. An approximation of the specific surface area was also obtained from the particle size distributions, which can be compared with the direct BET surface area results. Since the Malvern unit provides a particle size distribution assuming a spherical shape of the particles, a value of the specific surface area calculated from the distribution will effectively give only the external surface area and will not account for the porosity of the sample.

### 3.2.6 Zeta Potential

Zeta potential measurements on the ZetaView PMX100 (ParticleMetrix GmbH, Germany) were conducted to determine the surface charge characteristics of synthesized jarosite samples. The ZetaView uses a laser scattering microscope and a video camera to capture particle movement in an applied electrical field (electrophoresis). From this video the software is able to derive velocity distributions, which are used to calculate electrophoretic mobility, and in turn the zeta potential, using the Smoluchowski equation (2.16). As previously stated, the Smoluchowski equation applies to a thin electric double layers with respect to particle size and is typically valid when $\kappa a > 200\text{-}300$. Zeta potential measurement for this thesis were conducted with 0.01 M sodium nitrate ($NaNO_3$). The Debye length ($\kappa^{-1}$) can be calculated by using Equation 2.11, resulting in $\kappa^{-1} = 0.00304$ µm. The average particle size of jarosite material synthesized for this thesis is roughly 40 µm (Section 4.4). Therefore $\kappa a$ is on the order of 13,000, and the use of the Smoluchowski equation for zeta potential is justified.

Experiments were conducted by preparing 0.04 mg of jarosite sample in 100 mL of 0.01 M sodium nitrate. Tests were conducted at several pH values in the range from 2 to 10, using either sodium hydroxide (NaOH) or nitric acid ($HNO_3$) for pH modification. Samples were mixed at 200 rpm for one hour, with additional pH adjustments taking place every 10 minutes, or as needed, in order to reach a steady-state target value. After mixing, samples were subject to a 2 minute ultrasonic bath treatment and tested right away. All 5 jarosite samples underwent baseline zeta potential characterization.

### 3.2.7 Hallimond Tube Flotation and Surfactant Adsorption using Total Carbon Analysis

Hallimond tube flotation tests and surfactant adsorption analysis were done in combination, using the same conditioned sample for both. Tests were duplicated, with each run measuring the total organic carbon (TOC) and reporting the average of 3 readings.

The TOC operates by passing a carrier gas (purified air) at a controlled flow rate (150 mL/min) through an oxidation catalyst-filled total carbon (TC) combustion tube heated to 680$^{o}$C. The sample solution is automatically injected into the combustion tube where the TC is oxidized or decomposes to create carbon dioxide ($CO_2$). The combustion tube products carried by the carrier gas are cooled and dehumidified, pass through a halogen scrubber before entering the non-dispersive infrared detector (NDIR) cell. The NDIR detects $CO_2$ and its analog signal forms a peak, from which the data processors are able to calculate the area under the peak. Using a calibration curve the software is able to convert this peak area to the TC concentration.

Flotation and adsorption tests were run at pH 3.5 (natural) and pH 10. For experiments conducted at an unmodified pH of 3.5, 2 grams of jarosite was added to 10 mL of distilled water and mixed at 200 rpm for 1 hour. Another 20 mL of the tested surfactant solution, of a given concentration, conditioned to pH 3.5 in the background $NaNO_3$ were then added to the mixture, and conditioned at 200 rpm for an additional 1 hour.

Due to the natural tendency of jarosites to equilibrate to pH of 3-4 in colloidal suspensions (Zahrai et al, 2013), a procedure was developed in an attempt to stabilize a jarosite mixture at pH 10 for the duration of the test. If 2 grams of jarosite is left to condition in 30 mL

of a solution with pH 10, the solution becomes increasingly acidic within minutes, and pH decreased to ~4 within an hour. This solution acidification was also noted by Smith et al (2006) for alkaline dissolution tests. This rapid decrease in pH was offset with staged small additions of a background solution with pH 11. Increasing the pH too rapidly was deliberately avoided due to the enhanced dissolution of jarosite that occurs under more alkaline conditions (Reyes et al, 2017). Roca et al (1993) state that the beginning of jarosite dissolution under alkaline conditions was marked by a shift from its original yellowish-orange colour to red. For experiments conducted at pH 10, 2 grams of jarosite was added to 8 mL of 0.01M $NaNO_3$ at pH 10, and 1 mL of 0.01M $NaNO_3$ [pH 11] was added every 10 minutes (7 mL total). 15 mL of reagent solution was then added to reach a final volume of 30 mL at a desired surfactant concentration. Reagents were tested at various concentrations between 0-300 mg/L. The pH was monitored before and after surfactant addition and was found to be stable within 0.2 pH units in all cases over the timescale of the test.

After conditioning, contents of the beakers were transferred to glass vials and centrifuged for 1 hour at 9000 rpm (3000 g-force). Although the centrifuging time and acceleration were chosen arbitrarily, those parameters consistently resulted in a very sharp solid-liquid separation. Liquid was syringed off the top of every vial for examination in the total carbon analyzer (TOC). The remaining sample, including all the solids was used for Hallimond tube flotation experiments.

The remaining liquid and conditioned solids in the centrifuge tube were poured into the bottom of a Hallimond tube (Figure 3-7) setup. 0.01 mol/L sodium nitrate solution adjusted with $HNO_3$ to pH 3.5 or NaOH to pH 10, was used to fill up the Hallimond tube (150 mL). A small magnetic stir bar was used to gently agitate the bed of material at the bottom of the flotation cell. Compressed nitrogen flow was opened and the flotation was allowed to run for a total of 2 minutes, or for only 45 seconds to qualitatively assess the effect of the reagents on the kinetics of flotation. Both floated and the un-floated material was filtered, dried at 70$^{o}$C for 12 hours, and then separately weighed to determine the percentage of minerals floated.

Figure 3-7: Hallimond Tube for Flotation Test.

For TOC analysis of residual surfactant concentrations, all solution samples were acidified to pH 2.5 using nitric acid ($HNO_3$) and heated to 30$^oC$ for 8 minutes in order to drive off any carbon dioxide potentially forming at low pH from inorganic sources, mainly carbonates. This step ensured that the total organic carbon measured in each sample originated entirely from the organic surfactants. The TOC values were then easily converted to the concentration of the remaining reagent in solution, using reagent-specific TOC calibration curves. For both sodium dodecyl sulfate and octanohydroxamic acid, 5 mL of the aqueous phase was syringed off and acidified with 15 mL 0.01 M $NaNO_3$ (pH 2.5). Dilutions were carefully controlled in order to properly convert carbon readings back to the undiluted source. Since lauric acid readily forms colloidal precipitates at low pH, sample solutions of lauric acid were diluted 60-fold (0.33 mL sample with 19.67 mL of 0.01M $NaNO_3$ (pH 2.5)) in order to avoid any analytical issues associated with analysis of colloidal particulate matter in the Shimadzu TOC analyzer. The TOC results for samples containing colloidal precipitates were essentially impossible to reproduce, while the dilution of those solutions resulted in highly reproducible TOC results.

Background carbon values of all jarosite samples were measured by mixing 2 grams of material in 30 mL of 0.01M $NaNO_3$ for 1 hour at 200 rpm. The background TOC levels were found to be insignificant for all samples. Total organic carbon values for distilled water, nitric acid [pH 2], and sodium hydroxide [pH 10 and 11] were also measured and subtracted from the results obtained during adsorption experiments. Carbon concentrations for the stock solutions of each surfactant were also determined in order to verify the actual initial dosage. This step was particularly important for lauric acid solutions, as they required the above-mentioned high dilution, in order to minimize the initial experimental error involved in preparing a stock solution at an assumed concentration, and in doing so to improve the overall accuracy of the TOC data. Analysis of carbon values before and after adsorption in solution in equilibrium with the solids allows the adsorption of a reagent onto the jarosite particles to be assessed from the difference between the initial concentration (known) and residual/equilibrium after adsorption (measured). Adsorption results are presented in two ways. For direct correlation with the flotation data, the results are shown as the adsorption density of the surfactant as a function of the *initial* surfactant concentration (equal to the dosage in flotation). The more usual presentation – the adsorption densities as a function of the *residual* concentrations – is given in the appendix.

### 3.2.8 Contact Angle Measurements

The First Ten Angstroms FTA 1000 drop shape instrument uses a mounted camera to take a profile-view snapshot of a droplet on the surface of a solid. Based on the acquired image, the software is able to calculate the contact angle of the liquid (surfactant solution) on the tested surface. This method is known as the sessile drop method. Alternatively, the tested surface can be immersed in the studied liquid and a gas bubble can be brought into contact with the surface. In this approach, known as the captive bubble method, the contact angle is established from the shape of the gas bubble.

Since jarosite minerals were synthesized as very fine powders, the initial approach was to compress the powders into larger pellets, which could then be used for contact angle measurements. All attempts to pelletize jarosite powders for contact angle tests were unsuccessful. Pellets compressed at 4500 psi crumbled immediately on contact with liquid. A modified sessile drop method from Kaushik (2012) was then employed for contact angle

measurements. Jarosite material was conditioned following the procedure listed in 3.2.7. Select doses were chosen based upon the Hallimond tube and adsorption results, in order to reinforce trends shown in those tests. After conditioning under the same conditions as those of the flotation tests, samples were filtered using 0.1 micron filter paper. The filter paper was pre-washed with 200 mL of water to ensure no contaminants were leached from the paper. The solids on the filter paper were washed with 90 mL of distilled water in order to displace any excess surfactant solution from the bed of the particles as to not influence contact angle results. It should be noted that in this method, the solids are conditioned with the surfactants, and the resulting wettability is measured using a droplet of water placed on the bed of filtered solids. Conditioned samples were placed between two glass slides and gently compressed by hand. This simple step produced a flat-bed surface when the top slide was removed. The glass slide with the flattened material was placed on the sample stand of the First Ten Angstroms FTA 1000 drop shape instrument. A pipette was used to administer a single droplet of 0.01M $NaNO_3$ solution, which was adjusted to the correct pH, on the surface of the jarosite bed. If a droplet formed, indicating significant hydrophobicity of the bed, an image was taken within 5 seconds, and the contact angle was measured using the instrument software. For less hydrophobic samples, the droplet would quickly penetrate into the bed of particles without forming a contact with the bed. The measurements were performed in triplicates.

Results from this method should not be viewed as quantitatively accurate. They are used as an indicator of the relative hydrophobicity of the tested jarosite powders in the presence of the surfactants. Results offered either large contact angles (>100$^o$) or complete wetting of the bed. This is due to the fact that the "flat surface" formed for bubble placement is a thin bed of particles exhibiting substantial surface roughness and porosity, which can be viewed as a bundle of capillaries. The behaviour of a liquid on a bed of fine particles can be described by the following equation for the rate of penetration of a liquid into a compact layer of particles (Washburn, 1921):

$$\frac{l^2}{t} = \frac{r\gamma\cos(\theta)}{2\eta} \tag{3.1}$$

Where $l$ is the depth of liquid penetration, $r$ is the uniform internal radius of a single capillary at time $t$, $\gamma$ is the surface tension of the liquid, $\theta$ is the contact angle between the particle surfaces and the penetrating liquid, and $\eta$ is the viscosity of the liquid. A simple analysis of the Washburn equation shows that for a contact angle of $0^o$, the rate of penetration is at a maximum. As the contact angle increases, the rate of penetration gradually decreases and becomes zero when a contact angle of $90^o$ is reached. At contact angles larger than $90^o$, the penetration rate becomes negative. In this case, the droplet will sit on the bed surface without penetrating it, and it is now possible to directly measure the shape of the droplet and the corresponding contact angle. As a result of these phenomena, this method gave contact angles of either $>100^o$ or no values could be recorded. During these experiments, a bed of particles with a contact angle of $0^o < \theta < 90^o$ would gradually absorb the liquid, although with different rates, and no stable droplet for shape analysis could be obtained. Alternatively, if sufficient amounts of jarosite powders were available, the rates of penetration could be measured in a column packed with jarosite particles (which presents a separate set of measurement problems) to obtain those intermediate contact angle values. Since these tests were performed only for qualitative purposes, and with the limited amount of synthesized powders, it was decided to adapt the simplified approach.

## 4.0 Results and Discussion

### 4.1 Characterization of Jarosite Samples.

#### 4.1.1 Visual Appearance of the Samples

All synthesized jarosite samples were yellow-orange in colour and appeared identical (Figure 4-1 and Figure Figure *4-2*). No clear distinction could visually be made between them.

Figure 4-1: Synthesized Sodium (Baseline) Jarosite (left). Synthesized Low-Silver Sodium Jarosite (centre). Synthesized High-Silver Sodium Jarosite (right).

Figure 4-2: Synthesized Potassium (Baseline) Jarosite (left). Synthesized High-Silver Potassium Jarosite (right).

Samples were conditioned to a range of pH values [2, 4, 6, 8, 10, 12] in order to identify if any visible changes occurred. All jarosite samples reacted identically to shifts in pH, with a slight darkening in colour was observed at pH 8, darkening further at pH 10, before severe

reddening occurred at pH 12. Figure 4-3 shows this effect in drained baseline potassium samples. A darkening in colour was reported as a sign of jarosite dissolution and goethite precipitation on the surface of jarosite (Roca et al, 1993; Smith et al, 2006; Zahrai et al, 2013).

Figure 4-3: Effect of pH on Potassium Jarosite (Baseline) Mineral Colour [pH 2, 4, 6, 8, 10, 12 from left to right].

### 4.1.2 Scanning Electron Microscope (SEM)

Scanning electron images revealed fine crystalline structures for all synthesized jarosite samples (Figure 4-4, Figure 4-5, and Figure 4-6).

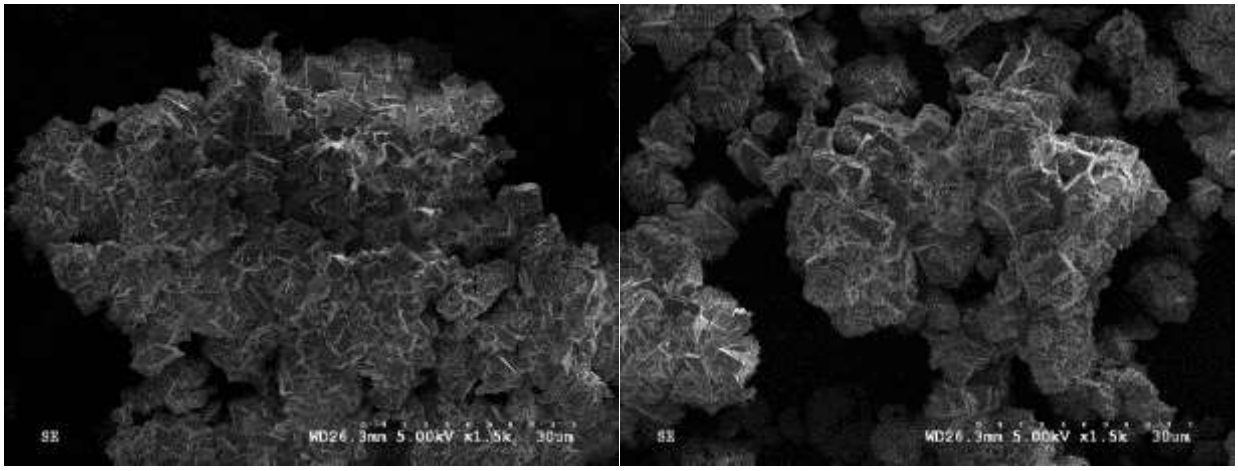

Figure 4-4: Scanning Electron Microscope. Sodium (Baseline) Jarosite (left), Low-Silver Sodium Jarosite (right).

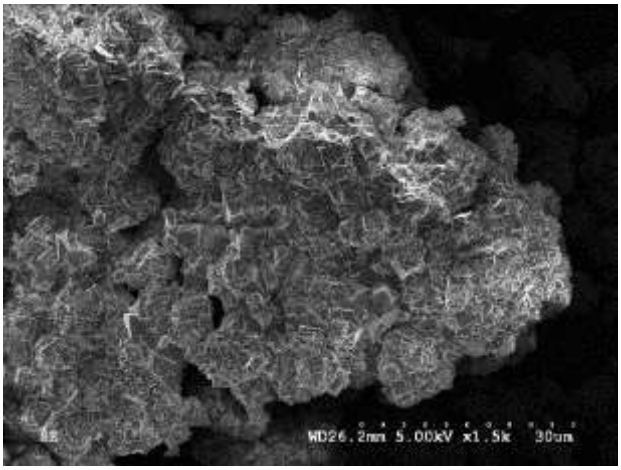


Figure 4-5: Scanning Electron Microscope. High-Silver Sodium Jarosite.

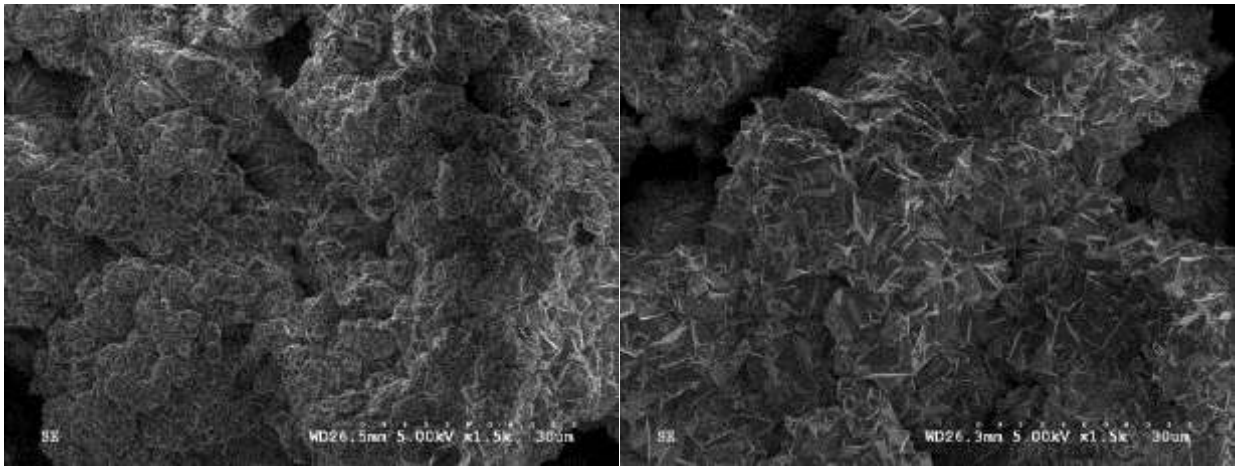


Figure 4-6: Scanning Electron Microscope. Potassium (Baseline) Jarosite (left), High-Silver Potassium Jarosite (right).

Elemental distributions of iron, and sodium/potassium for both baseline samples revealed even distributions of sodium/potassium throughout. The high silver samples of sodium/potassium demonstrated an even distribution of sodium/potassium, iron, and silver (Figure 4-7 and Figure 4-8). In all tested cases, the low silver sodium sample exhibited a rimming of sodium, with centrally distributed silver and evenly distributed iron (Figure 4-9). Since the rimming contains sodium and iron, it appears that the low-silver sodium jarosite sample is coated with a silver-deficient layer of a sodium jarosite phase. This Ag-deficient coating is not present in samples with a higher silver content.

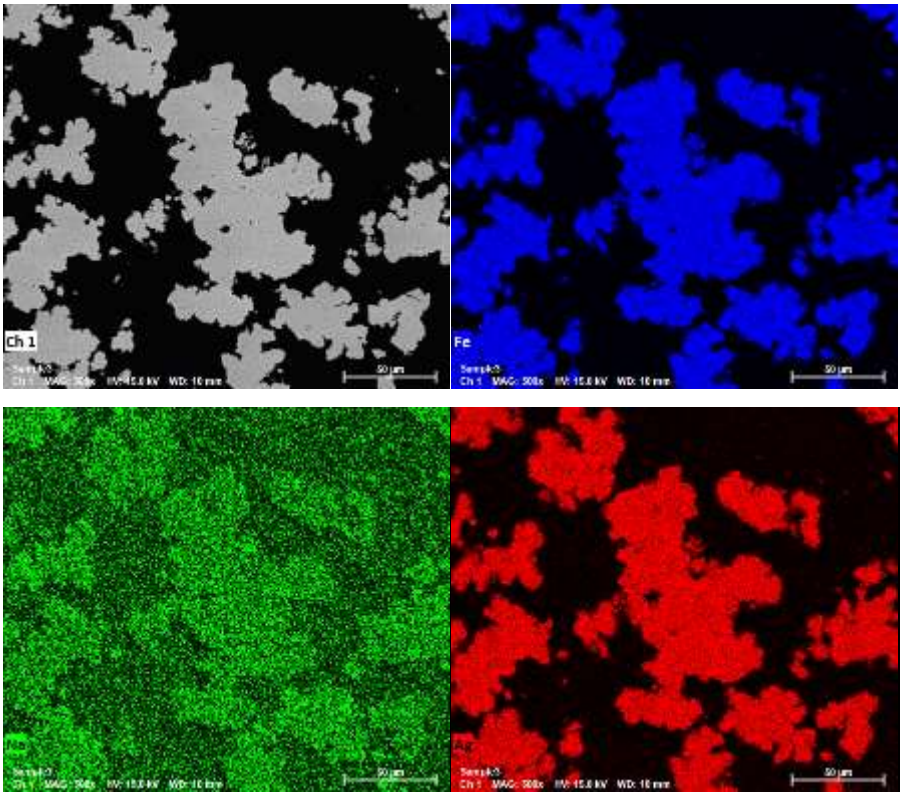


Figure 4-7: High-Silver Sodium Jarosite Elemental Distribution. Grey-scale Electron Back-scattered Image (top left). Iron (top right). Sodium (bottom left). Silver (bottom right).

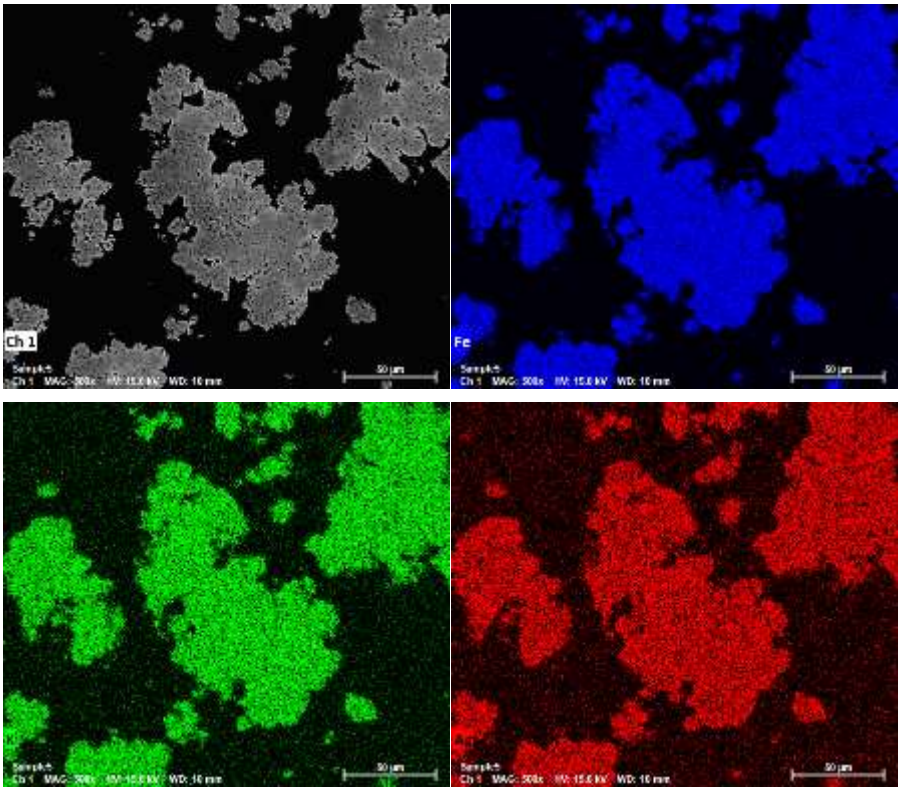


Figure 4-8: High-Silver Potassium Jarosite Elemental Distribution. Grey-scale Electron Back-scattered Image (top left). Iron (top right). Potassium (bottom left). Silver (bottom right).

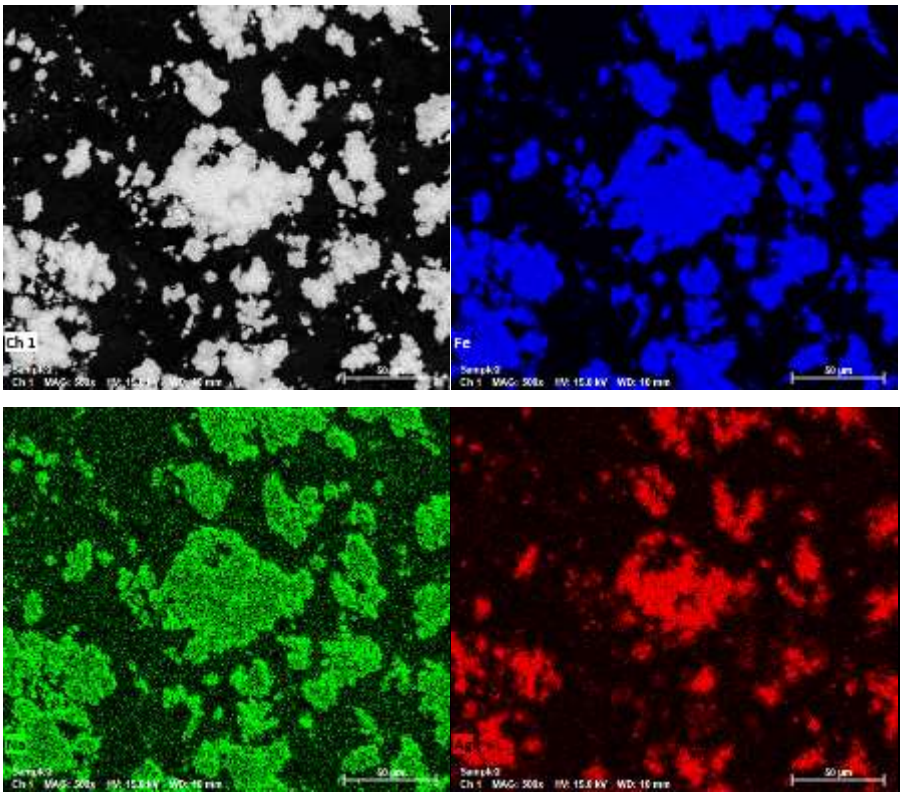


Figure 4-9: Low Silver-Sodium Jarosite Elemental Distribution. Top Left – Grey-scale Electron Back-scattered Image (top left). Iron (top right). Sodium (bottom left). Silver (bottom right). Note the apparent presence of a silver-deficient, sodium-rich layer on the particles surface.

### 4.1.3 Mineralogical Assay

Samples of synthesized jarosites were sent to a commercial lab in Vancouver for elemental assays. Duplicate assays were conducted to verify the consistency of the samples. Individual elemental contents were back-calculated from the provided major oxide assays. Results are shown in Table 4-1. These values are comparable to the theoretical assay values for jarosite minerals (Table 4-2).

It should be noted that the iron contents in all the samples are essentially the same, and only the sodium and/or potassium contents are affected by the addition of silver. This observations suggests that silver replaces the monovalent alkali metals in the crystal structure of jarosite. This trend is reflected in the back-calculated stoichiometric formula of each jarosite, where the sum of the coefficients of all monovalent cations ($K^+/Na^+$, $Ag^+$, and $H_3O^+$) adds up to 1.

Table 4-1: Synthesized Jarosite Assays.

| Sample | # | Fe (%) | Na (%) | K (%) | Ag (%) | S (%) |
|---|---|---|---|---|---|---|
| Baseline Na-Jarosite | 1 | 33.42 | 3.23 | - | - | 13.41 |
| | 2 | 32.70 | 3.15 | - | - | 13.41 |
| Low Silver Na-Jarosite | 1 | 32.03 | 1.99 | - | 3.56 | 12.62 |
| | 2 | 32.55 | 1.99 | - | 3.38 | 12.86 |
| High Silver Na-Jarosite | 1 | 29.80 | 0.47 | - | 12.73 | 12.01 |
| | 2 | 29.52 | 0.45 | - | 12.94 | 11.83 |
| Baseline K-Jarosite | 1 | 30.51 | - | 6.81 | - | 12.32 |
| | 2 | 29.77 | - | 6.40 | - | 12.31 |
| Silver K-Jarosite | 1 | 30.26 | - | 3.93 | 5.65 | 11.25 |
| | 2 | 30.30 | - | 4.12 | 5.46 | 11.96 |

Table 4-2: Theoretical Elemental Composition.

| Mineral | S (%) | Ag (%) | Fe (%) | Na (%) | K (%) |
|---|---|---|---|---|---|
| Natrojarosite ($NaFe_3(SO_4)_2(OH)_6$) | 13.23 | - | 34.57 | 4.74 | - |
| K-Jarosite ($KFe_3(SO_4)_2(OH)_6$) | 12.81 | - | 33.45 | - | 7.81 |
| Argentojarosite ($AgFe_3(SO_4)_2(OH)_6$) | 11.26 | 18.94 | 29.41 | - | - |

Values for the theoretical elemental compositions, listed in Table 4-2, are calculated by observing that every 1 mole of M-jarosite (M = Na, K, or Ag) ($MFe_3(SO_4)_2(OH)_6$) contains 1 mole of the M-site cation, 3 moles of iron, 2 moles of sulfate (equating to 2 moles of sulfur and 8 moles of oxygen), and 6 moles of hydroxide (equating to 6 moles of both oxygen and hydrogen). The molar mass (g/mol) of jarosite can then be calculated with Equation 4.1 by inserting the molar masses for M (Na = 22.98977 g/mol, K = 39.0983 g/mol, or Ag = 107.8682 g/mol), iron (Fe = 55.845 g/mol), sulfur (S = 32.066 g/mol), oxygen (O = 15.9994 g/mol), and hydrogen (H = 1.0074 g/mol).

$$\text{M-Jarosite Molar Mass} = \text{Molar Mass of}\left([M]+[3\times Fe]+[2\times S]+[14\times O]+[6\times H]\right) \quad (4.1)$$

This results in a molar mass of 484.69 g/mol for sodium jarosite, 500.80 g/mol for potassium jarosite, and 569.57 g/mol for silver jarosite. Using these calculated molar masses, along with the known molar masses of individual elements, the theoretical elemental composition of each M-jarosite (Table 4-2) can be calculated by using Equation 4.2.

$$\text{Element (\%)} = 100 \times \left( \frac{\text{\# of moles} \times \text{Molar Mass of Element} \left( \frac{g}{mol} \right)}{\text{Molar Mass of Jarosite} \left( \frac{g}{mol} \right)} \right) \quad (4.2)$$

If a 1 gram sample of M-jarosite is taken, the number of moles of each element can be calculated by dividing the elemental assay by 100 and dividing it by the molar mass of that element. The molecular formula for each synthesized jarosite sample (Table 4-3) was back-calculated using an average of the two chemical assays reported in Table 4-1.

Table 4-3: Synthesized Jarosite Back-Calculated Formulas.

| Sample | Formula |
|---|---|
| Sodium Jarosite (Baseline) | $(Na_{0.656},H_3O^+_{0.304})Fe_3(SO_4)_2(OH)_6$ |
| Low-Silver Sodium Jarosite | $(Na_{0.453},Ag_{0.168},H_3O^+_{0.379})Fe_3(SO_4)_2(OH)_6$ |
| High-Silver Sodium Jarosite | $(Na_{0.112},Ag_{0.669},H_3O^+_{0.216})Fe_3(SO_4)_2(OH)_6$ |
| Potassium Jarosite (Baseline) | $(K_{0.928},H_3O^+_{0.072})Fe_3(SO_4)_2(OH)_6$ |
| High-Silver Potassium Jarosite | $(K_{0.570},Ag_{0.249},H_3O^+_{0.181})Fe_3(SO_4)_2(OH)_6$ |

Assuming every mole of jarosite has 3 moles of iron, the number of iron moles can be divided by 3 to estimate the total number of monovalent metal moles present in the 1 gram sample. Dividing the number of sodium, potassium, or silver moles in the 1 gram sample by the total monovalent metal moles for each sample gives the percentage of the M-site that is occupied by each. Hydronium substitution is stated in literature as always being present during jarosite synthesis (Basciano, 2008; Grey et al, 2013) and is therefore assumed to make up the remaining part of the structure. A similar method can be employed using sulfur assays and assuming every mole of jarosite contains 2 moles of sulfur. Results using this method produce

similar molecular formulas, as both iron and sulfur are constant and assays fall close to theoretical values.

### 4.1.4 X-ray Diffraction

The results of the phase analysis by Rietveld refinements are given in Table 4-4. Rietveld refinement plots for the five jarosite samples X-ray spectrums, as well as unit cell parameters identified by X-ray diffraction are located in the appendix (Section 8.2). The baseline sodium and low-silver sodium jarosites were fit to two different spectra, indicating two slightly different compositions. The remaining samples were fit to a single spectrum. Hydronium substitution was noted as being present in all samples.

Table 4-4: X-ray Diffraction Phase Analysis.

| **Sample** | **Ideal Formula** | **%** |
|---|---|---|
| Sodium Jarosite (Baseline) | $(Na,H_3O^+)Fe_3^{3+}(SO_4)_2(OH)_6$ | 76 |
| | $(Na,H_3O^+)Fe_3^{3+}(SO_4)_2(OH)_6$ | 24 |
| Low-Silver Sodium Jarosite | $(Na,Ag,H_3O^+)Fe_3^{3+}(SO_4)_2(OH)_6$ | 57 |
| | $(Na,Ag,H_3O^+)Fe_3^{3+}(SO_4)_2(OH)_6$ | 43 |
| High-Silver Sodium Jarosite | $(Ag,Na,H_3O^+)Fe_3^{3+}(SO_4)_2(OH)_6$ | 100 |
| Potassium Jarosite (Baseline) | $(K,H_3O^+)Fe_3^{3+}(SO_4)_2(OH)_6$ | 100 |
| High-Silver Potassium Jarosite | $(K,Ag,H_3O^+)Fe_3^{3+}(SO_4)_2(OH)_6$ | 100 |

## 4.2 Surface Area and Porosity

The BET and Malvern Mastersizer surface areas for all synthesized jarosite samples were low (<1 $m^2/g$). The measured values are shown in Table 4-5 along with the calculated average BJH pore radius and volume. Previously recorded jarosite surface areas are in a footnote to the table for comparison with values obtained for the purposes of this thesis.

The BET surface areas of jarosite slightly decreases with the inclusion of silver. Potassium jarosites have slightly lower surface areas than the corresponding sodium jarosites. The average BJH pore radii also decreased in samples containing silver, with potassium samples having marginally lower pore radius than sodium samples.

Table 4-5: BET Surface Area and BJH Pore Radius of 5 Synthesized Jarosite Samples.

| Sample Name | M Cation | BET Surface Area ($m^2/g$) | Malvern Surface Area ($m^2/g$) | Average BJH Method Pore Radius (A) | Average BJH Method Pore Volume (cc/g) |
|---|---|---|---|---|---|
| Sodium Jarosite (Baseline) | Na | 0.3583 | 0.414 | 30.93 | 0.0021 |
| Low Silver Sodium Jarosite | Na/Ag | 0.3266 | 0.388 | 18.26 | 0.0018 |
| High Silver Sodium Jarosite | Na/Ag | 0.2944 | 0.368 | 18.28 | 0.0017 |
| Potassium Jarosite (Baseline) | K | 0.3077 | 0.413 | 20.94 | 0.0015 |
| High Silver Potassium Jarosite | K/Ag | 0.2741 | 0.429 | 15.75 | 0.0014 |

Literature data for synthetic jarosites: Dutrizac (2010): 0.42 m2/g for potassium jarosite, Cruells et al. (2000) 1.0-1.7 m2/g for silver/potassium jarosite, Forray et al. (2010) 1.03 $m^2/g$ for lead jarosite, and Wang et al. (2007) 0.30-1.11 $m^2/g$ for ammonium jarosite.

The more involved 132-point adsorption/desorption test offers a detailed plot of individual distributions as well as the cumulative pore volume (Figure 4-10) and surface area (Figure 4-11) as a function of pore radius (half pore width), using the DFT method. The results show that the majority of pore volume and surface area is present in meso-pores (2-80 Angstrom radius). For baseline potassium, the total surface area was 0.3077 $m^2/g$ (Table 4-5) and the cumulative surface area is around 0.181 $m^2/g$ at 80A (Figure 4-11), meaning ~60% of the total surface area is contained in pores smaller than 80A. The distribution of the 2 potassium jarosite samples follows a similar trend, with the cumulative volume and surface area of the silver sample being moderately lower.

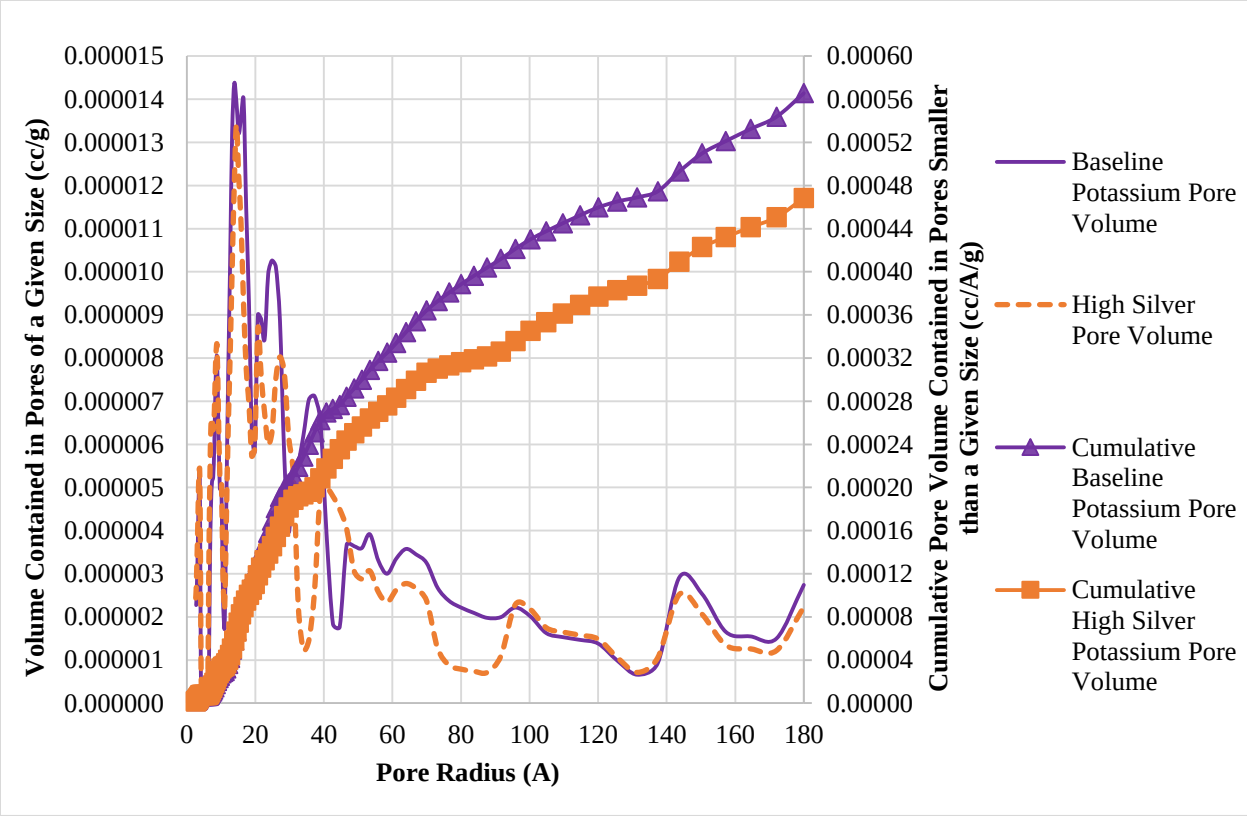


Figure 4-10: Pore Volume Distributions of Potassium Jarosite Samples (DFT Method).

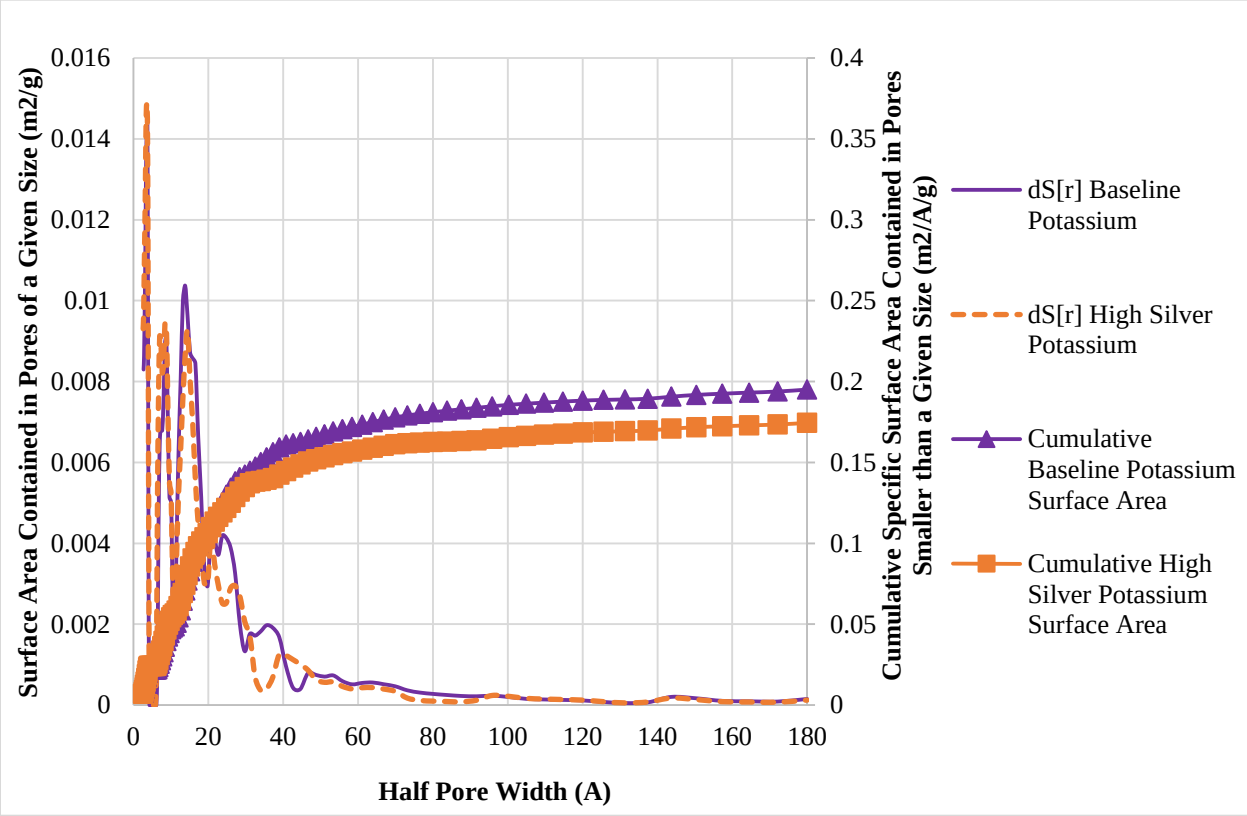


Figure 4-11: Surface Area Distributions of Potassium Jarosite Samples (DFT Method).

## 4.3 Particle Size Analysis

Particle size analysis revealed no influence of silver or difference between sodium and potassium, providing nearly identical particle size for each sample, with an average particle size of ~40 microns. Small differences can be seen between the sodium samples and the potassium samples at sizes below about 20 μm, with the sodium samples showing a higher proportion of the finer particles (~30%) than the potassium samples (~15%). The slightly finer nature of the sodium jarosites is consistent with the higher BET specific surface areas of these samples.

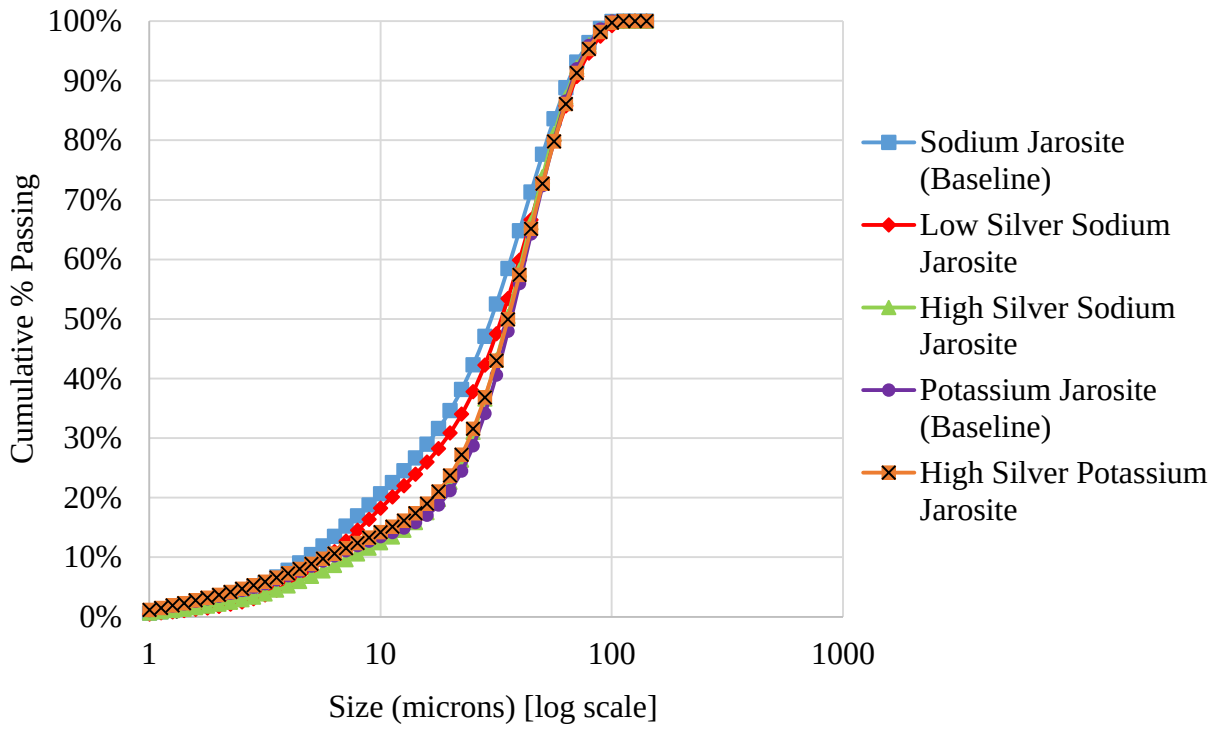


Figure 4-12: Particle Size Analysis of 5 Synthesized Jarosite Samples.

## 4.4 Zeta Potential

The zeta potential values of as-synthesized jarosite samples were measured at ten pH values in the pH range from 2 to 10 (Figure 4-13 and Figure 4-14).

Several sets of the zeta potential data of goethite available in the literature (Iwasaki et al, 1960; Li and Stanforth, 2000; Lakshmipathiraj et al, 2006) were added for comparison to help with detecting goethite precipitation on the surface of jarosite crystals at higher pH values. It should be noted that among the literature results only the data from Iwasaki et al (1960) were obtained at the same ionic strength as that used in this research.

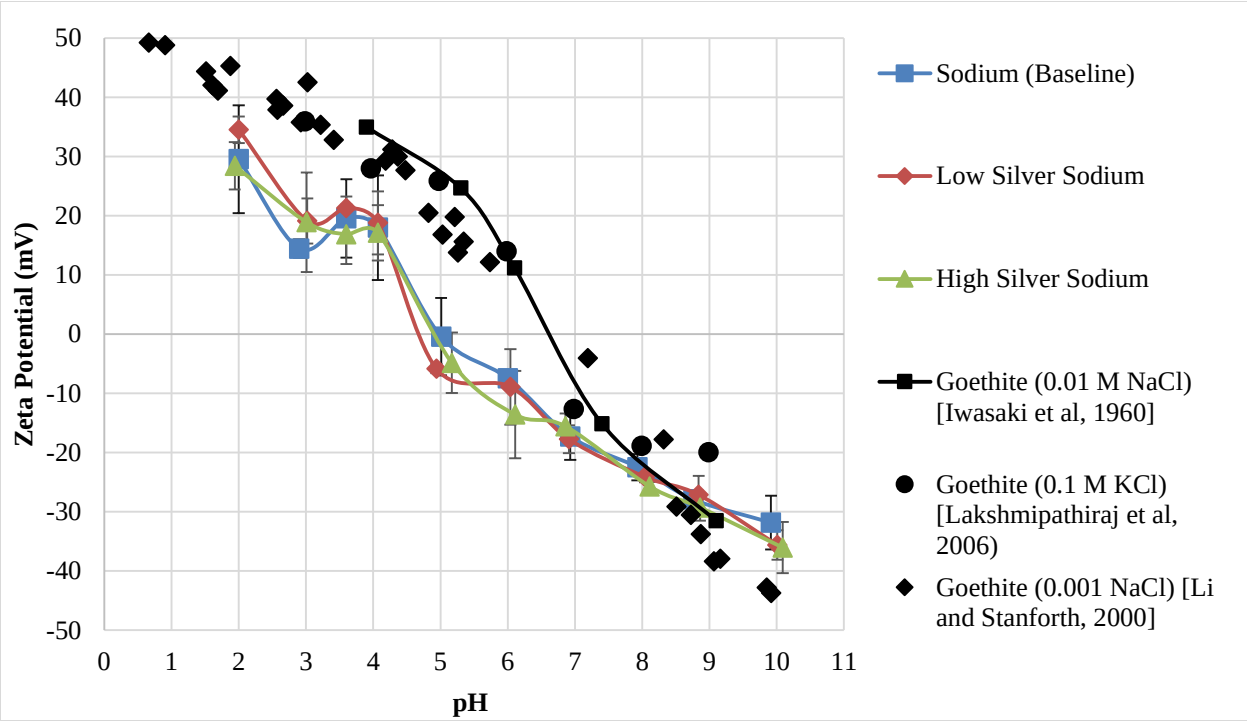


Figure 4-13: Zeta Potential Results for 3 Synthesized Sodium Jarosites (pH 2-10), along with examples of zeta potential data for goethite available in literature. The solid black trend line is drawn through the data from Iwasaki et al. (1960).

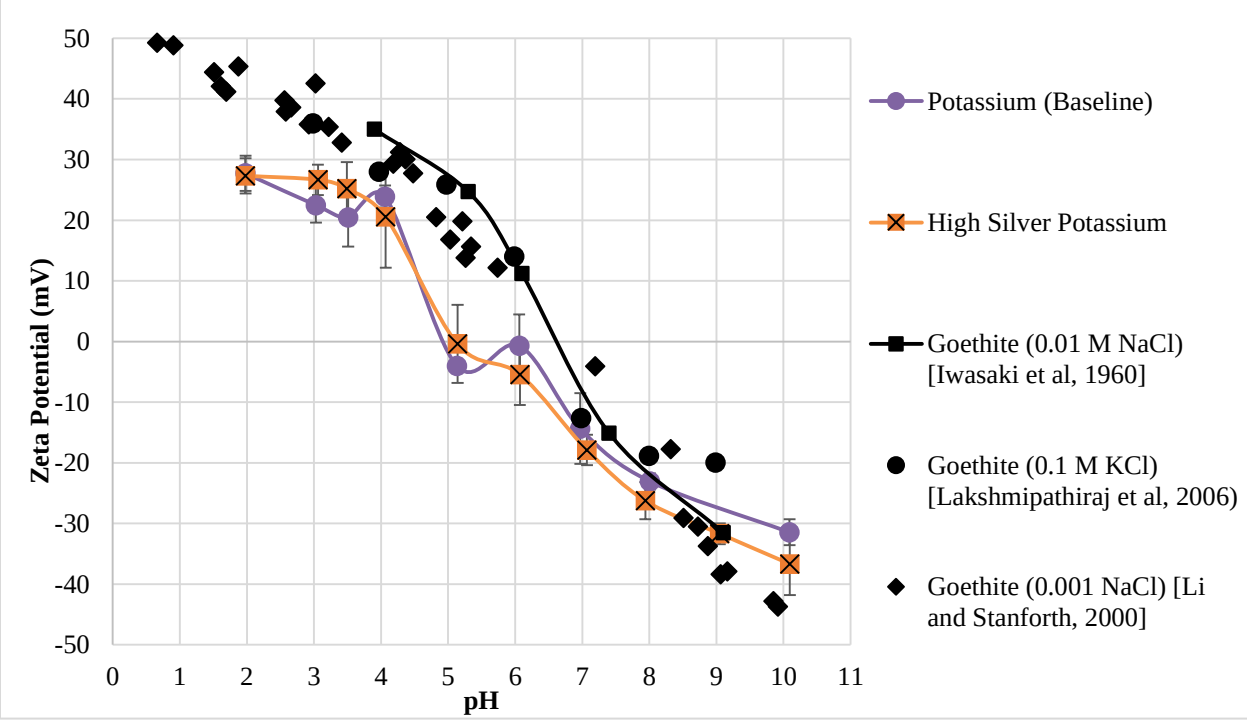


Figure 4-14: Zeta Potential Results for 2 Synthesized Potassium Jarosites (pH 2-10) along with examples of zeta potential data for goethite available in literature. The solid black trend line is drawn through the data from Iwasaki et al. (1960).

Only one isoelectric point was found for each of the 5 jarosite samples. This iep was found to be similar for all the samples (~pH 5), with a positive surface charge below pH 5 and a negative charge above it. Considering the magnitude of the experimental errors, shown as error bars in Figure 4-13 and Figure 4-14, both sodium and potassium jarosite samples have very similar surface charge profiles throughout the tested range of pH values. Most interestingly, silver inclusion appears to have a negligible effect on the surface charge characteristics of the tested samples. When the pH is greater than 7, the zeta potential of goethite starts overlapping with the zeta potential of the synthesized jarosite samples, particularly for the results from Iwasaki et al. (1960) that were obtained under the same ionic strength as the jarosite data from this research. This observation is an indication that the jarosite surfaces become coated by a goethite-like layer at higher pH values, a process which was discussed earlier in Section 2.6. The presence of goethite on the jarosite particles is also consistent with the observed colour change from yellow to red as the pH changes from 2 to 10 (Figure 4-3). When the pH is above ~3.8, dissolution of jarosite is dominated by a reaction resulting in goethite formation (Equation 2.3). As can be seen in the zeta potential results, all synthesized jarosite samples show a marked unusual shift in the results around pH 5-6 towards higher pH values, which seems to indicate a point where significant goethite formation already starts occurring on the jarosite surfaces but is difficult to detect visually.

## 4.5 Hallimond Tube Flotation and Surfactant Adsorption using Total Carbon Analysis

Reagent adsorption and Hallimond tube flotation tests were conducted at two pH values: natural (3.5) and 10, with varying initial concentrations of three reagents: lauric acid, sodium dodecyl sulfate, and octanohydroxamic acid. These reagents are discussed in Section 2.9. Lauric acid is a fatty acid. Fatty acids are commonly used as collectors for salt-type minerals (including sulfates, e.g. barite) and was selected as a representative of this group. Lauric acid is a weak electrolyte collector (similarly to hydroxamate but in contrast to dodecyl sulfate) with low solubility (in contrast to both hydroxamate and dodecyl sulfate), so in this case speciation is a function of pH and the low solubility may lead to precipitation. Dodecyl sulfate was selected due to the common sulfate anion with the jarosite surface. The assumption was that the sulfate group would show strong adsorption affinity towards the jarosite surface. Dodecyl sulfate is a strong electrolyte with high solubility in water, whose speciation is independent of pH. In other

words, this surfactant is always 100% dissociated and does not form colloidal precipitates. Lastly, a hydroxamate was chosen due its popularity as a collector for non-sulfide minerals containing heavy metals (e.g. malachite, cerussite). Hydroxamate is a weak electrolyte collector with high solubility. So in contrast to dodecyl sulfate, the speciation of hydroxamate in solution is a function of pH, but (similarly to dodecyl sulfate) the solubility is still high enough to prevent precipitation under typical flotation conditions. The chemistry of this reagent presents a more complex case than dodecyl sulfate.

Adsorption and Hallimond tube flotation results contain error bars representing the standard deviation for duplicated tests. In many cases the errors are actually smaller than the symbols used. Since Hallimond tube flotation is a small scale experiment performed on a single mineral, a clarification of terms such as “good” and “poor” flotation is required. For discussion purposes, the Hallimond tube flotation results can be broken down into 3 general subsets.

Good Flotation

Good flotation results are characterized by strong particle/bubble attachment, low turbidity of the remaining solution, and 80-100% of material floated during the 2 minute flotation time. During the test, the froth is loaded with solids, so collecting the solids at the end of the experiment without any material losses is usually very easy. An example of good flotation is shown in Figure 4-15.

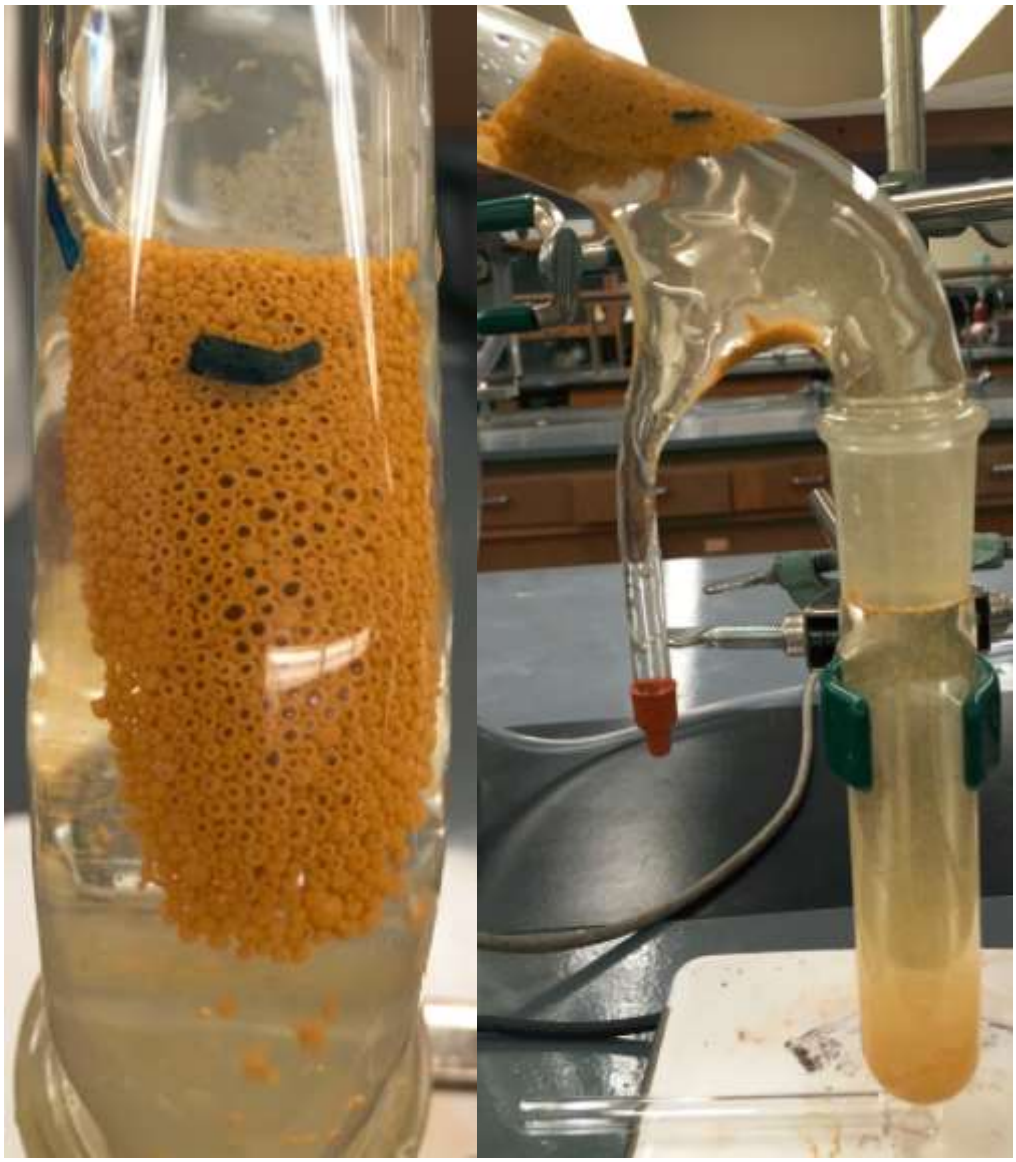

Figure 4-15: Example of Good Hallimond Tube Flotation Results. 200 mg/L Lauric Acid. pH 3.5. Top View (Left), Side View (Right).

Moderate Flotation

Moderate flotation results are characterized by lowered particle-bubble attachment, an increase in the turbidity of the remaining solution, and lowered amount of material floated (30-70%) compared to good flotation. Attachment was visible in varying degrees during these tests (the bubbles in the froth are clearly covered with solids). An example of moderate flotation is shown in Figure 4-16.

Figure 4-16: Example of Moderate Hallimond Tube Flotation Results. 50 mg/L Lauric Acid. pH 3.5. Top View (Left), Side View (Right).

Poor Flotation

Poor flotation results are characterized by the absence of clear particle-bubble interactions, lack of a well-defined froth layer, high turbidity of the solution in the tube, and very small amounts of material floated (0-30%). Any material that was floated during poor tests can be attributed to mechanical entrainment (carry-over) rather than to true flotation by attachment to gas bubbles. An example of poor flotation is shown in Figure 4-17.

Figure 4-17: Example of Poor Hallimond Tube Flotation Results. 10 mg/L Sodium Dodecyl Sulfate. pH 3.5.

### 4.5.1 Estimation of Dissolution

Based on the similar dissolution rates reported for Na/K/Ag/$H_3O^+$ jarosites (Table 2-4) It is assumed that the induction times and overall dissolution rates for both potassium and sodium jarosites containing hydronium and silver are comparable. The molecular formula coefficients

for the jarosite dissolution equations (2.4 and 2.5) were calculated by Smith et al (2006) using the measured equilibrium concentrations of $K^+$ and $Fe^{3+}$ ions (Table 2-5) as well as the standard convention of assigning sulfate a coefficient of 2. By using these coefficients and balancing the overall charge (by adjusting the coefficient of hydrogen cations), the following jarosite dissolution equations are reached (pH < 3.8 Equation 4.3; pH > 3.8 Equation 4.4):

pH < 3.8

$$KFe_3(SO_4)_2(OH)_6 + 4.3H^+ \rightarrow 1.245K^+ + 2.35Fe^{3+} + 2SO_4^{2-} + 6H_2O \quad (4.3)$$

pH > 3.8

$$KFe_3(SO_4)_2(OH)_6 + 3H_2O \rightarrow 1.245K^+ + 0.01425Fe^{3+} + 2.336FeO(OH) + 2SO_4^{2-} + 2.71H^+ \quad (4.4)$$

Only the concentration of aqueous iron and iron left in residual solids (jarosite plus goethite) was reported by Smith et al (2006), with no distinction between iron in goethite and iron in jarosite. However, given the similarities in steady-state ion concentrations ($K^+$, $SO_4^{2-}$) between acidic and alkaline dissolution, it is assumed that a similar amount of total iron dissolves in alkaline conditions as does in acidic conditions. Therefore, in Equation 4.4, the difference in $Fe^{3+}$ concentration between steady-state acidic dissolution, where no iron precipitation occurs, and steady-state alkaline dissolution can be attributed entirely to goethite precipitation. These calculations will show not only the extent of goethite precipitation but also will provide a measure of mass loss of jarosite as a result of the dissolution process.

The dissolution mechanisms of jarosite discussed in Section 2.6 indicate that higher dissolution is expected at pH 10 than at pH 3.5. Using the alkaline dissolution reaction (Equation 4.4), one can estimate the amount of jarosite dissolved at pH 10 based on the quantity of hydroxide consumed. At the beginning of the experiment, prior to the addition of jarosite, a volume of 8 mL of a 0.01 M $NaNO_3$ solution at pH 10 was added. During conditioning of the jarosite sample, a total of 7 mL of 0.01 M $NaNO_3$ at pH 11 was added in order to maintain pH at 10, as explained in Section 3.2.7. All surfactant solutions were also pre-conditioned to pH 10. At the end of the centrifuging step, after the addition and conditioning of all the components of the adsorption mixture the pH of the colloidal suspensions was 9.9 (+/- 0.1). 7 mL of a background solution with pH 11 contains 0.007 L $\times 10^{-3}$ mol/L of hydroxyl ions, or $7\times10^{-6}$ mol.

Since the final pH changes from 11 to 10 (or pOH increases from 3 to 4) and the final $OH^-$ ion concentration becomes $10^{-4}$ M (or $7\times10^{-7}$ mol in a volume of 7 mL), the amount of hydroxyl ions consumed to maintain the pH at 10 is $7\times10^{-6}$ mol - $7\times10^{-7}$ mol = $6.3\times10^{-6}$ mol. The stoichiometric coefficient of hydroxide consumption in the jarosite dissolution equation (4.4) is 2.71. The stoichiometric coefficient of jarosite is 1. In other words, for every 2.71 moles of hydroxide, 1 mole of jarosite is consumed. This stoichiometry results in a total jarosite dissolution of 2.32 x $10^{-6}$ mol. Multiplying this value by the molar mass of potassium jarosite (500.81 g/mol) results in an estimated 1.16 mg of jarosite dissolution in a volume of 30 mL. A reference estimation of dissolution can be conducted by using the jarosite solubility as analyzed in Section 2.6 for steady-state dissolution tests conducted by Baron and Palmer (1996) [0.0644 g/L at pH 1.6; 0.0816 g/L at pH 3] and Smith et al (2006) [0.0831 g/L at pH 2; 0.0836 at pH 8]. By using the total volume used in this thesis (30 mL), the maximum dissolution of jarosite can be estimated based on the highest reported solubility value [0.0836 mg/L (Smith et al. 2006)] to be 2.51 mg. This literature-based value is significantly larger than a solubility of 1.16 mg calculated in this thesis, but it should be noted that the cited solubility studies relied on equilibration times on the order of months. Therefore, it is reasonable to expect that under the experimental conditions of this research, and the relatively short timescales of the experiments, the solubility of jarosite should be lower (and far from steady-state) than the steady-state values reported in the literature. These calculations lead to the assumption that the mass loss of jarosite as a result of dissolution is negligible (approximately 1.16 mg out of 2 grams, or 0.06%) during conditioning for adsorption and Hallimond tube flotation experiments over the timescale of the tests.

Due to the relationship between iron precipitation and jarosite dissolution, the formation of goethite can also be estimated. Under the experimental conditions, especially in alkaline solutions, it can be expected that practically the entire amount of iron released by jarosite into solution precipitates as a goethite coating. As shown by Smith et al. 2006, at pH 8, only 0.6% of total iron released by jarosite remained in solution, while the remaining 99.4% was in the form of precipitated goethite. An estimation of goethite precipitation based on hydroxide consumption can be completed by using the stoichiometric coefficient for goethite in Equation 4.4 (2.336) and converting the moles of jarosite consumed ($2.32\times10^{-6}$ mol) to moles of goethite precipitated ($2.32\times10^{-6}$ mol jarosite × 2.336 = $5.43\times10^{-6}$ mol) and finally to the mass of goethite

precipitated ($5.43\times10^{-6}$ mol × 88.85 g/mol goethite = 0.48 mg). Previous literature on alkaline jarosite dissolution (Section 2.6), the visual colour change on jarosite as the pH is increased from 8 to 10 to 12 (Figure 4-3), and the zeta potential results conducted for the purpose of this thesis (Figure 4-13 and Figure 4-14), all point to significant surface coverage of jarosite particles by goethite at pH 10. Therefore, the presence of goethite on the jarosite surface cannot be ignored when discussing adsorption mechanisms of surfactants in the following sections.

### 4.5.2 Lauric Acid

Surfactant adsorption and Hallimond tube flotation tests with lauric acid were conducted at initial concentrations of 0-200 mg/L (pH 3.5) and 0-300 mg/L (pH 10). The methods for calculating the pH of precipitation, as well as individual species concentrations, for lauric acid are shown in Section 2.9.1. Calculations of the pH of precipitation in the tested concentration range show that a colloidal precipitate of lauric acid is only present at pH 3.5, and does not form at pH 10. The dominant species at pH 10 is the $RCOO^-$ anion. At pH 3.5 the RCOOH precipitate is the dominant form, with aqueous RCOOH remaining at a constant concentration at the limit of solubility ($1.20\times10^{-5}$ M).

#### 4.5.2.1 pH 3.5

All 5 jarosite samples experience high lauric acid adsorption densities at natural pH (3.5) for initial concentrations of 20, 50, and 80 mg/L, with nearly 100% adsorption. A plateau develops at an adsorption density of 0.02-0.025 mmol/$m^2$ for sodium jarosite samples. Potassium samples continued to adsorb large amounts of lauric acid at 150 mg/L before starting to level off at a higher concentration of 200 mg/L (0.04 mmol/$m^2$). There is no noticeable influence of silver on adsorption. At an initial concentration of 20 mg/L the sodium jarosite samples experienced poor flotation. The two potassium samples gave moderate flotation. All 5 samples perform moderately at initial concentrations of 50 and 80 mg/L before achieving good flotation at the same initial concentration (150 mg/L). The shorter 45 second Hallimond tube flotation test yielded no difference among the 5 jarosite samples, although only a fraction of material was collected compared to the 2 minute test.

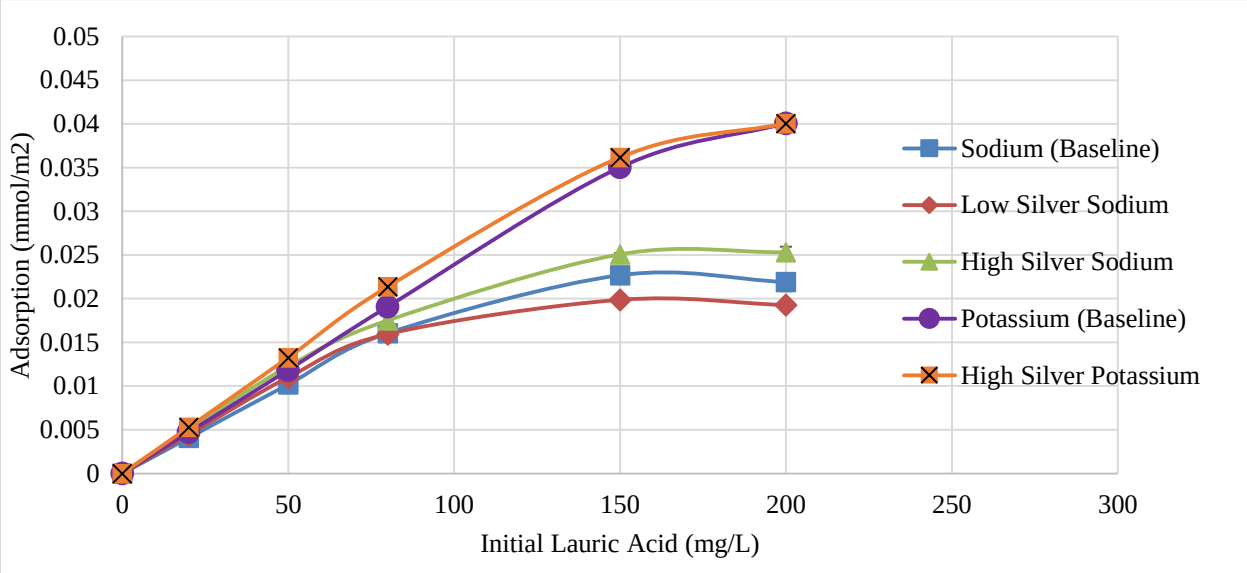


Figure 4-18: Lauric Acid Adsorption Results (pH 3.5).

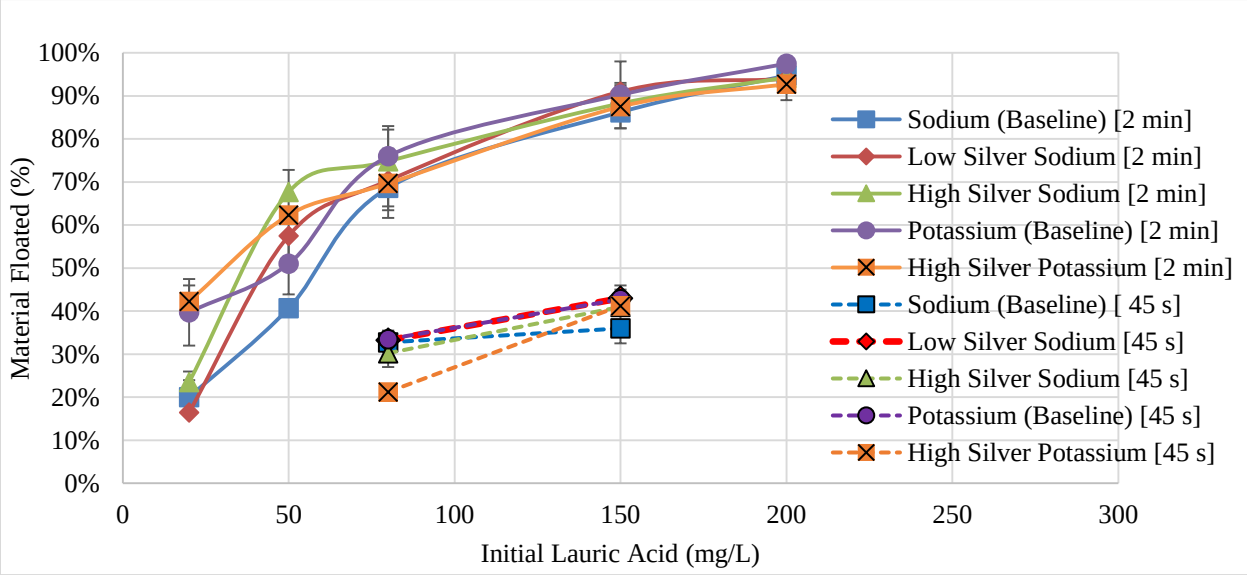


Figure 4-19: Lauric Acid Hallimond Tube Flotation Results (pH 3.5).

At pH 3.5 lauric acid forms a colloidal precipitate rather than a true solution. Attachment of these colloidal particles accounts for the high adsorption densities, and nearly 100% adsorption at concentrations below 100 mg/L. Multiple molecules are adsorbing simultaneously as part of the precipitate particles, as opposed to adsorption of individual molecules, which is the main mode of adsorption from a true surfactant solution. The iep of the lauric acid precipitate is at pH 2.5-3, above which the precipitate is negatively charged (Laskowski, 1999). Therefore at pH 3.5, electrostatic attraction between the surface and the precipitate is most

likely the main interaction mechanism. Potassium jarosite samples exhibit higher adsorption densities at 150 and 200 mg/L. As silver appears to have no significant impact on the results it is presumed that this increased adsorption is due to a higher affinity of the colloidal precipitate for potassium. This higher affinity, however, does not translate to enhanced flotation of the potassium jarosite particles, with sodium samples requiring a lower adsorption density to become sufficiently hydrophobic.

#### 4.5.2.2 pH 10

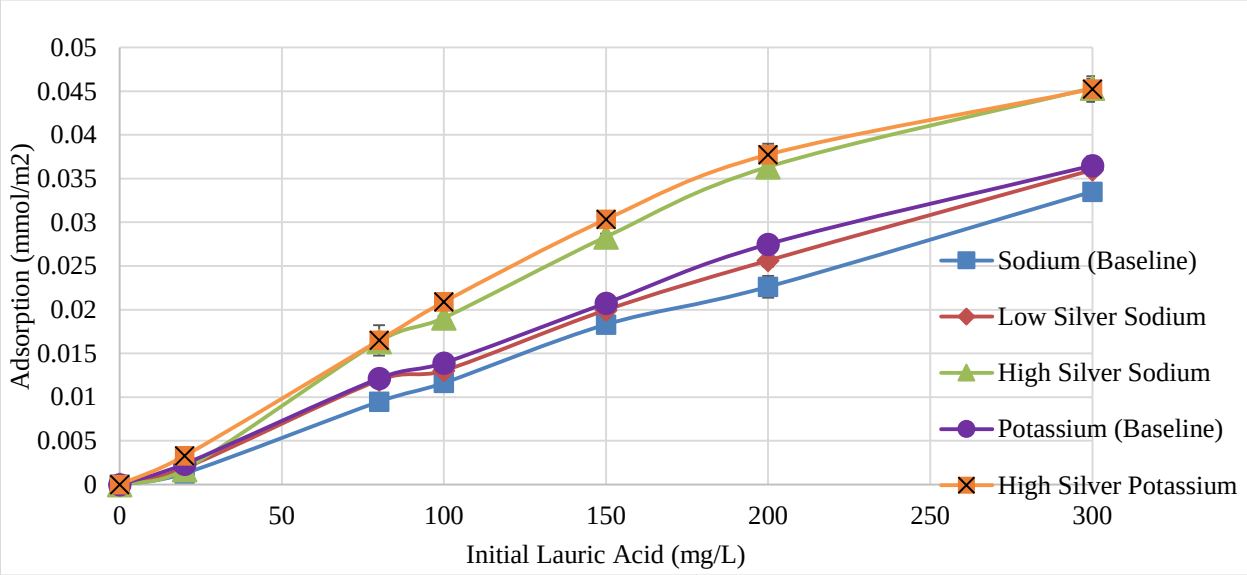


Figure 4-20: Lauric Acid Adsorption Results (pH 10).

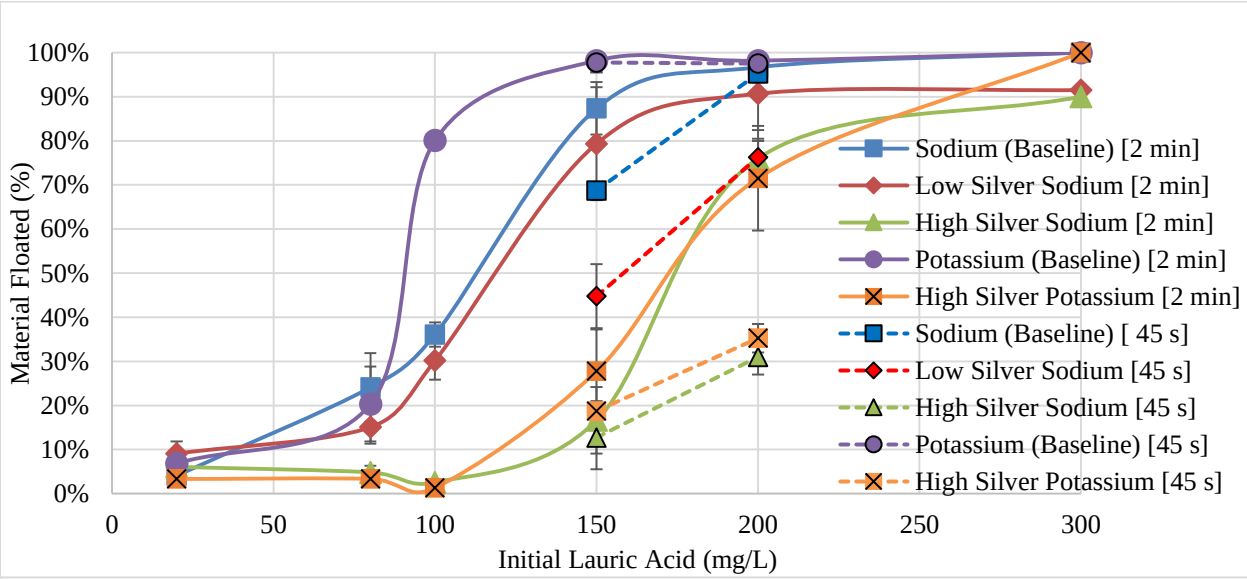


Figure 4-21: Lauric Acid Hallimond Tube Flotation Results (pH 10).

All 5 jarosite samples experienced significant, continuous, nearly linear adsorption of lauric acid at pH 10. The two high silver jarosites displayed slightly higher adsorption than the rest of the samples over the tested concentration range. Hallimond tube experiments at low initial concentrations of 20 and 80 mg/L of lauric acid (pH 10) result in poor flotation for all jarosite samples. Flotation of the two high silver samples remains poor at initial concentrations of 100 and 150 mg/L before achieving moderate/good results at 200/300 mg/L. The low silver and baseline sodium jarosite samples exhibit moderate flotation at 100 mg/L and good flotation at 150, 200, and 300 mg/L. The potassium jarosite sample produces good flotation at even lower initial concentrations of 100 mg/L, with extremely fast flotation of material taking place at higher doses. A change in jarosite colour, from yellow-orange to a darker orange, was observed for all samples at elevated concentrations at pH 10, particularly when moderate/good flotation was achieved.

Shorter 45 second Hallimond tube experiments at 150 mg/L demonstrate the high rate with which baseline samples float, particularly the potassium jarosite, which achieves complete flotation over that time. That result again correlates with the apparent higher affinity of lauric acid for potassium. At 200 mg/L only a fraction of material floats from the high silver samples after 45 sec, compared to the amount floating during the full 2 minute test, whereas baseline samples achieve 100% mass yield. All the samples apparently required a critical dose, or a minimum adsorption density, to achieve moderate/good flotation results, which correlated well with the colour change that was found to occur. This colour change indicates the formation of a surface coating on jarosite particles as a result of surfactant adsorption. The behaviour of the low silver sodium sample is similar to the baseline sodium sample and this result could be attributed to the sodium jarosite rimming present in the low silver sodium sample as shown in the SEM data (Figure 4-9). The surface of low-Ag sodium jarosite appeared to be coated by an Ag-deficient layer.

At pH 10 lauric acid is in the dissociated, anionic form. At these basic conditions a colloidal acid precipitate does not form, so the adsorption and flotation results are controlled by interactions of the jarosite particles with the dissociated laurate anion ($RCOO^-$). The surface of jarosite is also negatively charged, therefore electrostatic attraction cannot be a dominant mechanism of interaction. No literature was found on adsorption mechanisms of sodium laurate

on jarosites. However, the more readily available work surrounding the adsorption mechanisms of surfactants on hematite ($Fe_2O_3$) was examined. This approach is appropriate because the surface of jarosite is presumed to be coated with goethite (FeO(OH)) at pH 10 and should have similar surface characteristics to that of the hydrated hematite modelled by Chernyshova et al (2011).

Peck et al (1966) were the first authors to present evidence of chemical adsorption between a long chain carboxylic acid (oleic acid, C18) and the hematite surface to form a ferric carboxylate species. Han et al (1973) reported lauric acid (C12) adsorption on hematite (above the pzc) to proceed through chemical adsorption as well as via hydrogen bonding. Quast (2000) demonstrated chemical adsorption of lauric acid on hematite at pH 10, when the surface of hematite was negatively charged. The same mechanisms of lauric acid adsorption on hematite were reported by Chernyshova et al (2011). Adsorption at low concentrations occurred chemically via a single bonded oxygen to surface iron along with a hydrogen bond between the double bonded oxygen atom and a surface hydroxyl group. This mechanism of adsorption was found to be dominant at low lauric acid concentrations (Ponnurangam et al, 2012). As the concentration of lauric acid increases, the chemically bonded laurate anion acts as an anchor point for further laurate adsorption. Intermolecular (lateral) hydrogen bonding and hydrophobic interactions between this anchoring molecule and adjacent laurate anions help to overcome the increasing electrostatic repulsion between more and more densely adsorbing laurate anions. This enables two hydrogen bonds to form between the two oxygen atoms of lauric acid and the hydroxylated (-OH) sites on the hematite surface. As the concentration of lauric acid increases, the domains of adsorbed molecules grow (Figure 4-22) through increased double-hydrogen bonding (Chernyshova et al, 2011). The hydrogen bonded molecules have more freedom to rearrange and obtain better packing than the chemically bonded molecules (Ponnurangam et al, 2012).

Although the adsorption density nearly linearly increases with laurate concentration, it is clear that adsorption at lower surfactant concentrations is insufficient to induce good flotation. It therefore appears that the initial chemical adsorption of the anchoring laurate molecules does not render the surface sufficiently hydrophobic. Only when hydrogen bonded laurate molecules

increase the adsorption density, does the hydrophobicity of the surface increase and flotation is suddenly improved.

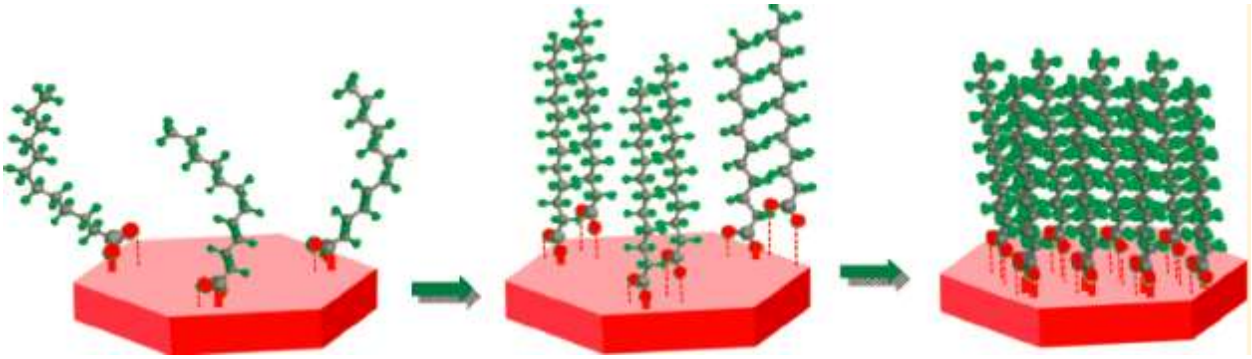

Figure 4-22: Hematite Adsorption of Lauric Acid (pH 10). Chemically Bonded Anchor Molecules (Left). Hydrogen Bonded Molecules Forming Domains Around Anchors (Centre). Monolayer Formation and Particle Hydrophobicity is Achieved as Domains Grow and Connect (Right) (© Chernyshova et al, 2011, by permission).

A change in the adsorption mechanism with increasing surfactant concentrations is further supported by the observed color change at higher laurate concentrations. It should be noted that since the pH was kept constant, this color change is most likely a result of mineral-surfactant interactions.

Based on the substantial adsorption density at pH 10 (despite the conditions for electrostatic repulsion) and the observed colour change experienced by jarosite at higher dosages (suggesting a second mechanism of adsorption), it is concluded that the laurate anion adsorbs on the negatively charged goethite-coated jarosite surfaces (pH 10) through a combination of mechanisms, as suggested by Chernyshova et al (2011) and Ponnurangam et al (2012). The chemical adsorption of laurate ions alone does not offer sufficient hydrophobicity for successful flotation, and the laurate concentration must be increased until sufficient coverage via hydrogen bonding takes place. The two high silver samples give higher laurate adsorption densities than the remaining three samples, but at the same time, the high-silver samples require higher laurate concentrations compared to the other samples in order to achieve high flotation yields. The presence of silver appears to enhance laurate adsorption at pH 10, reinforcing the idea of chemical interactions between the surfactant and the metal sites (Fe and Ag) on the surface, but the orientation of the chemically adsorbed molecules does not favor jarosite flotation. As noted earlier, the chemically-bonded laurate anions are believed to act as anchoring sites for further laurate adsorption through hydrogen bonding. As argued by Ponnurangam et al

(2012), the adsorbed molecules require a level of freedom for self-assembling into a hydrophobic layer. The chemically adsorbed molecules are rigidly bonded with the surface thus preventing the formation of a sufficiently hydrophobic surface layer. The wider concentration range of poor flotation for the high-silver jarosites indicates that laurate chemically adsorbs in that range. Since silver replaces sodium and potassium in the jarosite crystal, those higher levels of silver produce additional sites for the chemical adsorption of laurate, and this effect can be seen in the adsorption densities in Figure 4-21. In the absence of silver, the transition from chemical adsorption to adsorption through hydrogen bonding occurs at lower laurate concentrations, and therefore flotation becomes better at a lower laurate dosage than in the case of high-silver samples.

### 4.5.3 Sodium Dodecyl Sulfate

Surfactant adsorption and Hallimond tube flotation tests with sodium dodecyl sulfate were conducted at initial concentrations of 0-150 mg/L (pH 3.5) and 0-300 mg/L (pH 10).

#### 4.5.3.1 pH 3.5

All 5 jarosite samples are characterized by very low adsorption densities of dodecyl sulfate. The samples gave insignificant differences in the adsorption results between one another. However, flotation with dodecyl sulfate at pH 3.5 yielded unexpectedly much better results than the low adsorption densities would perhaps suggest. When an initial concentration of 100 mg/L was introduced the two high-silver jarosite samples achieved good flotation results, while the 2 baseline samples along with the low silver sodium jarosite remained at moderate levels. At an initial concentration of 150 mg/L all samples floated very well. Although observable only in a narrow concentration range, this increased flotation of the high-silver samples seems to suggest that the silver sites on the jarosite surfaces enhance the surfactant-jarosite interactions. At the same time, there are no indications in the flotation or adsorption results of a change in the adsorption mechanism, by analogy to the effect of silver on laurate-jarosite interactions discussed earlier.

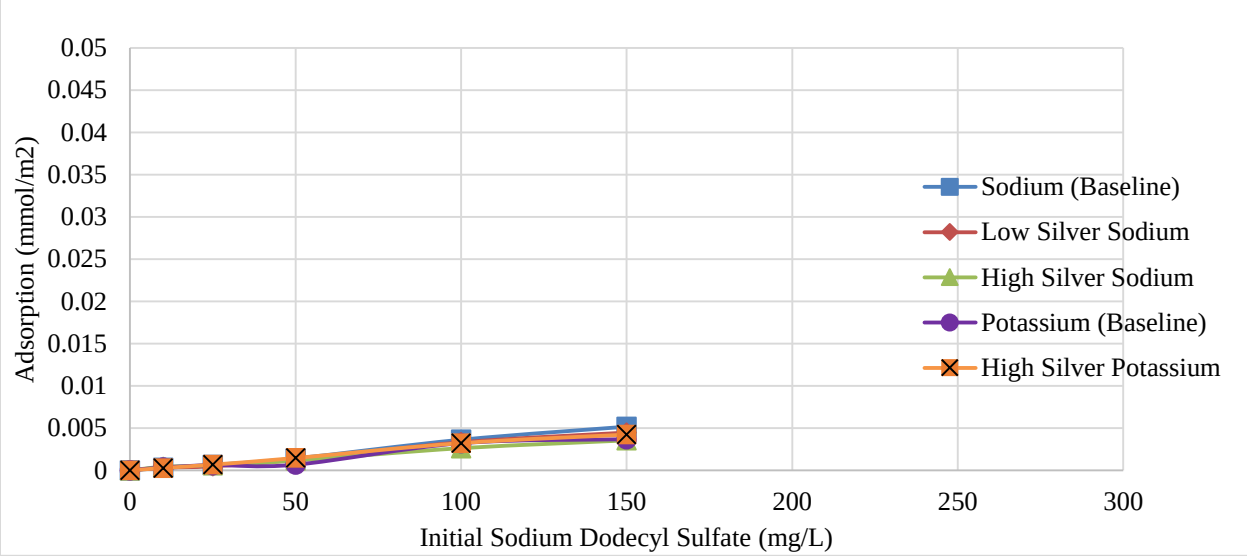


Figure 4-23: Sodium Dodecyl Sulfate Adsorption Results (pH 3.5).

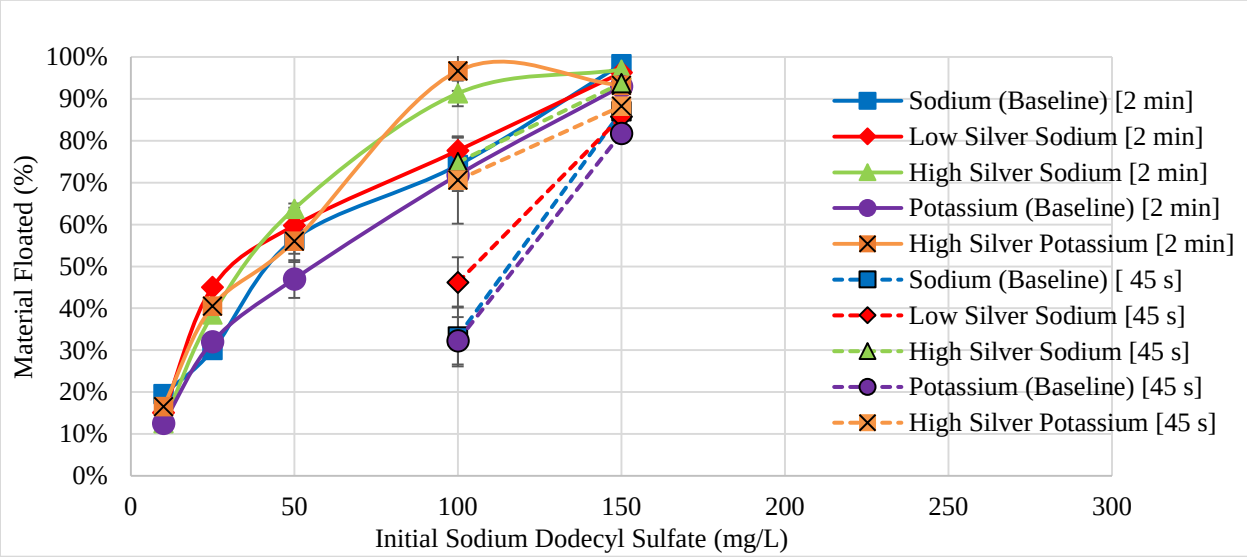


Figure 4-24: Sodium Dodecyl Sulfate Hallimond Tube Flotation and Reagent Adsorption (pH 3.5).

Shorter 45-second Hallimond tube experiments were conducted at initial concentrations of 100 and 150 mg/L. This revealed that the high silver samples floated much faster at 100 mg/L. High silver bearing jarosite samples achieved mass yields of 70%, compared to approximately 30-50% achieved by the baseline/low silver samples during the 45 second test. The flotation kinetics (100 mg/L) are faster when silver is present on the surface.

At pH 3.5 the surface of jarosite is positively charged. Dodecyl sulfate is fully dissociated and negatively charged. The strong attraction that will exist between the two opposite charges leads to the simple conclusion that adsorption of dodecyl sulfate on the surface

of jarosite at pH 3.5 is physical and due to attractive electrostatic forces. The reason behind such low adsorption densities producing good flotation results is unclear, and the low adsorption density is rather inconsistent with adsorption by electrostatic attraction, as numerous studies show for other surfactant-mineral systems.

When reviewing the adsorption mechanisms of the tested surfactants on oxide surfaces, it should be noted that numerous studies identify chemical adsorption between laurate anion (and also hydroxamate) and iron sites as the mechanism of interaction. At the same time, sodium dodecyl sulfate does not adsorb on the goethite-coated jarosite at pH 10, and a very low adsorption density was observed at low pH. This comparison suggests that the low adsorption of dodecyl sulfate does not proceed onto the iron sites. The assumption behind using dodecyl sulfate was that it would show a high affinity towards jarosite surfaces because of the common sulfate anion. Using equilibrium solubility data from the literature (data from Smith et al, 2006, in Table 2-5), it is possible to estimate the adsorption density of dodecyl sulfate assuming indeed that adsorption proceeds onto the vacant sites left after dissolution of sulfate ions from the jarosite surface. According to Smith et al (2006), the concentration of sulfate anions in equilibrium with jarosite is $3.3 \times 10^{-4}$ mol/L. Since the volume of solution used in the adsorption in this research was 30 mL, the number of moles of sulfate in that volume was $3.3 \times 10^{-4}$ mol/L × 0.03L = 0.00001 mol, or 0.01 mmol. Since all the jarosite samples had very similar BET specific surface areas, an average value of $0.3122 \pm 0.03$ $m^2/g$ can be assumed in further calculations. Since 2 grams of jarosite were used in each adsorption test, the surface area available for adsorption under the experimental conditions can be calculated as $0.3122$ $m^2/g \times 2g = 0.6244$ $m^2$. Using the number of moles of sulfate ions in solution (0.01 mmol), along with the surface area ($0.6244$ $m^2$), the number of adsorption sites available for dodecyl sulfate adsorption, or essentially the maximum adsorption density, can finally be calculated as 0.01 mmol/$0.6244$ $m^2$ = $0.016$ mmol/$m^2$. This value immediately shows that the maximum adsorption density of dodecyl sulfate on the jarosite surface, assuming ion exchange between sulfate and dodecyl sulfate, is very low compared to the adsorption densities measured for the other surfactants. This observation suggests that adsorption of dodecyl sulfate indeed proceeds onto the vacant sites left after sulfate anions, and that adsorption on these sites should be very low. This calculated value can be refined further by noting that the equilibrium sulfate concentration (from Smith et al, 2006) used in this calculation was obtained after 4 months of equilibration, while the timescale

of our tests was much shorter. The solubility of jarosites calculated for the experimental conditions of this research (Section 4.5.1) was 1.16 mg, while the value calculated from steady-state ion concentrations (Smith et al, 2006) was 2.51 mg. In other words the concentration of sulfate in solution under the experimental conditions should be actually lower, which in turns implies that the number sites, and the adsorption density, should be even lower than 0.016 mmol/$m^2$. Using the ratio of the solubility value from Smith et al (2006) (2.51 mg) to the solubility estimated in this thesis (1.16 mg), the adsorption density of sodium dodecyl sulfate should only be 0.016 mmol/$m^2$/(2.51/1.16) = 0.0074 mmol/$m^2$, which is nearly equal to the highest measured adsorption density of this surfactant (Figure 4-23). This analysis strongly supports the assumption that adsorption of dodecyl sulfate takes place as an exchange process between sulfate ions from the jarosite surface and the dodecyl sulfate anions from solution.

However, this analysis still doesn't explain why such low adsorption densities are able to provide good flotation. Digre and Sandvik (1968) argued that adsorption of a collector at the mineral-liquid interface is not the only mode of collector-mineral interactions, and that substantial amounts of collector molecules can be brought onto the mineral surface by gas bubbles. In this scenario, collector molecules adsorb not only on the mineral surface but also on gas bubbles, and additional collector molecules can be transferred to the mineral surface by collisions with the collector-coated gas bubbles. There is some experimental evidence in support of this model (Pope & Sutton, 1972; Fuerstenau, 2001), but generally such dynamic adsorption phenomena involving three interfaces are very difficult to follow experimentally (Yan, 2016). It is noteworthy that the critical micelle concentration (cmc) of sodium dodecyl sulfate is $8.2 \times 10^{-3}$ mol/L (Leja, 1982) while the critical micelle concentration of sodium laurate is $2.6 \times 10^{-2}$ mol/L (Leja, 1982). These values indicate that the adsorption of sodium dodecyl sulfate on gas bubbles should be higher than the adsorption of sodium laurate at a given molar concentration in solution. Considering that octanohydroxamic acid is a shorter chain surfactant compared to dodecyl sulfate or laurate, the cmc value for hydroxamate should be even higher (no systematic literature data for octanohydroxamic acid were indentified), indicating lower adsorption on bubble surfaces. In other words, sodium dodecyl sulfate is the most likely surfactant of the three tested reagents to undergo the type of surfactant transfer phenomena proposed by Digre and Sandvik (1968) since the adsorption of dodecyl sulfate on gas bubbles should be the highest among the tested collectors.

4.5.3.2 pH 10

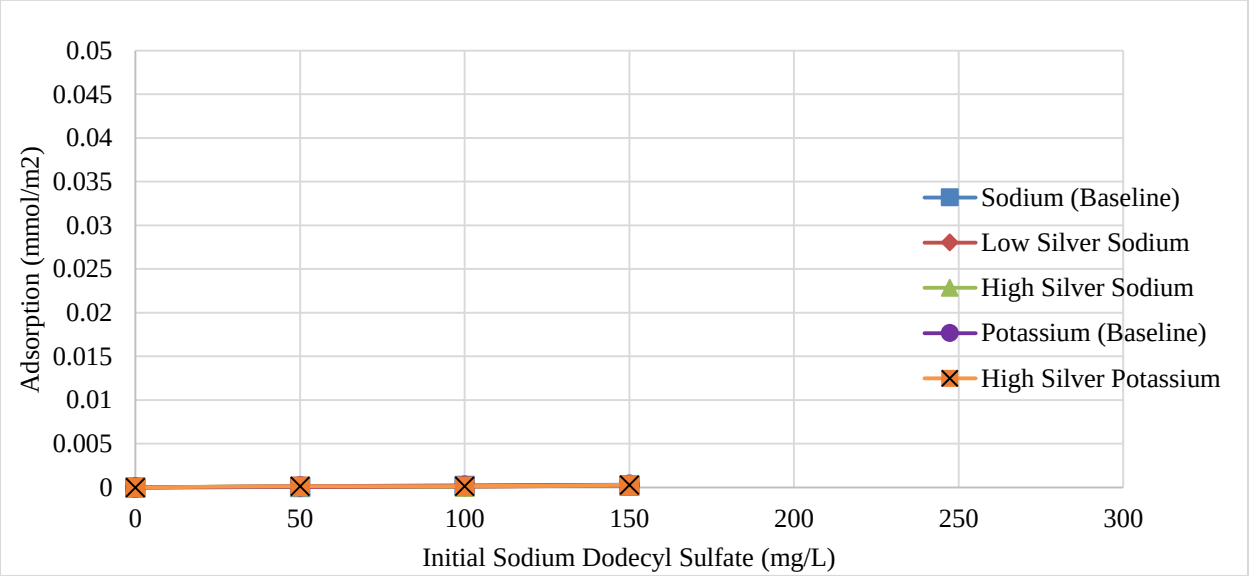


Figure 4-25: Sodium Dodecyl Sulfate Adsorption Results (pH 10).

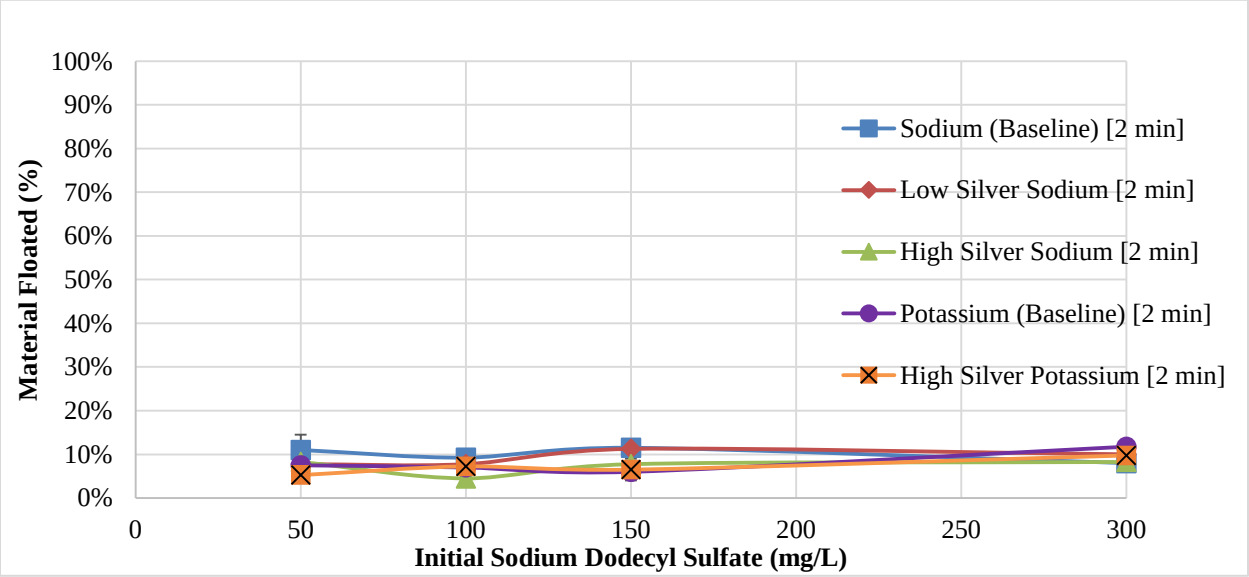


Figure 4-26: Sodium Dodecyl Sulfate Hallimond Tube Flotation Results (pH 10).

Practically no measurable adsorption of dodecyl sulfate at pH 10 was detected. Hallimond tube flotation yielded very poor flotation results for all samples at all tested initial reagent concentrations. Particle/bubble attachment was not visible and flotation cells remained highly turbid at the end of each flotation test. The small amounts of solids, on the order of 10%, collected in each test were most likely a result of mechanical carry-over to the side arm of the Hallimond tube. At pH 10, the surface of jarosite is coated with a goethite layer, and the

flotation of goethite (and other oxide-type minerals) at high pH with dodecyl sulfate is actually known to be very poor (Iwasaki et al, 1960). Such results are normally interpreted in terms of the lack of collector adsorption due to electrostatic repulsion between the negatively charged oxide surface and the anionic collector molecules. In a sense, the formation of goethite on the jarosite surface depresses the flotation of jarosite with dodecyl sulfate.

### 4.5.4 Octanohydroxamic Acid

Hallimond tube flotation tests with the use of octanohydroxamic acid were conducted at initial concentrations of 0-300 mg/L (pH 3.5) and 0-150 mg/L (pH 10).

#### 4.5.4.1 pH 3.5

All 5 jarosite samples showed significant adsorption of octanohydroxamic acid at an unmodified pH (3.5). Sodium jarosites showed slightly lower adsorption densities when silver was present in the crystal structure. However, silver had no impact on octanohydroxamate adsorption on potassium jarosite.

Hallimond tube flotation tests with octanohydroxamic acid at an unadjusted pH (3.5) yielded similar results across all samples, with no apparent effects of sodium/potassium or silver inclusion. Flotation was poor at initial concentrations lower than 150 mg/L. The majority of floated material was due to entrainment from the natural up-flow in the cell. Initial concentrations of octanohydroxamic acid of 200 mg/L led to improved flotation results. There was a decrease in turbidity, and an increase in attachment. It was not until a 300 mg/L initial concentration of hydroxamate that flotation was excellent with practically all the material floating. At this initial concentration the surfaces of jarosite particles appeared to slightly darken in colour.

At pH 3.5 octanohydroxamic acid is un-dissociated and carries no overall charge. Therefore the contributions of electrostatic adsorption are expected to be minimal. Since the presence of silver had no impact on adsorption and flotation results, it is postulated that the adsorption of hydroxamic acid proceeds primarily on iron sites on the jarosite surfaces. It

should also be recalled that the content of iron was practically the same for all the jarosite samples, which should produce very similar surface densities of the adsorption sites.

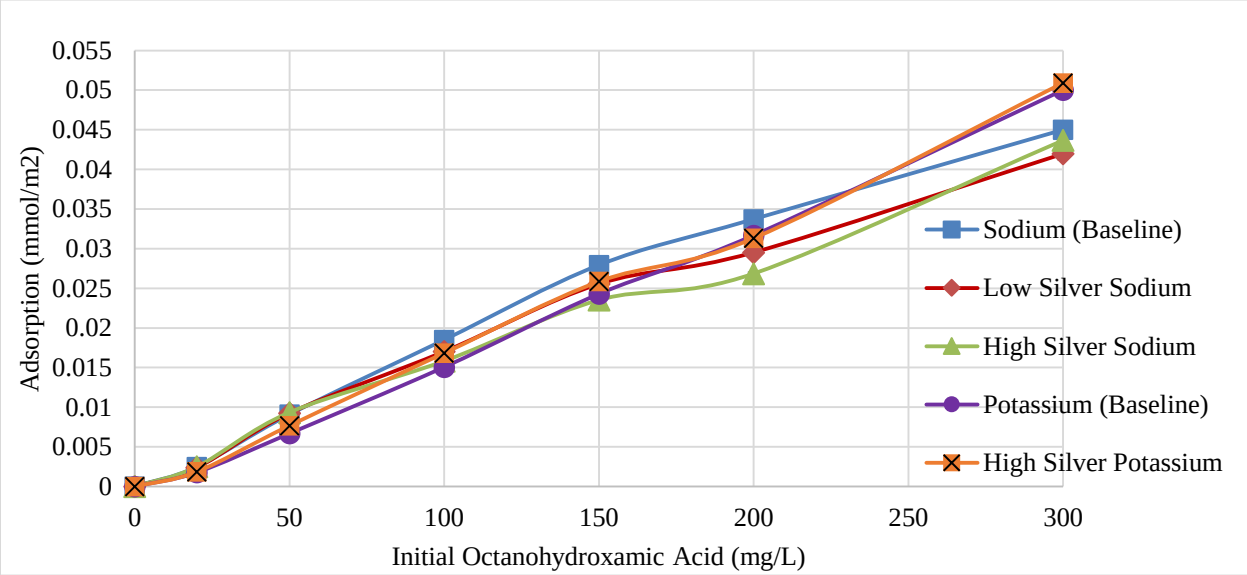


Figure 4-27: Octanohydroxamic Acid Adsorption Results (pH 3.5).

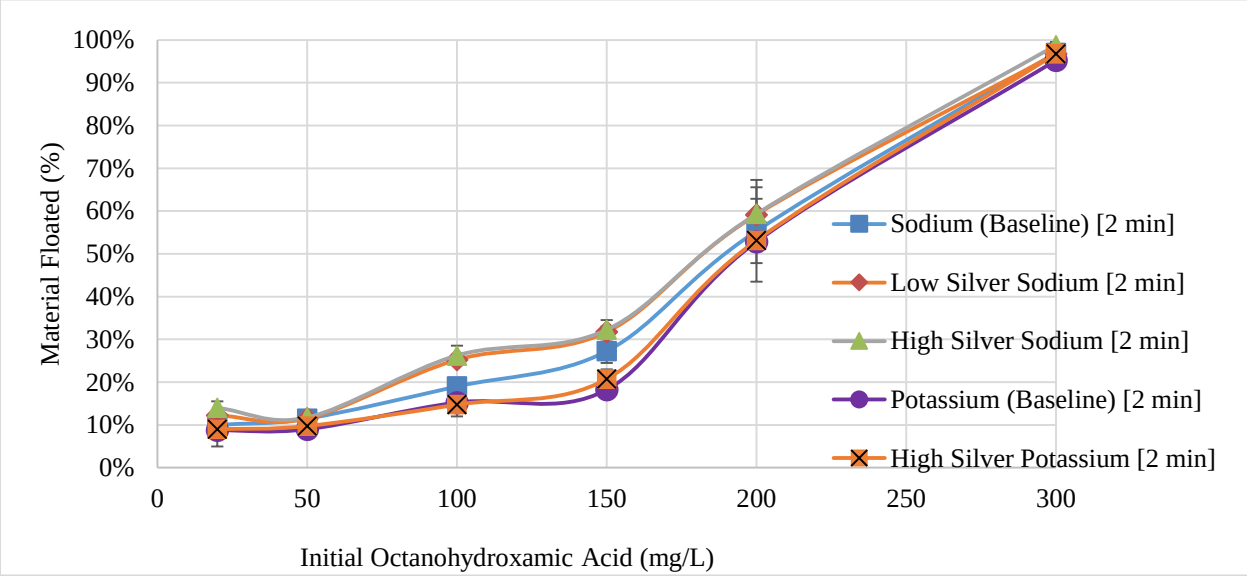


Figure 4-28: Octanohydroxamic Acid Hallimond Tube Flotation Results (pH 3.5).

Similarly to lauric acid, there are no literature data on the adsorption mechanisms of hydroxamates on the surface of jarosite, therefore previous work surrounding their adsorption on goethite was examined. Goethite was selected due to both minerals having similar structures, with a centrally located iron atom bonded to surrounding oxygen atoms. Even though jarosites are not coated by goethite at pH 3.5, jarosites contain hydroxyl groups in their crystal structure,

and it is fair to assume that jarosite surfaces will also contain iron-hydroxyl sites, similarly to the surfaces of oxide minerals.

Holmen et al (1997) observed that acetohydroxamate ($CH_5NO_2$) adsorption took place on goethite (pH 3-6) initially via a chemical bond between a hydroxamate oxygen atom and a surface iron site, and a hydrogen bond between two hydroxyl groups – one from the mineral surface and one from the hydroxamate molecule (Figure 4-29). It should be noted that in the pH range from 3 to 6 hydroxamic acid R-CONH-OH is the dominant species in solution. Through a complex process of rearrangement and dehydration (Figure 4-30), the hydroxamic acid eventually forms a bidentate ligand, with a second oxygen atom from the hydroxamate now being bonded to the central iron atom from the mineral surface (Figure 4-31). The rate of the overall process shown in Figure 4-30 is directly proportional to the total adsorbed hydroxamate on the goethite surface – chelation proceeds faster at higher adsorption densities of hydroxamate. These experiments were conducted at concentrations of $10^{-3}$ M of hydroxamate, which was just above the molar concentration at which jarosite flotation began to show improved results (150 mg/L of octanohydroxamic acid is equal to a concentration of $9.4\times10^{-4}$ mol/L). It is postulated that at concentrations lower than 200 mg/L, insufficient amounts of octanohydroxamate adsorbed on the surface of jarosite to promote the process of chelation. In order to induce successful flotation, a critical concentration of octanohydroxamate is required, as seen in the flotation results. This change in the flotation response seems to follow the two modes of hydroxamic acid adsorption on iron sites. The single chemical bond shown in Figure 4-29 is unable to make jarosite sufficiently hydrophobic for flotation. The change in colour that was observed around a concentration of 200 mg/L reinforces the suggestion that a new adsorption mechanism started to take place at higher hydroxamate concentrations creating a hydrophobic surface. The orientation of the resulting surfactant-iron bidentate ligand at the goethite surface appears to promote flotation. The transition concentration from one adsorption mechanism to the other appears to coincide with the transition from poor to good flotation. The removal of water molecules from the interface during the dehydration step should also contribute to increased hydrophobicity.

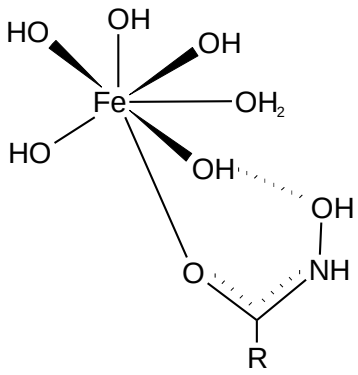


Figure 4-29: Initial Adsorption of Acetohydroxamate on Goethite. Chemical Fe-O Bond and Hydrogen Bond between Surface and Reagent Hydroxyl Groups (© Holmen et al, 1997, by permission).

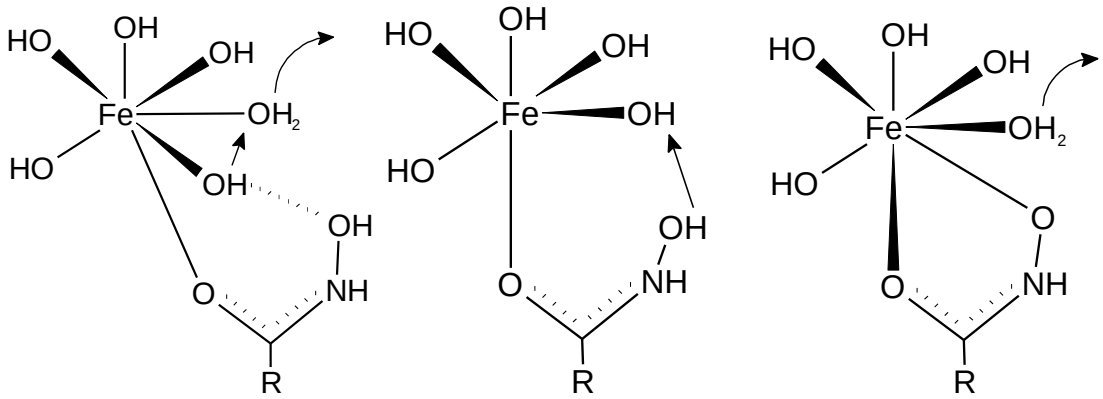


Figure 4-30: Dehydration and Shifting of a Hydroxyl Group and Hydrogen Atom to Surface Iron during Acetohydroxamate Adsorption on Goethite (© Holmen et al, 1997, by permission).

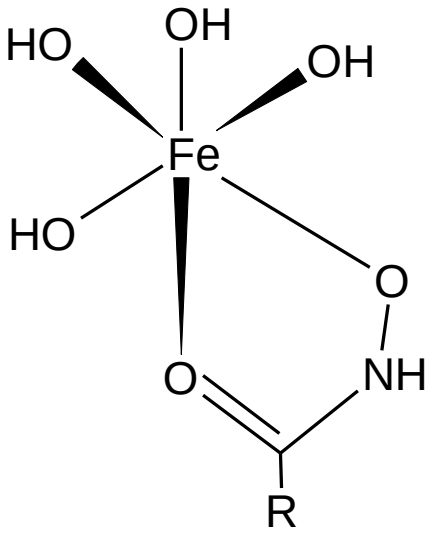


Figure 4-31: Bidentate Ligand (Chelation) Formed between Acetohydroxamate and Goethite (© Holmen et al, 1997, by permission).

4.5.4.2 pH 10

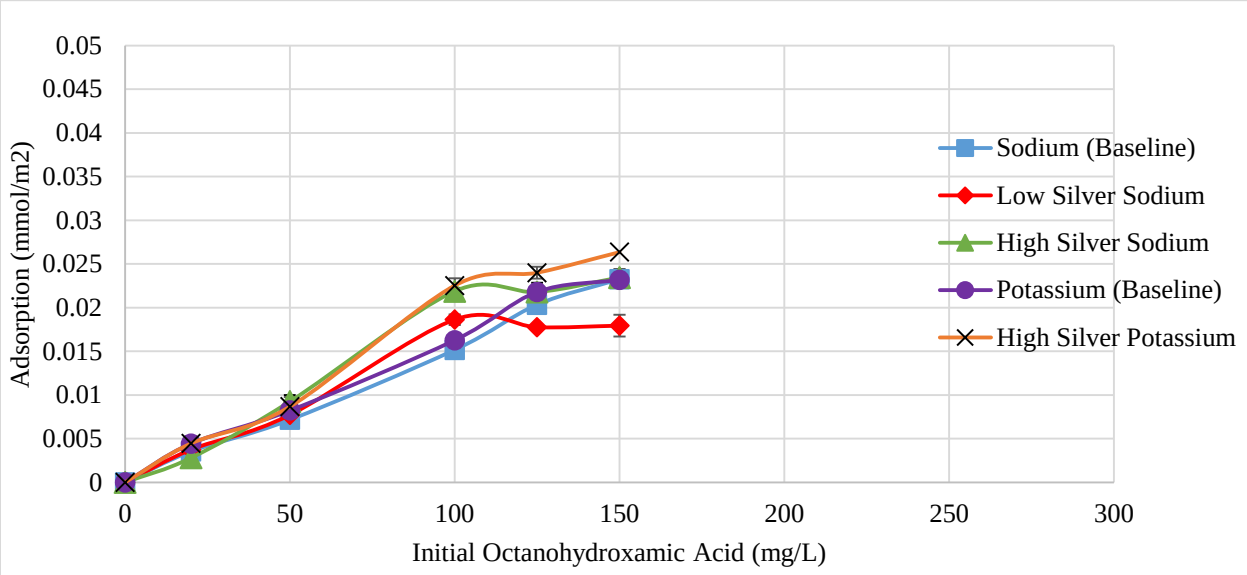


Figure 4-32: Octanohydroxamic Acid Adsorption Results (pH 10).

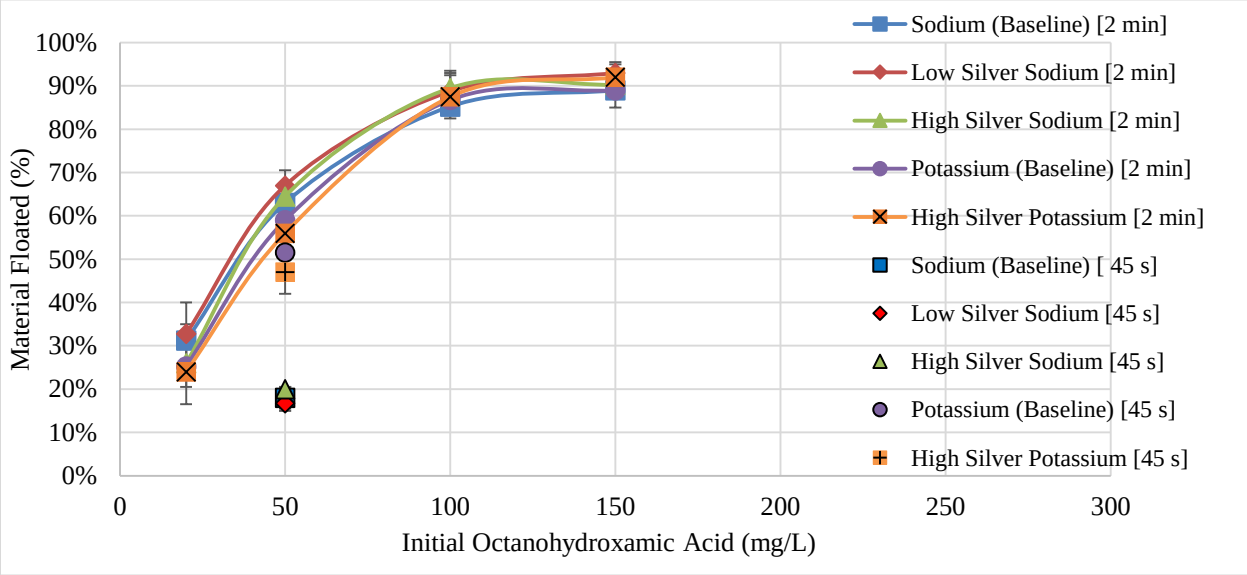


Figure 4-33: Octanohydroxamic Acid Hallimond Tube Flotation Results (pH 10).

All jarosite samples produced very similar adsorption densities of octanohydroxamate at pH 10. Adsorption densities reach a plateau at initial concentrations between 100-125 mg/L (0.005-0.008 mmol/$m^2$). This plateau region closely corresponds with the concentration range of highest flotation. A visible colour change occurred in all samples when high initial concentrations (>100 mg/L) were used. Jarosite particles changed from yellow-orange to a dark orange.

Shorter 45 second Hallimond tube flotation tests were conducted at pH 10 at an initial concentration of 50 mg/L. Nearly identical amounts (~50%) of potassium jarosites were floated during the 45 second tests, which was almost the same as in the 2 minute tests, whereas very little of the sodium samples (~20%) floated in 45 seconds when compared to the full 2 minutes. These results indicate that the presence of potassium over sodium on the jarosite surface increases the flotation kinetics when conditioned with octanohydroxamate at pH 10, without substantial differences in the adsorption densities.

At pH 10 octanohydroxamic acid is dissociated, with the hydroxamate anion R-CONH-$O^-$ being the dominant species adsorbing on goethite. In the hydroxamate anion, and in contrast to the acid form R-CONH-OH, the second oxygen atom is now freed for direct metal chelation to occur. This appears to be the major difference from octanohydroxamic acid adsorption at pH 3.5, as the formation of the bidentate ligand (Figure 4-31) can directly proceed without the intermediate stages shown in Figure 4-30. This mode of interaction explains why the similar adsorption densities between pH 3.5 and 10 at low concentrations of octanohydroxamic acid result in such a difference in flotation results,

At pH 10, the surface of jarosite is negatively charged. Adsorption proceeds despite the electrostatic repulsion existing between jarosite and the hydroxamate anions. Such a behavior is often an indication of chemical interactions between the surfactant and the mineral surface. At pH 10, jarosite surfaces are coated by goethite and should resemble the behavior of oxide surfaces even more closely than at pH 3.5.

Buckley and Parker (2013) investigated octanohydroxamate and its ability to adsorb on the surface of iron oxides [hematite ($Fe_2O_3$), and magnetite ($Fe_3O_4$)] and iron sulfides [pyrrhotite ($Fe_{1-x}S$), and pyrite ($FeS_2$)]. Buckley and Parker (2013) discovered that the principle mechanism of adsorption was chemisorption via the formation of a bidentate ligand between the two oxygen atoms in the head group of hydroxamate and iron at the minerals surface (Figure 4-34) confirming essentially the mechanisms proposed by Holmen et al. (1997) at lower pH.

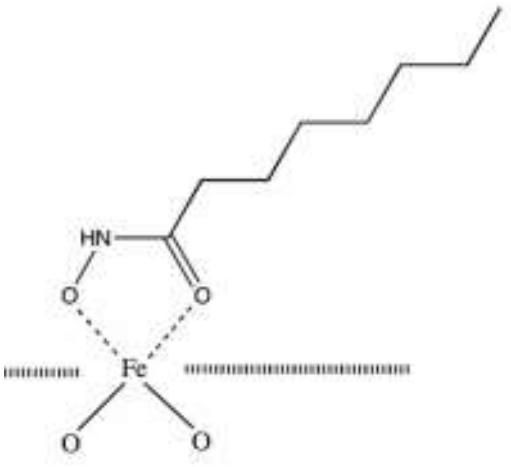


Figure 4-34: Chemical Chelation of Octanohydroxamate on Iron Oxide. Bidentate Ligand Forms at Low Hydroxamate Concentrations. (© Buckley and Parker, 2013, by pemission).

Due to the assumed goethite precipitation it is assumed that adsorption on goethite-coated jarosite particles proceeds along very similar mechanisms. Due to the strong affinity of hydroxamate to form stable chelates with iron (Buckley & Parker, 2013), it is reasonable to expect that adsorption on jarosite, an iron containing mineral, also takes place on iron sites. M-site occupancy of jarosite minerals by monovalent cations should have no impact on chelation between iron and hydroxamate. This assumption is reflected in the adsorption results, where Ag, K, or Na M-site occupation does not seem to have a significant effect on the adsorption density.

### 4.5.5 Individual Jarosite Samples

In the following section, the Hallimond tube flotation (full 2 minute tests) and surfactant adsorption results discussed in Sections 4.5.2, 4.5.3, and 4.5.4 are summarized separately for individual jarosite samples (sodium (baseline) – Figure 4-35; low-silver sodium – Figure 4-36; high-silver sodium – Figure 4-37; potassium (baseline) – Figure 4-38; high-silver potassium – Figure 4-39) in order to highlight the action of the reagents towards the different jarosite samples. Error bars for both adsorption and flotation results are included for duplicated tests. In most cases the adsorption error bars are smaller than the size of the symbol used. Additional adsorption results are also presented as a function of residual surfactant concentration, and given in the appendix.

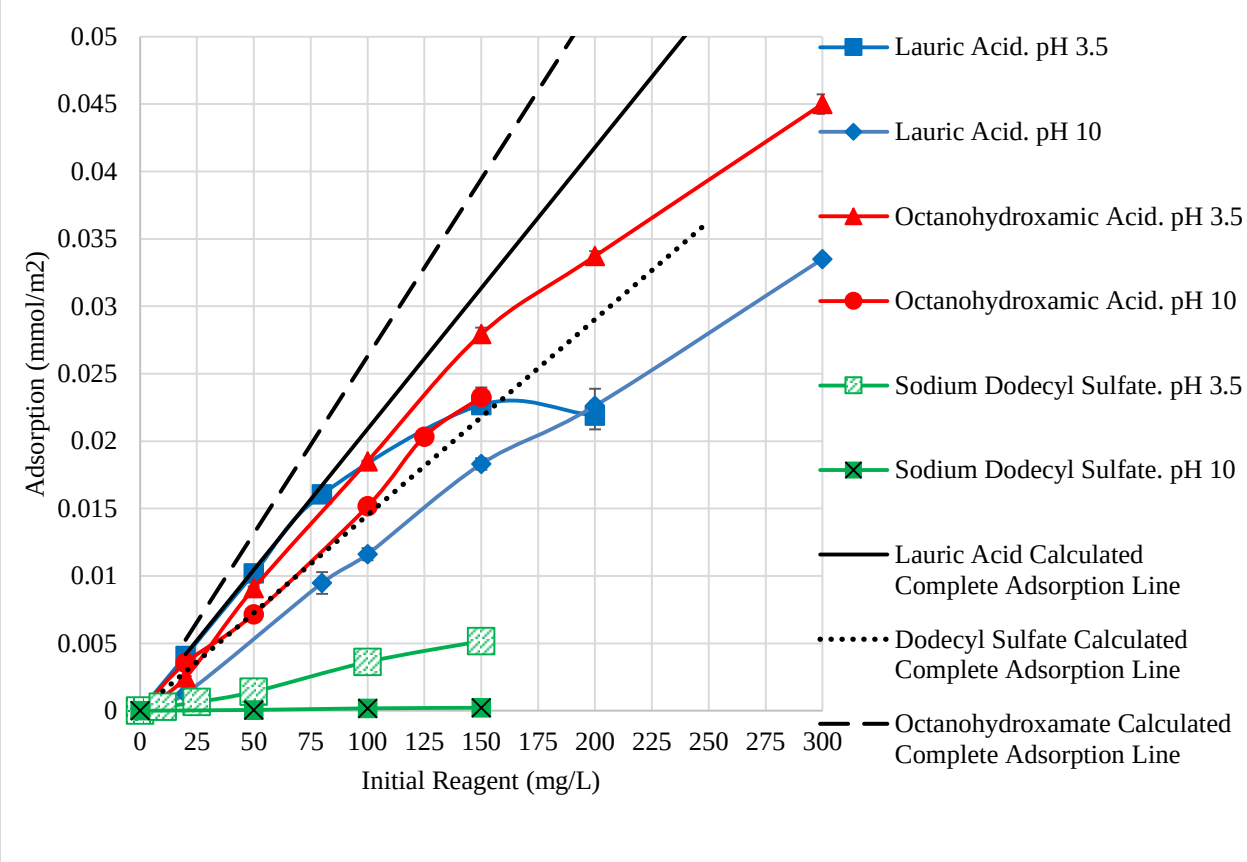


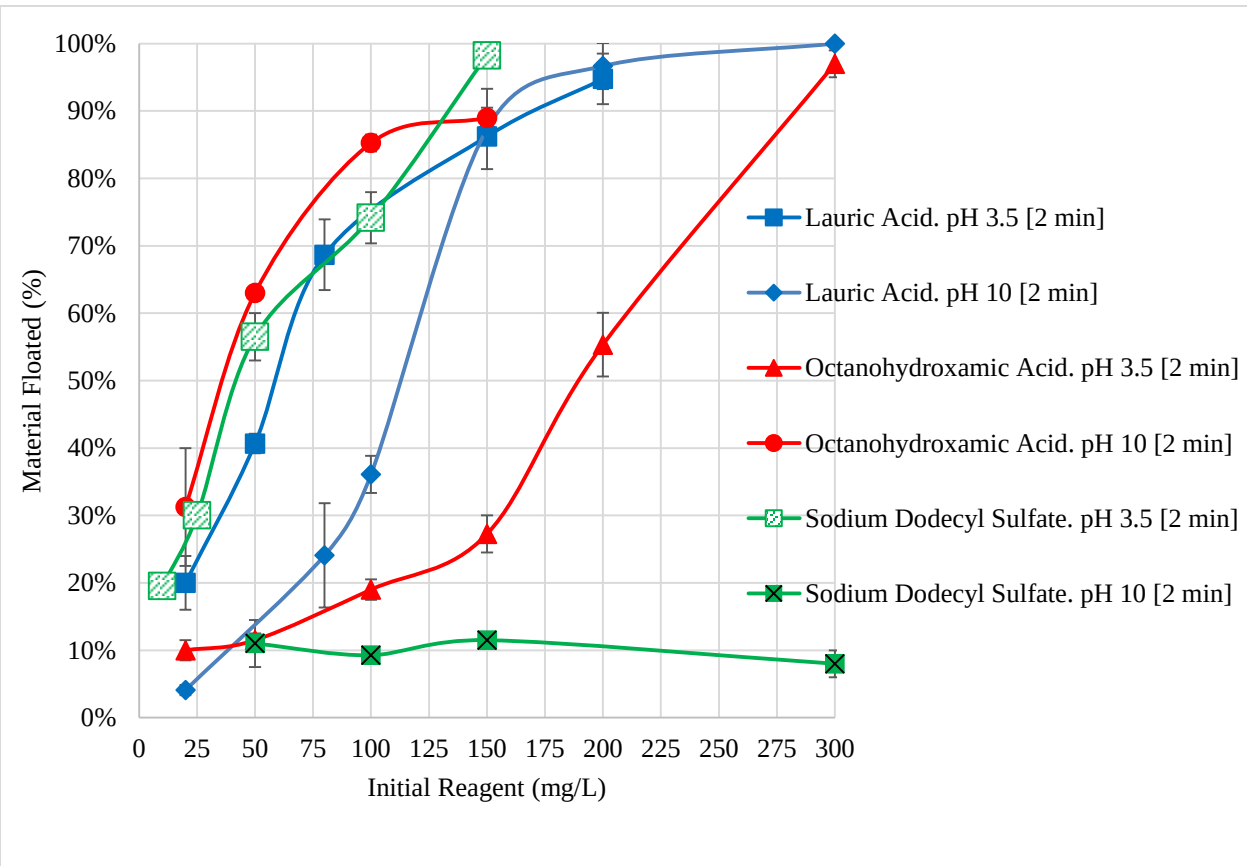


Figure 4-35: Surfactant Adsorption and Hallimond Tube Flotation Results for Sodium Jarosite (Baseline).

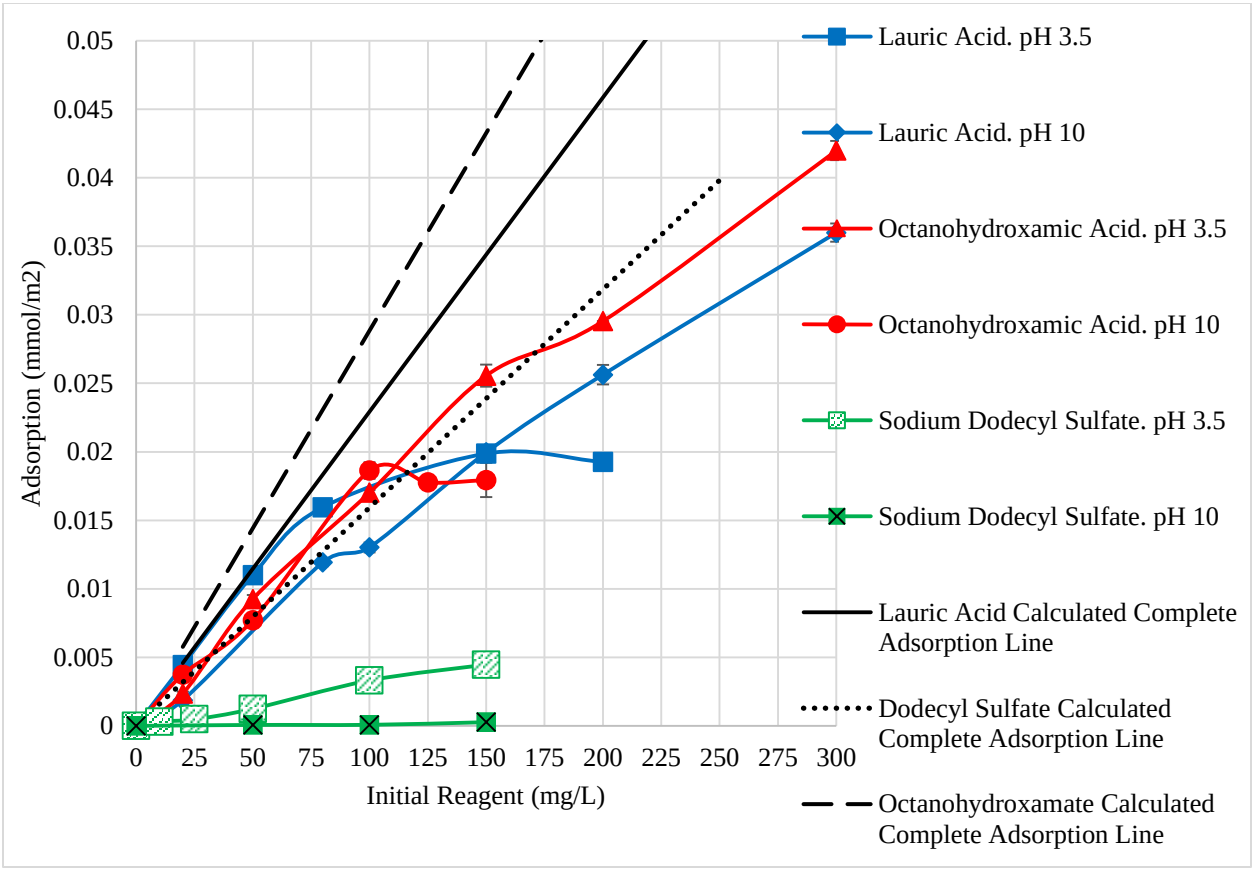


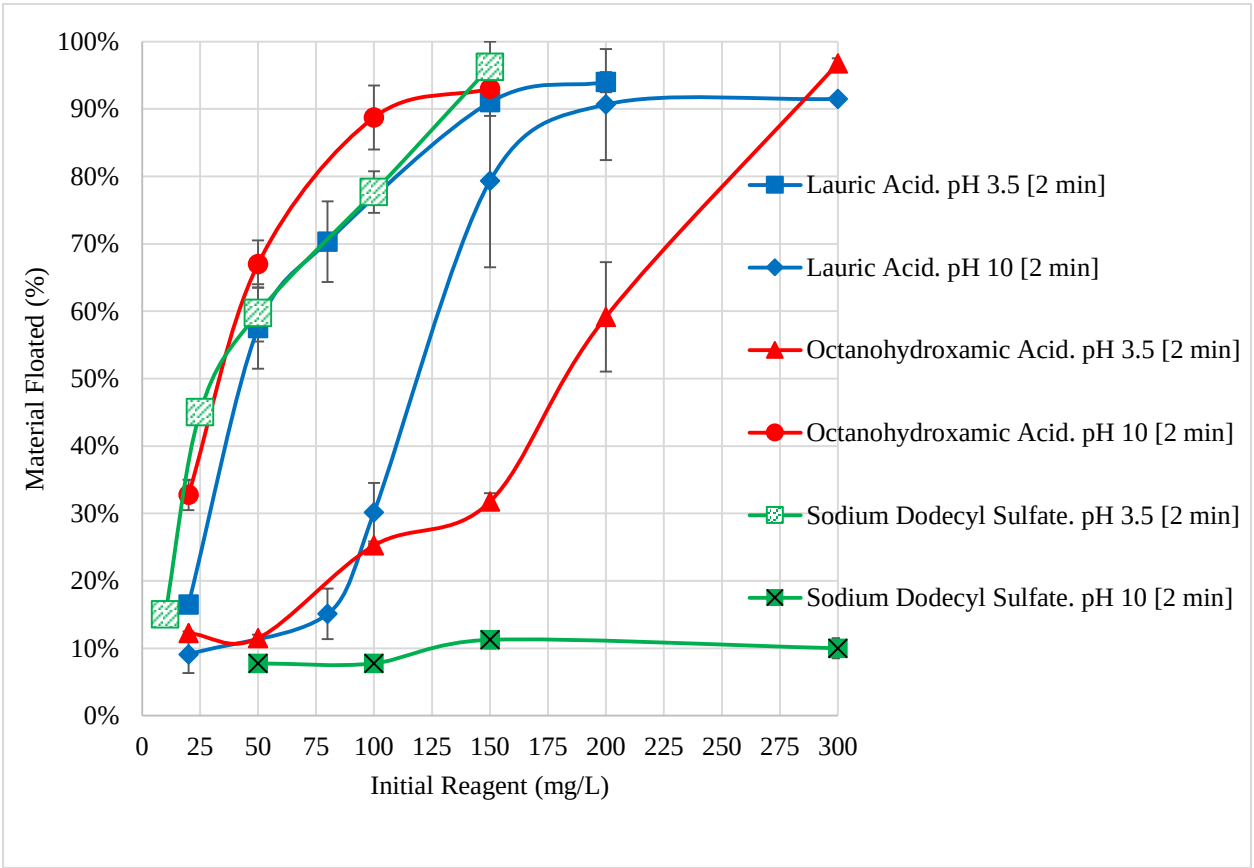


Figure 4-36: Surfactant Adsorption and Hallimond Tube Flotation Results for Low-Ag Sodium Jarosite.

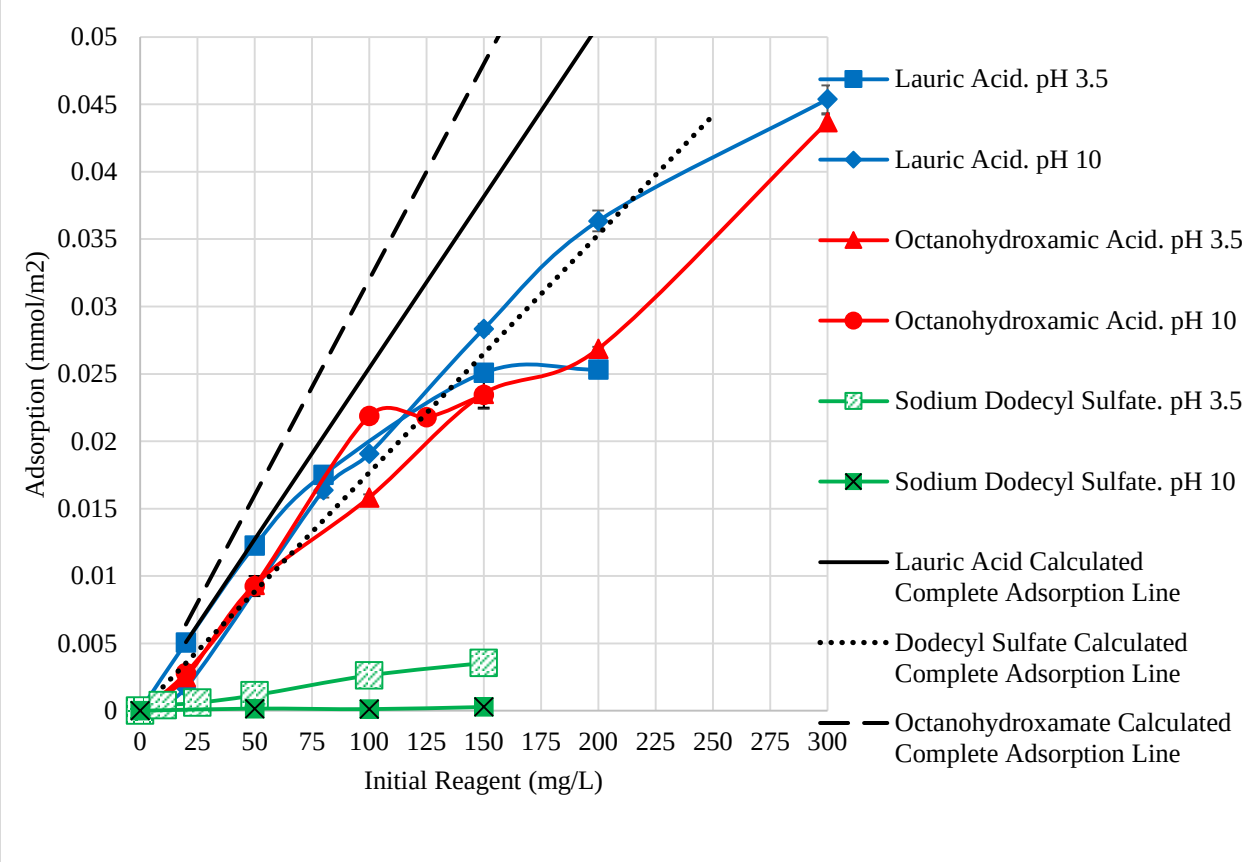


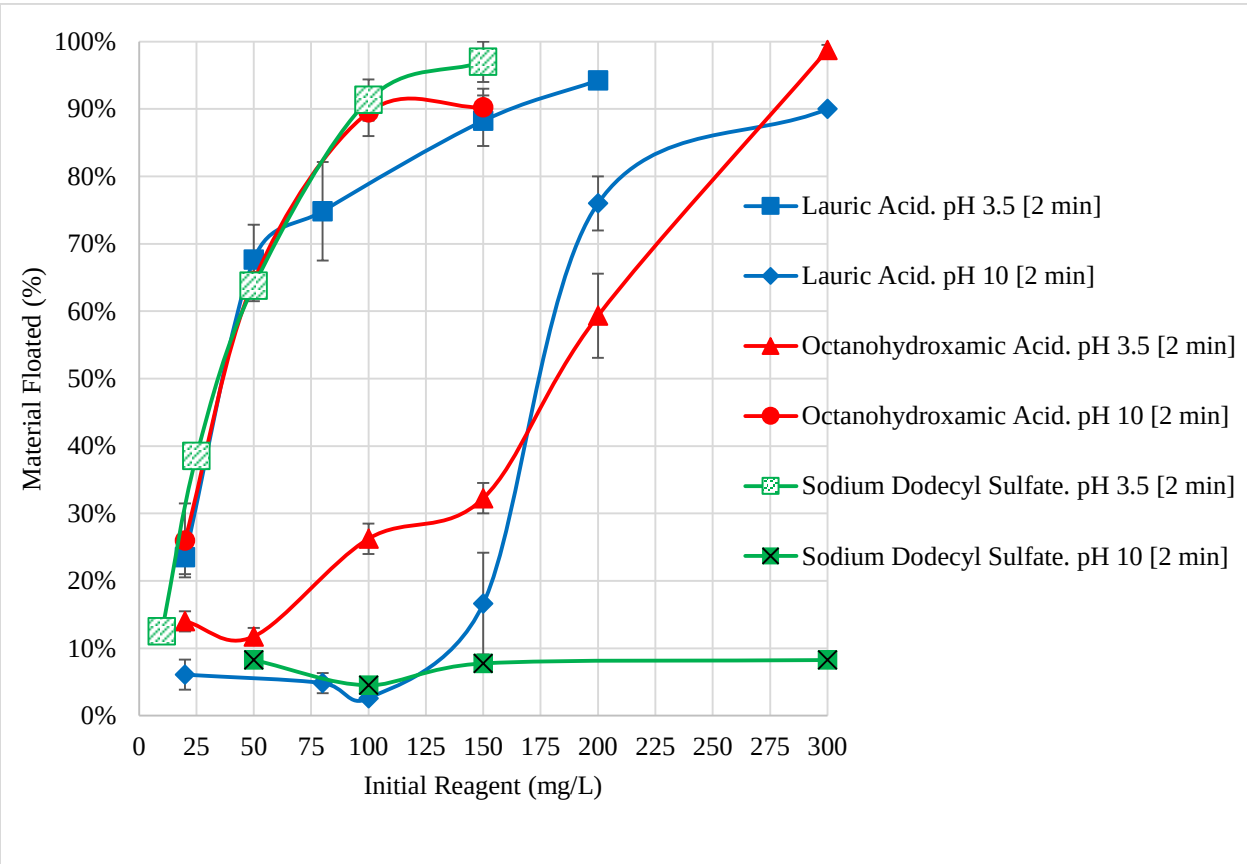


Figure 4-37: Surfactant Adsorption and Hallimond Tube Flotation Results for High-Ag Sodium Jarosite.

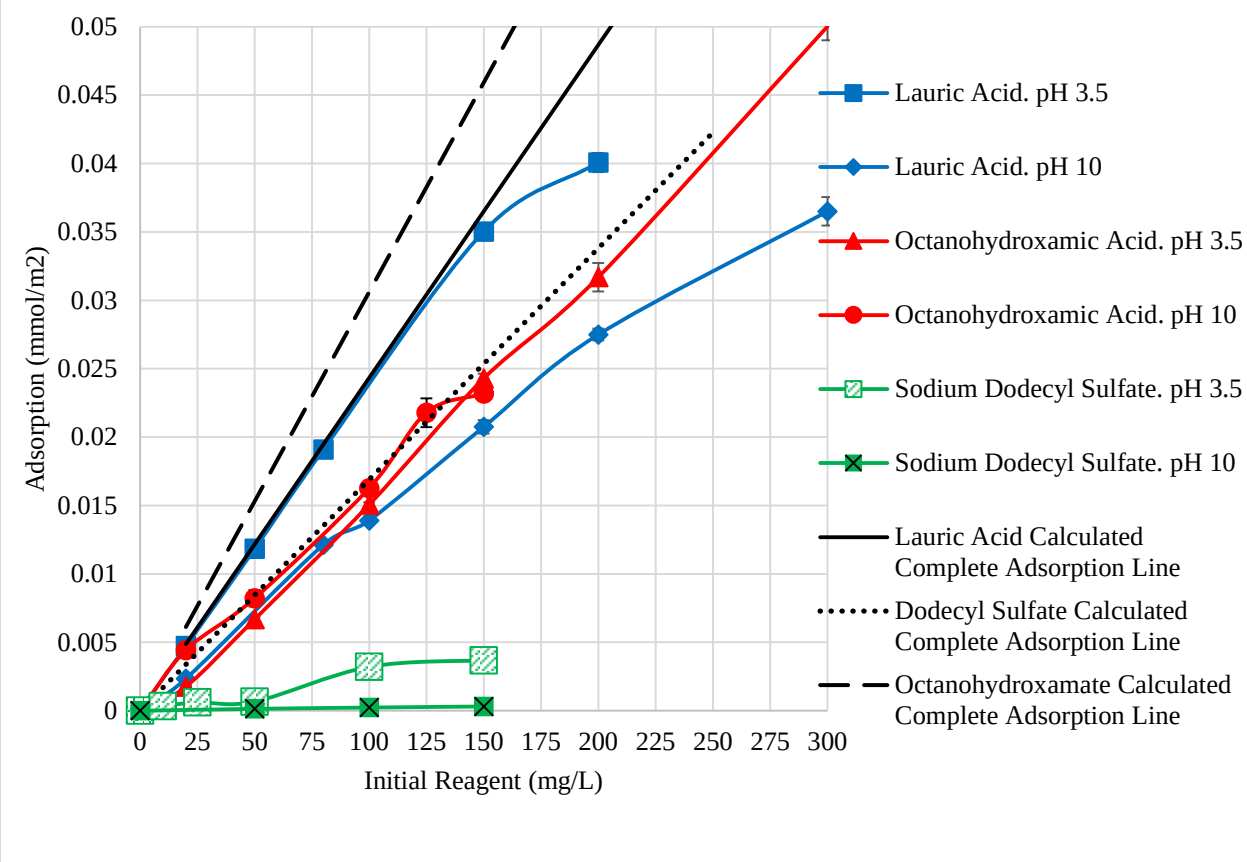


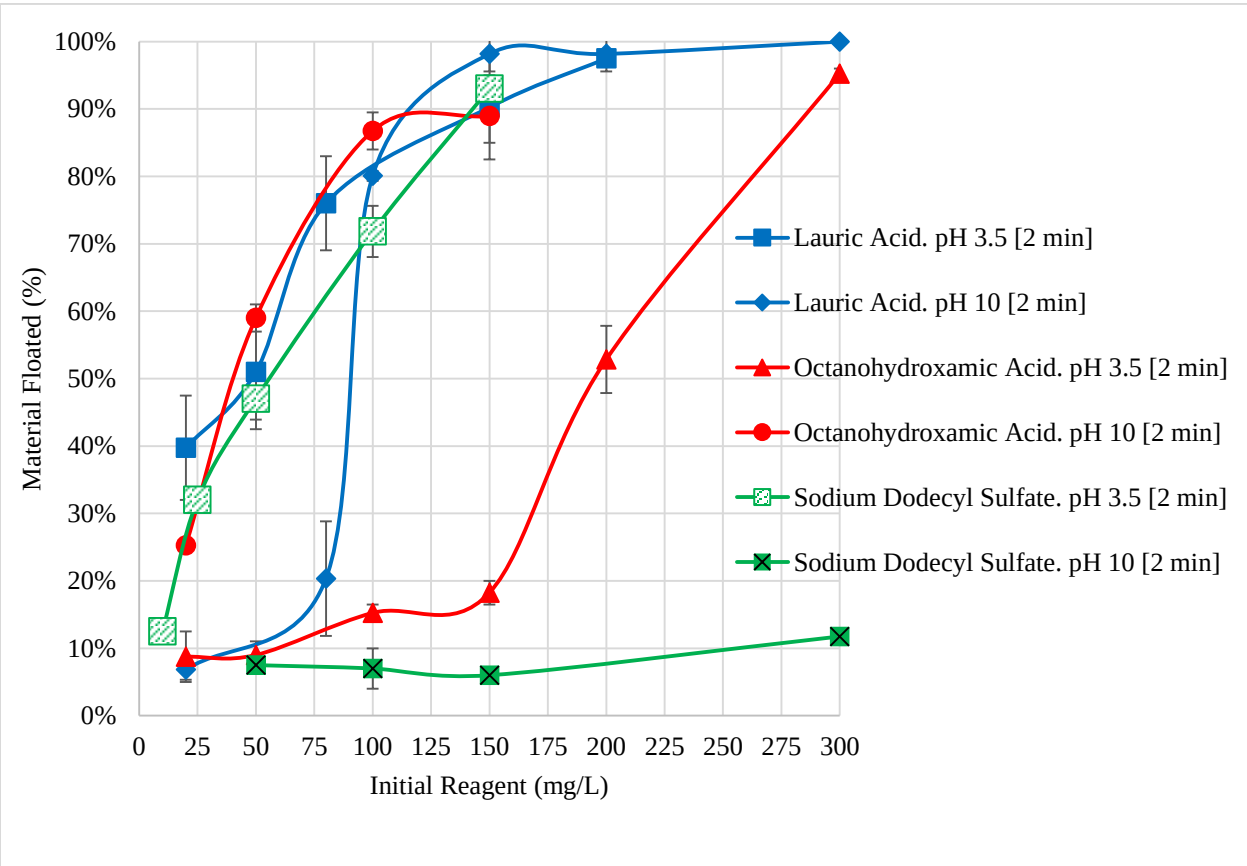


Figure 4-38: Surfactant Adsorption and Hallimond Tube Flotation Results for Potassium Jarosite (Baseline).

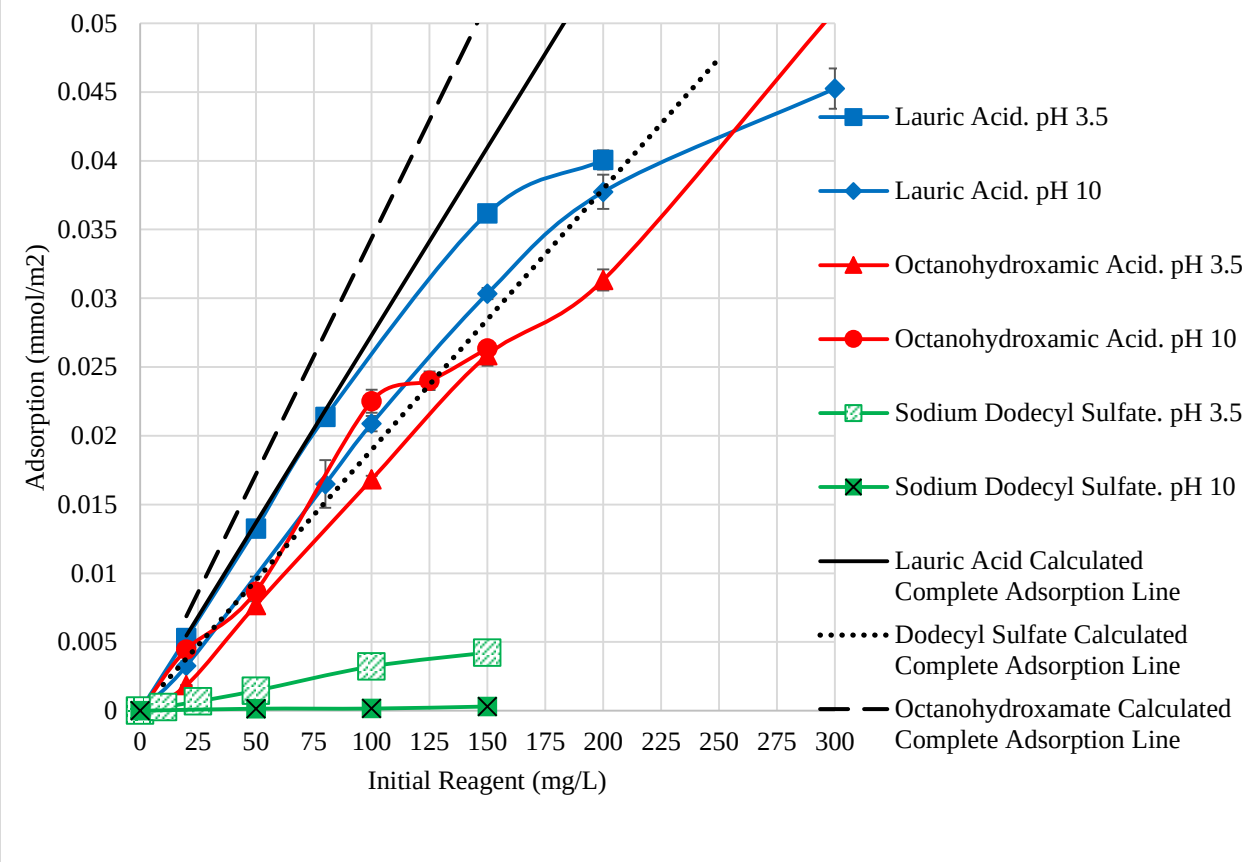


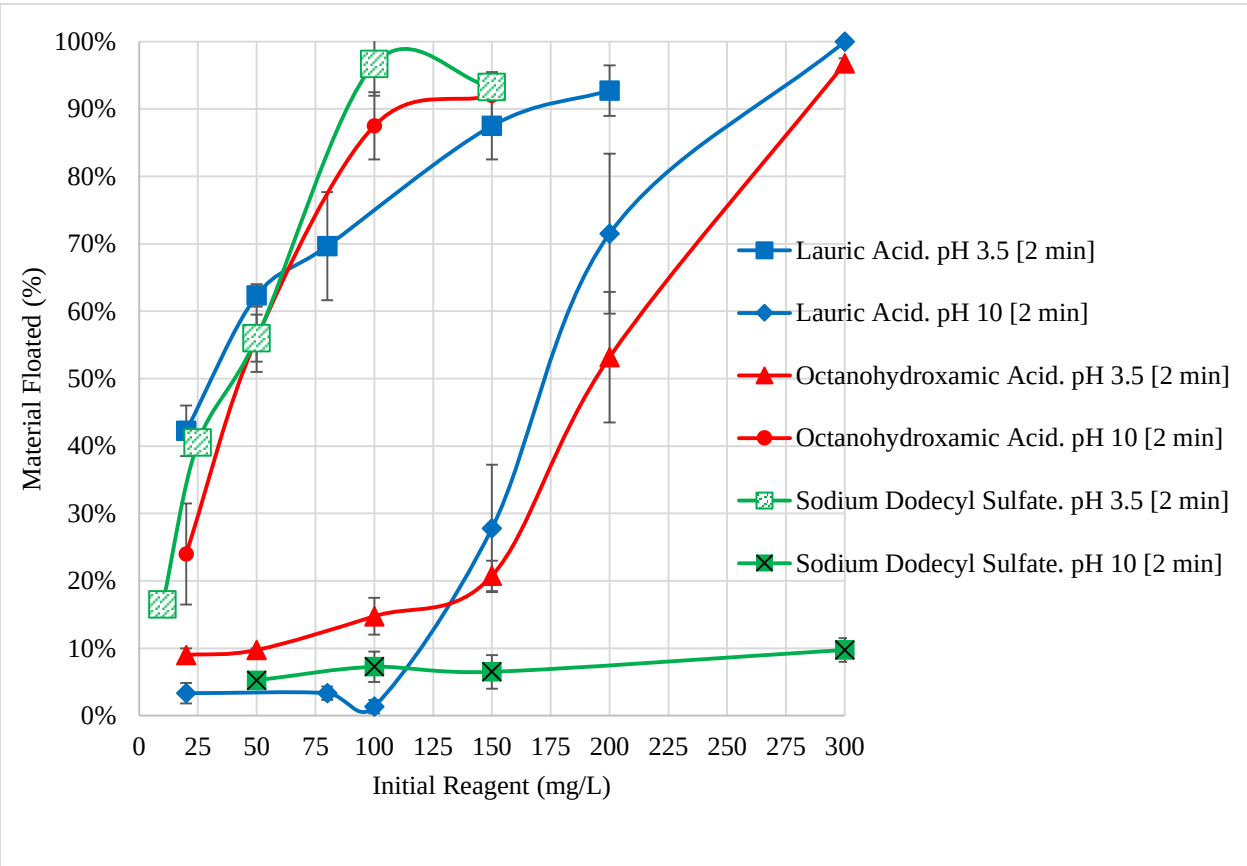


Figure 4-39: Surfactant Adsorption and Hallimond Tube Flotation Results for High-Ag Potassium Jarosite.

Summarizing all these results the Hallimond tube flotation results can be grouped into 3 main sets of flotation trends:

1) Those that exhibit a rapid increase in flotation with surfactant concentration:
    a. Lauric acid (pH 3.5) – all samples.
    b. Octanohydroxamic acid (pH 10) – all samples.
    c. Sodium dodecyl sulfate (pH 3.5) – all samples.
    d. Lauric acid (pH 10) – potassium/sodium (baseline), and low-silver sodium jarosite.
2) Those that require a higher concentration to initiate good flotation:
    a. Octanohydroxamic acid (pH 3.5) – all samples.
    b. Lauric acid (pH 10) – high-silver samples.
3) Those that produce poor flotation for all cases:
    a. Sodium dodecyl sulfate (pH 10) – all samples.

As the results show, all jarosites are readily floated by sodium dodecyl sulfate at low pH. Under alkaline conditions, octanohydroxamate offers the most promising results at relatively low concentrations. Although lauric acid produces high flotation at low concentrations under acidic conditions (similarly to sodium dodecyl sulfate), it is very likely that this reagent will not perform well in a mixture of minerals since the colloidal precipitate of lauric acid at low pH tends to indiscriminately interact with all components of a mixture. Generally speaking, fatty acids are not used as collectors under acidic conditions. High pH data for lauric acid consistently show that a much higher dosage of the reagent is required for good flotation compared to the other two surfactants.

### 4.5.6 Influence of Silver on Hallimond Tube Flotation

Silver content appears to have an impact on flotation under two sets of tested conditions (reagent concentration, pH): 150 mg/L lauric acid (pH 10) and 100 mg/L dodecyl sulfate (pH 3.5). For these two cases the low-silver sodium sample behaves similarly to the baseline sample. This is thought to be a result of the silver deficient coating preventing surfactant interactions with Ag. Hallimond tube flotation results, plotted as a function of silver, for these tests are

shown in Figure 4-40 for the 3 sodium samples and Figure 4-41 for the 2 potassium samples. Samples conditioned with dodecyl sulfate at pH 3.5 demonstrate that the increasing silver content increases the amount of material floated. Samples conditioned with lauric acid at pH 10 have the opposite effect, as silver content appears to be detrimental to the amount of material floated. These trends are the same regardless of sodium or potassium jarosite. It should be noted that these trends depend on the reagent concentration, and at higher dosages of the collectors it becomes impossible to identify any clear relationships between jarosite flotation, surfactant adsorption, and silver content in the jarosite samples. Nevertheless, these limited observations on the effect of silver again suggest that sodium dodecyl sulfate is a potential collector for silver jarosite flotation at low pH (and hydroxamate under alkaline conditions).

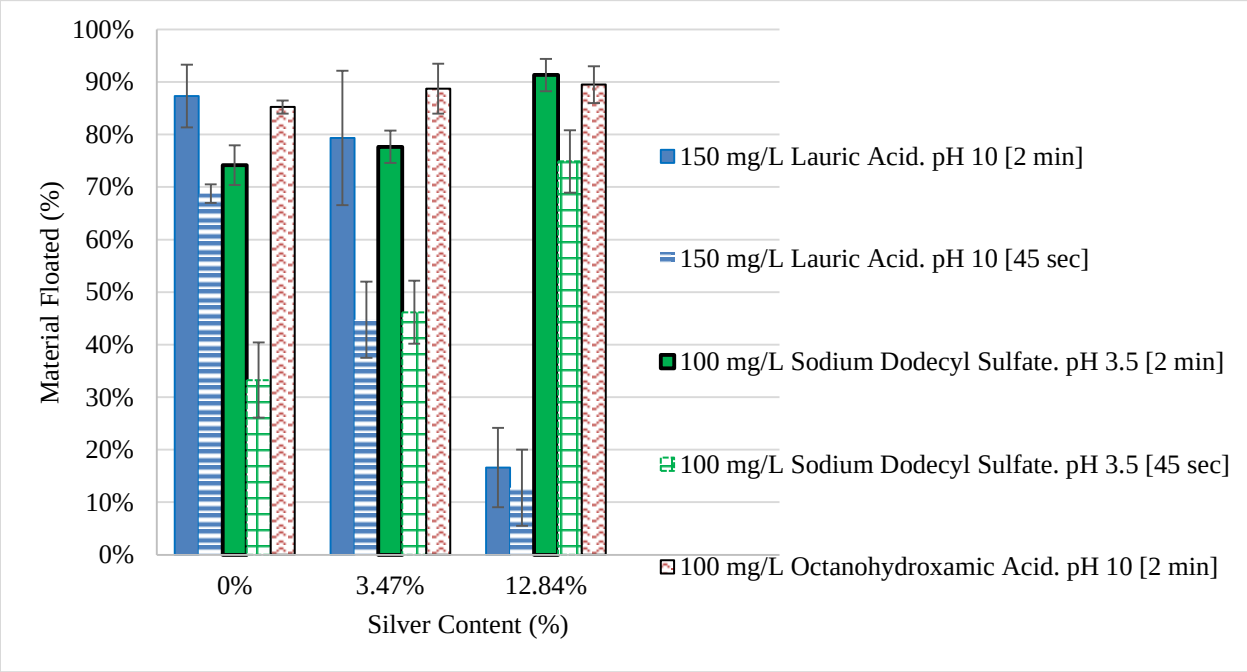


Figure 4-40: Impact of Silver on Sodium Jarosite Hallimond Tube Flotation.

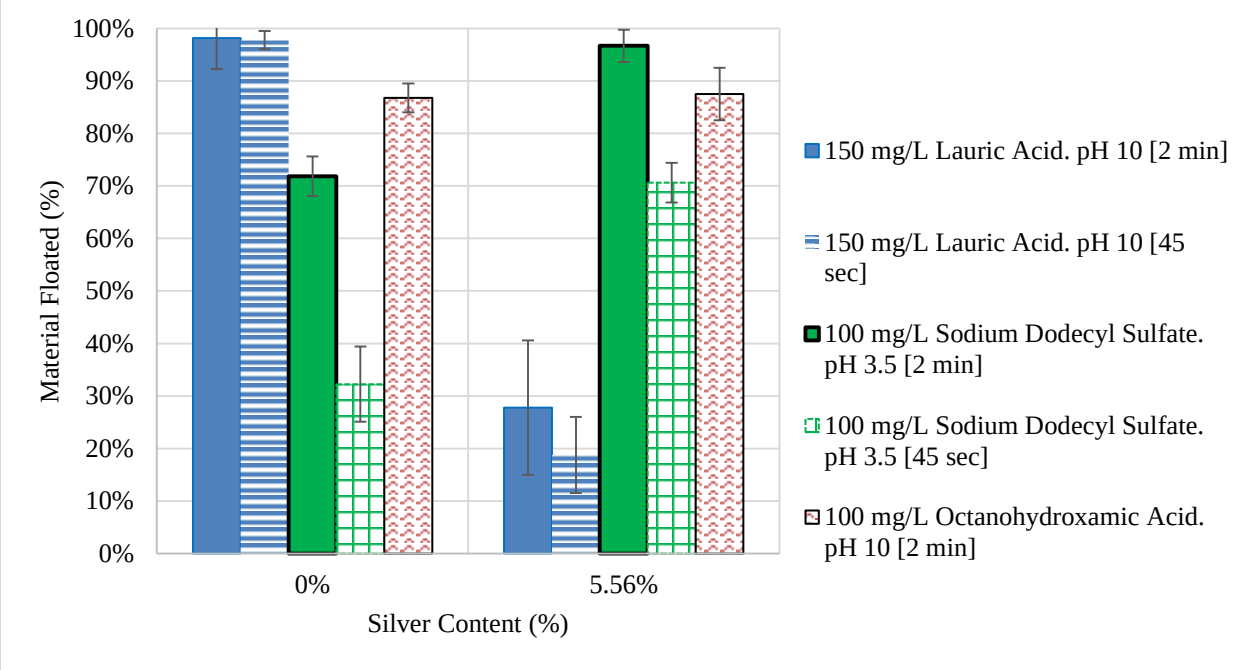


Figure 4-41: Impact of Silver on Potassium Jarosite Hallimond Tube Flotation.

## 4.6 Contact Angle

Contact angle measurements were conducted as triplicates with average results presented in Table 4-6 for experiments conducted at an unmodified pH [3.5], and in Table 4-7 for experiments conducted at pH 10. The method employed for measuring the contact angle (refer to Section 3.2.8) offered either large contact angles (>90$^{o}$) or complete wetting of the bed. Because of the inability of the technique to distinguish between contact angles from 0 to 90$^{o}$, tests resulting in apparent contact angles of 0$^{o}$ are record as N/A, and in all such cases the sessile droplet was spontaneously absorbed by the particle bed. Results conducted in this manner are not quantitatively accurate and are used merely as an indicator of the relative hydrophobicity. Flotation classifications are listed with contact angle results. These classifications are poor (P), moderate (M), and good (G). They are described in more detail at the beginning of Section 4.5. All samples were also tested with no chemical reagent added (both pH 3.5 and 10) to establish the baseline wetting behavior, and in all these cases the test resulted in the soaking in of the droplet, or in complete penetration and wetting of the particle bed.

Table 4-6: Contact Angle Measurements [pH 3.5].

| Jarosite Sample | Reagent (Dosage) – pH 3.5 | | | |
|---|---|---|---|---|
| | Lauric Acid (50 mg/L) | Lauric Acid (150 mg/L) | Sodium Dodecyl Sulfate (100 mg/L) | Sodium Dodecyl Sulfate (150 mg/L) |
| | Contact Angle (Degrees) | | | |
| Baseline Sodium | 132.6 (M) | 122.4 (G) | N/A (M) | 118.5 (G) |
| Low Silver Sodium | 126.7 (M) | 128.1 (G) | N/A (M) | 122.0 (G) |
| High Silver Sodium | 126.0 (M) | 124.0 (G) | N/A (G) | 117.8 (G) |
| Baseline Potassium | 119.1 (M) | 123.0 (G) | N/A (M) | 115.0 (G) |
| High Silver Potassium | 122.6 (M) | 124.9 (G) | N/A (G) | 112.1 (G) |

| Jarosite Sample | Reagent (Dosage) – pH 3.5 | |
|---|---|---|
| | Octanohydroxamic Acid (150 mg/L) | Octanohydroxamic Acid (300 mg/L) |
| | Contact Angle (Degrees) | |
| Baseline Sodium | N/A (P) | 118.8 (G) |
| Low Silver Sodium | N/A (P) | 112.6 (G) |
| High Silver Sodium | N/A (P) | 109.9 (G) |
| Baseline Potassium | N/A (P) | 122.9 (G) |
| High Silver Potassium | N/A (P) | 116.3 (G) |

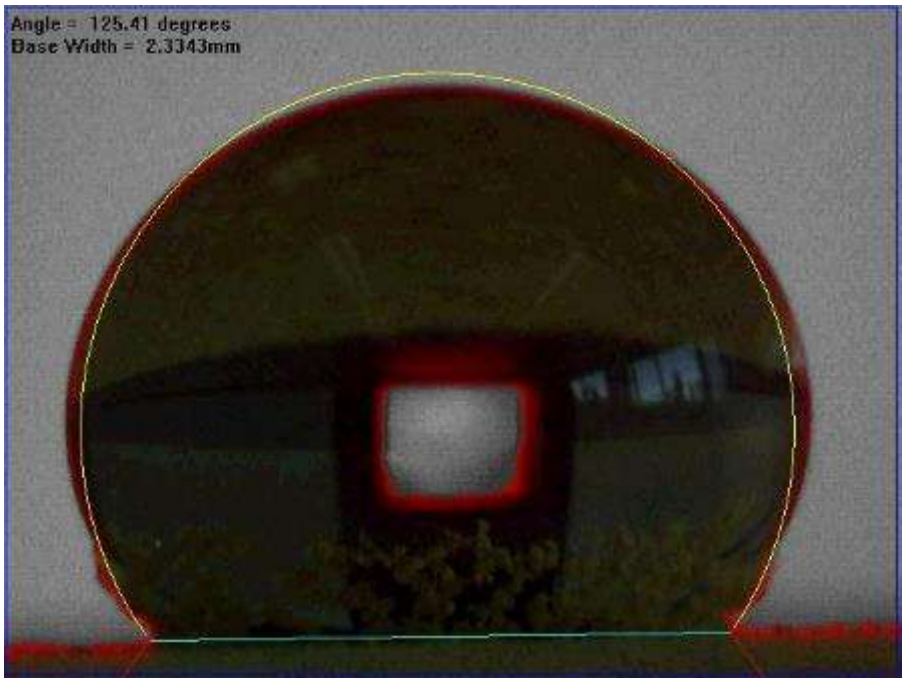


Figure 4-42: Lauric Acid Contact Angle (pH 3.5). 50mg/L High-Ag Potassium (125.41$^{o}$).

It should be noted that poor flotation is quite consistently accompanied by the lack of well-defined contact angle between the sessile droplet and the bed of jarosite particles. As discussed in Section (3.2.8), such a result should not however be interpreted as zero contact angle since the water droplet will spontaneously soak into the bed of jarosite particles at any contact angle lower than 90 deg. Contact angle measurements for dodecyl sulfate (100 mg/L at pH 3.5) did not mirror the positive effect that silver had on Hallimond tube flotation. At this concentration flotation of the high silver samples was very good, whereas contact angles for sessile droplets could not be measured. The reason behind this, as discussed in Section 3.2.8, is due to liquid penetration of the surface at contact angles less than 90$^{o}$. Other contact angle tests at pH 3.5 mirror the trends of Hallimond tube flotation. It is reasonable to conclude that the low adsorption of SDS produced substantial contact angles, sufficient to induce flotation, but they were all lower than 90°. The jarosite surfaces in the presence of dodecyl sulfate were not as hydrophobic as in the presence of lauric acid or hydroxamic acid. The data for dodecyl sulfate essentially indicate that very high contact angles, of about 100 degrees or so, are not necessary for good flotation, an observation that has been known for a very long time (Leja, 1982).

Table 4-7: Contact Angle Measurements [pH 10].

| Jarosite Sample | Reagent (Dosage) – pH 10 | | | |
|---|---|---|---|---|
| | Baseline | Lauric Acid (150 mg/L) | Lauric Acid (200 mg/L) | Sodium Dodecyl Sulfate (150 mg/L) |
| | Contact Angle (Degrees) | | | |
| Baseline Sodium | N/A (P) | 118.3 (M) | 114.0 (G) | N/A (P) |
| Low Silver Sodium | N/A (P) | 114.1 (M) | 116.9 (G) | N/A (P) |
| High Silver Sodium | N/A (P) | N/A (P) | 116.2 (M) | N/A (P) |
| Baseline Potassium | N/A (P) | 118.3 (G) | 109.6 (G) | N/A (P) |
| High Silver Potassium | N/A (P) | N/A (P) | 114.5 (M) | N/A (P) |

| Jarosite Sample | Reagent (Dosage) – pH 10 | |
|---|---|---|
| | Octanohydroxamic Acid (25 mg/L) | Octanohydroxamic Acid (150 mg/L) |
| | Contact Angle (Degrees) | |
| Baseline Sodium | N/A (P) | 111.5 (G) |
| Low Silver Sodium | N/A (P) | 118.7 (G) |
| High Silver Sodium | N/A (P) | 116.4 (G) |
| Baseline Potassium | N/A (P) | 116.2 (G) |
| High Silver Potassium | N/A (P) | 104.7 (G) |

Contact angles of jarosite samples conditioned with lauric acid (pH 10) correlate with the negative effect of silver at an initial concentration of 150 mg/L. When the concentration is raised to 200 mg/L, the high silver samples become highly hydrophobic, coinciding with an increase in their flotation. The contact angle results for both dodecyl sulfate and octanohydroxamic acid agree very well with their respective flotation data at pH 10, as good flotation in each case coincides with a high contact angle.

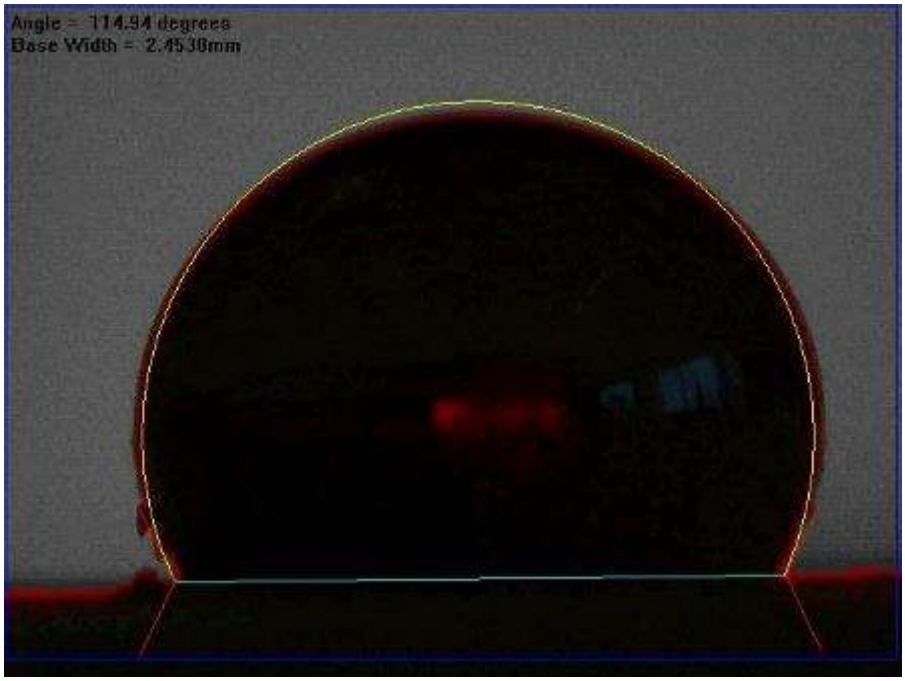


Figure 4-43: 150 mg/L Lauric Acid (pH 10). Sodium (Baseline) Contact Angle (114.94$^{o}$).

## 5.0 Conclusion

Five jarosite samples were synthesized in a Parr Autoclave and their surface properties relevant to flotation were examined. The five samples were: Sodium jarosite, low-silver sodium jarosite (3.47 % Ag), high-silver sodium jarosite (12.84% Ag), potassium jarosite, and high-silver potassium jarosite (5.56% Ag). The silver content was adjusted by varying the initial molar ratios of sodium (or potassium) to silver. Even though the high-silver potassium sample was synthesized under the same conditions as the high-silver sodium sample (0.3 M $Fe_2SO_4$, 0.06 M $AgSO_4$, 0.04 M $(Na/K)SO_4$), the resulting silver-potassium jarosite had a much lower silver content than the sodium counterpart. The two high-silver samples were a homogenous solid mixture of multiple M-site jarosites (K or Na with Ag and $H_3O^+$) formed during jarosite precipitation. The distribution of silver was found to be homogeneous within the entire volume of the jarosite particles, except the low-silver sodium jarosite sample that appeared to be coated with a thin, silver-deficient, sodium jarosite layer.

No differences were observed in the surface charge characteristics of the 5 samples in the pH range from 2 to 10. The tested jarosite samples exhibited a common isoelectric point at pH 5.

Reagent adsorption and Hallimond tube flotation experiments were conducted on single minerals with three anionic surfactants at pH 3.5 and at pH 10. The three reagents were: sodium laurate, sodium dodecyl sulfate, and octanohydroxamic acid.

The experimental results were analyzed in terms of correlations between zeta potential, surfactant adsorption, and flotation results in order to enhance the fundamental understanding of surfactant-jarosite interactions. It was found from the adsorption and flotation results that the floatability of jarosites in the presence of the tested reagents followed two main trends. For several jarosite-reagent-pH combinations, the floatability of the mineral increased steadily with the increasing adsorption density of the reagent. In other cases, a minimum concentration of the reagent was required to initiate flotation even though the adsorption density of the surfactant continuously increased. Based on the available literature data on surfactant adsorption on iron oxide minerals, it was postulated that in the latter case, the transition from poor to good flotation

coincided with a change in the adsorption mechanism of the surfactant, while in the former case, one mechanism dominated the interaction. When analyzing the adsorption data, it was also recognized that the jarosite surface at pH 10 was coated by a goethite (FeO(OH)) layer, while at pH 3.5 the surfactants adsorbed on a clean jarosite surface.

At low concentrations at high pH, lauric acid initially chemically adsorbs on the jarosite surface but the adsorbed layer does not offer sufficient hydrophobicity to induce flotation. Only when additional laurate anions adsorb through lateral hydrophobic interactions with the chemically adsorbed laurate anions (and hydrogen bonding with the jarosite surface), does the floatability of jarosites dramatically improve. High-silver jarosite samples required an increased concentration of lauric acid in order to see improved flotation results. Shortening the flotation time from 2 minutes to 45 seconds further stretched the range of poor flotation seen in the high-silver samples, while the baseline samples continued to demonstrate good floatation at lower initial concentrations of lauric acid. The shortened flotation times had no significant impact on the flotation results for the baseline samples.

A similar transition in the mode of adsorption was proposed to occur for hydroxamate at low pH, when the hydroxamic acid form is the main surfactant species in solution. In this case, the adsorption process initially proceeds through a single chemical bond between one oxygen from hydroxamic acid and an iron site on the jarosite surface without inducing flotation. At higher hydroxamic acid concentrations, the increasing number of so adsorbed surfactant molecules leads to reorganization (and dehydration) of the adsorbed layer to form bidentate complex bonds between both oxygen atoms from hydroxamic acid and iron sites on the surface. Under these conditions, (low pH, higher hydroxamic acid concentrations), the flotation of all jarosites was nearly complete. At high pH, the complete dissociation of the acid to form the hydroxamate anion facilitates the direct formation of the bidentate complex with the goethite-coated jarosite surfaces, leading to the observed excellent flotation even at lower hydroxamate concentrations.

Sodium dodecyl sulfate produced the lowest, barely detectable adsorption densities among the tested surfactants for all the jarosite samples and under all pH conditions. Adsorption takes place as an exchange process between sulfate ions from the jarosite surface and the

dodecyl sulfate anions from solution. Analysis of equilibrium solubility data from the literature (Smith et al, 2006) shows the maximum adsorption density of dodecyl sulfate on the jarosite surface, assuming ion exchange between sulfate and dodecyl sulfate, to be very low compared to the adsorption densities measured for the other surfactants. This observation suggests that adsorption of dodecyl sulfate indeed proceeds onto the vacant sites left after sulfate anions, and that adsorption on these sites should be very low. However, the flotation of the tested jarosites in the presence of sodium dodecyl sulfate was generally very good at low pH. This counterintuitive result was attributed to surfactant transfer to the jarosite surface by gas bubbles. In this scenario (Digre and Sandvik, 1966), the surfactant (collector) molecules exhibit a higher affinity to, and adsorb more densely on gas bubbles than on mineral particles. Attachment of particles to gas bubbles and flotation are still possible because additional collector molecules are brought to the particle surfaces by collisions with the surfactant-coated gas bubbles. In the case of dodecyl sulfate, this mode of interaction would be favored compared to the other surfactants due to the longest hydrocarbon tail of the molecule (C12 vs C11-lauric acid vs C8-hydroxamic acid). Additionally, the jarosite surfaces at low pH are positively-charged, which increases the probability of electrostatic attraction with the negatively charged, surfactant-carrying gas bubbles. Shortening of the flotation time from 2 minutes to 45 seconds revealed the high-silver jarosite samples to float faster. At high pH, no adsorption of dodecyl sulfate was detected on any of the jarosite samples, and no flotation was possible. At high pH, adsorption of dodecyl sulfate on the goethite-coated jarosite particles and their flotation were prevented by electrostatic repulsion between the negatively charged goethite layer on the jarosite particles and the fully dissociated anionic surfactant.

It was overall concluded that the adsorption of the anionic surfactants was driven by chemical interactions with iron sites on the jarosite surfaces regardless of the jarosite type. As a result, no systematic trends were observed as a function of the silver content. Based on all the data, sodium dodecyl sulfate appears to be a promising collector for all jarosites at low pH, while under alkaline conditions octanohydroxamic acid leads to excellent flotation of all the samples. These two surfactants offer excellent flotation at relatively low dosages.

## 6.0 Recommendations for Further Research

The results of this thesis were obtained for single minerals of well-defined composition, and under controlled chemistry of process water (pH and ionic strength). Selectivity of the recommended reagents should be verified. Mixtures of jarosites with other minerals, as well as actual leaching residues, should be tested through froth flotation experiments to determine silver grades and recoveries. The kinetics of jarosite flotation could also be determined from such data.

On the fundamental side, the role of silver in surfactant-jarosite interactions should be investigated in greater detail. A more systematic study focusing on the speciation of silver on jarosite surfaces should be carried out. Although goethite precipitation was observed at high pH, as also suggested by several published studies, the extent of precipitation and the coverage of the jarosite surfaces deserves a more systematic approach. A separate advanced surface characterization study (e.g., Fourier transform-IR or X-ray photoelectron spectroscopy) should also be performed.

A range of common anionic surfactants were studied as jarosite collectors. Considering that the isoelectric point of jarosites was identified at pH 5, these minerals may float well with cationic collectors, such as amines, at higher pH values. Primary alkyl amines are weak-electrolyte type surfactants whose speciation in solution is a function of pH (by analogy to fatty acids). However, quaternary amines are strong electrolytes and these surfactants are not affected by changes in pH. A similar fundamental study is recommended on the floatability of jarosites using typical industrial amines (primary, quaternary).

## 7.0 Bibliography


Alpers, C.N., Nordstrom, D.K. & Ball. J.W. (1989) Solubility of jarosite solid solutions precipitated from acid mine waters, Iron Mountain, California, U.S.A. *Sciences Geologiques*, 42(4), 281-298.

Arregui, V., Gordon, A.R., & Steintveit, G. (1979). Jarosite Process – Past, Present, and Future. *IEEE International Conference on Acoustics, Speech & Signal Processing*, 97-123.

Asokan, P. (2007). Application of some Inorganic Residues in Management of Hazardous Jarosite Waste. (PhD. Thesis (ENV-PHD-07-701)). Department of Environmental Science and Engineering, Indian Institute of Technology Bombay, Powai, Mumbai.

Baron, D., & Palmer, C.D. (1996). Solubility of jarosite at 4-35ºC. *Geochimica et Cosmochimica Acta*, 60(2), 185-195.

Basciano, L. (2008). Crystal Chemistry of the Jarosite Group of Minerals. *Queens University Doctorate Thesis, 1-196.*

Beccia, M.R. (2014). Hydroxamic acids interactions with metals in aqueous and micellar media: a mechanistic study of complexation reactions and metallacrown formation. *UNIVERSITÀ DI PISA Dipartimento di Chimica e Chimica Industriale Doctorate Thesis*, 1-147.

Bedi, A., Singh, B.R., Deshmukh, S.K., Aggarwal, N., Barrow, C.J., & Adholeya, A. (2018). Development of novel myconanomining approach for the recovery of agriculturally important elements from jarosite waste. *Journal of Environmental Sciences*, 67, 356-367.

Bolorunduro, S.A., Dreisinger, D.B., & Van Weert, G. (2003). Fundamental Study of Silver Deportment during the Pressure Oxidation of Sulphide Ores and Concentrates. *Minerals Engineering, 16(8)*, 695-708.

Bonda, C., Marks, J., Wroblewski, L., Raatikainen, H., Lenox, S., & Gebhardt, K. (2015). Human and Environmental Toxicity of Sodium Lauryl Sulfate (SLS): Evidence for Safe Use in Household Cleaning Products. *Environmental Health Insight*, 9, 27-32.

Brand, H.E.A., Scarlett, N.V.Y., & Grey, I.E. (2012). In situ studies into the formation kinetics of potassium jarosite. *Journal of Applied Crystallography*, 45, 535-545.

Brophy, G.P. (1965). Sulfate studies; [Part] 4, The jarosite-natrojarosite-hydronium jarosite solid solution series. *The American Mineralogist*, 50(10), 1595-1607.

Buckley, A.N. & Parker, G.K. (2013). Adsorption of n-octanohydroxamate collector on iron oxides. *International Journal of Mineral Processing*, 121, 70-89.

Casandra, A., Chung, M., Noskov, B.A., & Lin, S. (2017). Adsorption kinetics of sodium dodecyl sulfate on perturbed air-water interfaces. *Colloids and Surfaces A: Physiochemical and Engineering Aspects*, 518, 241-248.

Cogram, P.F. (2016). Capacity and mechanisms of uptake of silver by jarosite family minerals. *University of London Doctorate of Philosophy Thesis.*

Challa-Choque, D., Nava-Alonso, F., & Fuentes-Aceituno, J.C. (2016). Acid decomposition and thiourea leaching of silver from hazardous jarosite residues: Effect of some cations on the stability of the thiourea system. *Journal of Hazardous Materials*, 317, 440-448.

Chernyshova, I.V. Ponnurangam, S., & Somasundaran, P. (2011). Adsorption of Fatty Acids on Iron (Hydr)oxides from Aqueous Solutions. *Langmuir*, 27(16), 10007-10018.

Clogston, J., Patri, A. (2010). Zeta Potential Measurement. *Characterization of Nanoparticles Intended for Drug Delivery*, 697, 63-70.

Cosgrove, T., Editor (2005). *Colloid Science: Principles, Methods and Applications.* Blackwell Publishing.

Cosgrove, T., Editor (2010). *Colloid Science: Principles, Methods and Applications. 2nd Edition.* Blackwell Publishing.

Cruells, M., Roca, A., Patino, F., Salinas, E., & Rivera, I. (2000). Cyanidation kinetics of argentian jarosite in alkaline media. *Hydrometallurgy,* 55, 153-163.

Dabous, A. (2002). Uranium isotopic evidence for the origin of the Bahariya iron deposits, Egypt. *Ore Geology Reviews,* 19, 165-186.

Delgado, A.V., Editor (2002). Electrokinetic Phenomena and Their Experimental Determination: An Overview. *Interfacial Electrokinetics and Electrophoresis*. *Surfactant Science Series,* 106, 1-54.

Desborough, G.A., Smith, K.S., Lowers, H.A., Swayze, G.A., Hammarstrom, J.M., Diehl, S.F., Leinz, R.W., & Driscoll, R.L. (2010). Mineralogical and chemical characteristics of some natural jarosites. *Geochimica et Cosmochimica Acta*, 74, 1041-1056.

Digre, M. & Sandivik, Kl. (1968). Adsorption of amine on quartz through bubble interaction, 77(739 Sec C), c61-4.

Drzymala, J. (2007). Mineral Processing. *Foundations of theory and practice of minerallurgy,* 213-225.

Drouet, C., & Navrotsky, A. (2003). Synthesis, Characterization, and Thermochemistry of K-Na-H3O Jarosites. *Geochimica et cosmochimica acta, 67(11),* 2063-2076.

Dutrizac, J.E. (1983). Factors Affecting Alkali Jarosite Precipitation. *Metallurgical Transactions, 14B,* 531-539.

Dutrizac, J.E. (1984). The Behaviour of Impurities during Jarosite Precipitation. *Hydrometallurgical Process Fundamentals,* 125-169.

Dutrizac, J.E. (1996). Effect of Seeding on the Rate of Precipitation of Ammonium Jarosite. *Hydrometallurgy, 42(3),* 293-312.

Dutrizac, J.E. (1999). Effectiveness of Jarosite Species for Precipitating Sodium Jarosite. *Journal of the Minerals, Metals, and Materials Society, 51(12),* 30-32.

Dutrizac, J.E. (2004). The Behaviour of the Rare Earths during the Precipitation of Sodium, Potassium, and Lead Jarosites. *Hydrometallurgy, 73(1),* 11-30.

Dutrizac, J.E. (2010). Comparative Rates of Precipitation of Ammonium Jarosite and Sodium Jarosite in Ferric Sulphate – Sulphuric Acid Media. *Canadian metallurgical Quarterly,* 49(2), 121-130.

Dutrizac, J.E., & Chen, T.T. (2004), Factors Affecting the Incorporation of Cobalt and Nickel in Jarosite. *Canadian Metallurgical Quarterly, 43(3),* 305-320.

Dutrizac, J.E., & Jambor, J. (1987). Behaviour of Silver during Jarosite Precipitation. *Institution of Mining and Metallurgy, 96,* 206-218.

Dutrizac, J.E., & Jambor, J. (2000). Jarosites and Their Application in Hydrometallurgy. *Reviews in Minerology and Geochemistry, 40,* 405-452.

Dutrizac, J.E., & Kaiman, S. (1976). Synthesis and Properties of Jarosite-type Compounds. *Canadian Mineralogist, 14,* 151-158.

Eastoe, J. (2010). Surfactant Aggregation and Adsorption at Interfaces. *Colloid Science: Principles, Methods and Applications. 2nd Edition,* Chapter 4.

Elwood Madden, M.E., Bodnar, R.J., & Rimstidt J.D. (2004). Jarosite as an indicator of water-limited chemical weathering on Mars. *Nature Journal,* 431, 821-823.

Elwood Madden, M.E., Madden, A.S., Rimstidt, J.D., Zahrai, S.K., Kendall, M.R., & Miller, M.A. (2012). Jarosite dissolution rates and nanoscale mineralogy. *Geochimica Cosmochimica Acta,* 91, 306-321.

Fairchild, J.G. (1933). Artificial Jarosites – Separation of Potassium from Cesium. *The American Mineralogist, 18,* 543-547.

Forray, F.L., Smith, A.M.L., Drouet, C., Navrotsky, A., Wright, K., Hudson-Edwards, K.A., Dubbin, W.E. (2010). Synthesis, characterization and thermochemistry of a Pb-jarosite. *Geochimica et Cosmochimica Acta,* 74, 215-224.

Frederick, M., & Everdingen, R. (1987). Formation of a Jarosite Deposit on Cretaceous Shales in the Fort Norman Area, Northwest Territories. *Canadian Mineralogist,* 25(2), 221-226.

Fuerstenau, D.W. (2001). Excess nonequilibrium collector adsorption and flotation rates. *Minerals & Metallurgical Processing,* (18), 83-88.

Fuerstenau, D.W. (2007a). A Century of Developments in the Chemistry of Flotation Processing. *Frother Flotation a Century of Innovation,* 6.

Fuerstenau, D.W. (2007b). Insoluble Oxides and Silicates. *Frother Flotation a Century of Innovation,* 495-503.

Fuerstenau, D.W., Herrera-Urbina, R., & McGlashan, D.W. (2000). Studies on the applicability of chelating agents as universal collectors for copper minerals. *International Journal of Mineral Processing,* 58, 15-33.

Fuerstenau, D.W., & Raghavan, S. (2007). Some Aspects of Flotation Thermodynamic. *Froth Flotation A Century of Innovation*, Chapter 6, 93-104.

Fuerstenau, M.C. Miller, J.D., & Gutierrez, G. (1967). Selective flotation of iron oxide. Trans. AIME, 238, 200-203.

Ganguly, A. (2012). Fundamentals of Inorganic Chemistry for Competitive Examinations. *Pearson Publishing*, 2nd edition.

Gasharova, B., Gottlicher, J., & Becker, U. (2005). Dissolution at the Surface of Jarosite: an in situ AFM Study. *Chemical Geology*, 215, 499-516.

Gonzalez-Ibarra, A.A., Nava-Alonso, F., Uribe-Salas, A., & Castillo-Ventureno, E.N. (2016). Decomposition kinetics of industrial jarosite in alkaline media for the recovery of precious metals by cyanidation. *Canadian Metallurgical Quarterly*, 1-7.

Grey, I.E., Scarlett, N.V.Y., & Brand, H.E.A. (2013) Crystal Chemistry and Formation Mechanisms of Non-Stoichiometric Monoclinic K-jarosites. *Mineralogical Magazine*, 77(3), 249-268.

Groat, L.A., Jambor, J.L., & Pemberton, B.C. (2003). The Crystal Structure of Argentojarosite, $AgFe_3(SO_4)_2(OH)_6$. *The Canadian Mineralogist, 41*, 921-928.

Gunaratnam, A.A., Dreisinger, D.B., & Choi, Y. (2018). Characterisation of solid phases in the iron-sulphate-water system where silver is present. *Canadian Metallurgical Quarterly. The Canadian Journal of Metallurgy and Materials Science.* https://doi.org/10.1080/00084433.2018.1431076

Gupta, C. (2006). Chemical Metallurgy. Principles and Practice. *Published by John Wiley and Sons.*

Gupta, C., & Prasas, A. (2018). Strength and Durability of Lime-Treated Jarosite Waste Exposed to Freeze and That. *Journal of Cold Regions Engineering,* 32(1), 04017025 1-11.

Gwyther, D. (2004). Impact of the deposition of jarosite on deepwater meiobenthos in southeastern Australia. *Marine Pollution Bulletin,* 48(9-10), 997-1003.

Han, H., Sun, W., Hu, Y., Jia, B., & Tang H. (2014). Anglesite and Silver Recovery from Jarosite Residues Through Sulfidization-flotation and Zinc Hydrometallurgy. *Journal of Hazardous Materials, 278,* 49-54.

Han, K.N., Healy, T.W., & Fuerstenau, D.W. (1973). The mechanism of adsorption of fatty acids and other surfactants at the oxide-water interface. *Journal of Colloid and Interface Science,* 44(3), 407-414.

Hage, J.T.L., & Schuiling, R.D. (2000). Comparative column elution of jarosite waste and its autoclaved product – evidence for the immobilization of deleterious elements in jarosite. *Minerals Engineering,* 13(3), 287-296.

Higgins, F., Magliocco, L., & Colthup, N. (2006). Infrared and Ramen Spectroscopy Study of Alkyl Hydroxamic Acid and Alkyl Hydroxamate Isomers. *Society for Applied Spectroscopy,* 60(3), 279-287.

Holley, E., Bissig, T., & Monecke, T. (2016). The Veladero High –Sulfidation Epithermal Gold Deposit, El Indio-Pascua Belt, Argentina: Geochronology of Alunite and Jarosite. *Economic geology and the bulletin of the Society of Economic Geologists,* 111(2), 311-330.

Holmen, B.A., Tejdor-Tejdor, M.I., Casey, W.H. (1997). Hydroxamate Complexes in Solution and at the Goethite-Water Interface: A Cylindrical Internal Reflection Fourier Transform Infrared Spectroscopy Study. *Langmuir,* 13, 2197-2206.

Hope, G., Woods, R., & Parker, G. (2010). Interaction of Hydroxamates with Malachite. *Electrochemistry in Mineral and Metal Processing, 28(6),* 27.

Israelachvili, J. (1985). Intermolecular and Surface Forces. Academic Press Inc.

Iwasaki, I., Cooke, S.R.B., & Colombo, A.F. (1960). Flotation Characteristics of Goethite. *U.S. Department of the Interior, Bureau of Mines.*

Jones, F.S., Bigham, J.M., Gramp, J.P., Tuovinen, O.H. (2018). Formation and characterization of ternary (Na, $NH_4$, $H_3O$)-jarosites produced from Acidithiobacillus ferrooxidans cultures. *Journal of Applied Geochemistry,* 91, 14-22.

Jordens, A., Marion, C., Kuzmina, O., & Waters, W. (2014). Surface Chemistry Considerations in the Flotation of Bastnäsite. *Minerals Engineering, 66,* 119-129.

Ju, S., Zhang, Y., Zhang, Y., Xue, P., & Wang, Y. (2011). Clean Hydrometallurgical Route to Recover Zinc, Silver, Lead, Copper, Cadmium, and Iron from Hazardous Residues Produced during Zinc Hydrometallurgy. *Journal of Hazardous Materials, 192,* 554-558.

Kato, T., & Miura, Y. (1977). The crystal structures of jarosite and svanbergite. *Mineralogical Journal,* 8(8), 419-430.

Katsioti, M., Boura, P., Agatzini, S., Tsakiridis, P.E. & Oustadakis, P. (2005). Use of jarosite/alunite precipitate as a substitute for gypsum in Portland cement. *Cement and Concrete Composites,* 27(1), 3-9.

Kaushik, S. (2012). Surface Properties of Crandallite in Relation to Froth Flotation. *Master of Applied Science Thesis, University of British Columbia.*

Koh, P., & Schwarz, M.P. (2003). CFD modelling of bubble-particle collision rates and efficiencies in a flotation cell. *Minerals Engineering,* 16, 1055-1059.

Lakshmipathiraj, P., Narasimhan, B.R.V., Prabhakar, S., & Bhasker Raju, G. (2006). Adsorption of arsenate on synthetic goethite from aqueous solutions. *Journal of Hazardous Materials,* B136, 281-287.

Laskowski, J. S. (1999). Weak Electrolyte Collectors. *Society for Mining, Metallurgy, and Exploration. Advances in Flotation, 59-82.*

Lee, J.S. (1998). Practical Aspects of Copper Oxide Recovery with Alkyl Hydroxamates. *Minerals Engineering, 11(10),* 929-939.

Leja, J. (1982). Surface Chemistry of Froth Flotation. Plenum Press.

Li, L., & Stanforth, R. (2000). Distinguishing Adsorption and Surface Prcipitation of Phosphate on Goethite (α-FeOOH). *Journal of Colloid and Interface Science,* 230, 12-21.

Liu, C., Zhang, J., Srinivasakannan, C., Peng, J.H., Le, T.Q.X., Guo, Z.Y. (2016). Recovery of Valuable Metals from Jarosite by Sulphuric Acid Roasting Using Microwave and Water Leaching. *Canadian Metallurgical Quarterly*.

May, A., Sjoberg, J.J., & Baglin, E.G. (1973). Synthetic Argentojarosite: Physical Properties and Thermal Behavior. *The American Mineralogist, 58(9),* 936-941.

Mills, S.J., Nestola, F., Kahlenber, V., Christy, A.G., Hejny, C., & Redhammer, G.J. (2013). Looking for jarosite on Mars: The low-temperature crystal structure of jarosite. *American Mineralogist*, 98, 1966-1971.

Mombelli, D., Mapelli, C., Cecca, C.D., Barella, S., Gruttadauria, A., Pisu, M., & Viola, A. (2018). Characterization of cast iron and slag produced by jarosite reduction via Arc Transferred Plasma (ATP) reactor. *Journal of Environmental Engineering,* 6, 773-783.

Mukherjee, C., Jones, F., Bigham, J., & Tuovinen, O. (2016) Synthesis of argentojarosite with simulated bioleaching solutions produced by Acidithiobacillus ferrooxidans. *Materials Science and Engineering C, 66*, 164-169.

Murphy, D., & Gilkes, R. (2010). Clay minerals in saprolite overlying hydrothermally altered and unaltered rocks, Vera Epithermal gold deposit, Australia. *Clays and Clay Minerals,* 58(6), 783-791.

Najorka, J., Lewis, J., Spratt, J., & Sephton, M. (2016). Single-crystal X-ray diffraction study of synthetic sodium-hydronium jarosite. *Phys Chem Minerals,* 43, 377-386.

NanoComposix. (2012). Zeta Potential Analysis of Nanoparticles. Retrieved from: http://50.87.149.212/sites/default/files/nanoComposix%20Guidelines%20for%20Zeta%20Potential%20Analysis%20of%20Nanoparticles.pdf

Natarajan, R. (2013). Hydroxamic Acids as Chelating Mineral Collectors. *Hydroxamic Acids,* 281-307.

Nguyen, A.V., Schulze, H.J., & Ralston, J. (1997). Elementary steps in particle-bubble attachment. *International Journal of Mineral Processing,* 51, 183-195.

Ohshima, H. (2002). Electrophoresis of Charged Particles and Drops. *Interfacial Electrokinetics and Electrophoresis*. *Surfactant Science Series,* 106, 123-146.

Patino, F., Roca, A., Reyes, M., Cruells, M., Rivera, I., & Leticia, E.H. (2010). Kinetic Modeling of the Alkaline Decomposition and Cyanidation of Argentojarosite. *Journal of the Mexican Chemical Society,* 54(4), 216-222.

Patino, F., Salinas, E., Cruells, M., & Roca, A. (1998). Alkaline decomposition – cyanidation kinetics of argentian natrojarosite. *Hydrometallurgy,* 49, 323-336.

Pappu, A., Saxena, M., & Asolekar, S.R. (2007). Solid wastes generation in India and their recycling potential in building materials. *Build Environment,* 42, 2311-2320.

Pappu, A., Saxena, M., Asolekar, S.R. (2011). Waste to wealth-cross sector waste recycling opportunity and challenges. Can. J. Environ. Construct. Eng. 2 (3), 14–23.

Peck A.S., Raby L.H., & Wadsworth M.E. (1966). An infrared study of the flotation of hematite with oleic acid and sodium oleate. *Transactions of AIME,* 235, 301-306.

Pelino, M. (2000). Recycling of zinc-hydrometallurgy wastes in glass and glass ceramic materials. *Waste Manage*, 20 561–568. http://dx.doi.org/10.1016/S0956-053X(00)00002-7.

Ponnurangam, S., Chernyshova, I.V. & Somasundaran, P. (2012). Rational Design of Interfacial Properties of Ferric (Hydr)oxide Nanoparticles by Adsorption of Fatty Acids from Aqueous Solutions. *Langmuir,* 28(29), 10661-10671.

Pope, M.I. & Sutton, D.I. (1972). Collector adsorption during froth flotation. *Powder Technology,* 5, 101-104.

Pritchett, B.P., Elwood Madden, M.E., & Madden, A.S. (2012). Salinity and Temperature Effects on the Dissolution of Natrojarosite and K-Jarosite. *43rd Lunar and Planetary Science Conference, held March 19-23, 2012 at The Woodlands, Texas. LPI Contribution No. 1659, id.2331*.

Quast, K.B. (2000). A Review of Hematite Flotation using 12-Carbon Chain Collectors. *Minerals Engineering*, 13(13), 1361-1376.

Quast, K.B. (2015). Use of conditioning time to investigate the mechanisms of interactions of selected fatty acids on hematite Part II laboratory investigations. *Minerals Engineering*, 79, 301-305.

Reyes, I.A., Mireles, I., Patino, F., Pandiyan, T., Flores, M., Palacios, E.G., Gutierrez, E.J., & Reyes, M. (2016). A study on the dissolution rates of K-Cr(VI)-jarosites: kinetic analysis and implications. *Geochemical Transactions,* 17(3).

Reyes, I.A., Patino, F., Flores, M.U., Pandiyan, T., Cruz, R., Gutierrez, E.J., Reyes, M., & Flores, V.H. (2017). Dissolution rates of jarosite-types compounds in $H_2SO_4$ medium: A kinetic analysis and its importance on the recovery of metal values from hydrometallurgical wastes. *Hydrometallurgy,* 167, 16-29.

Reynolds, P. (2010). Wetting of Surfaces. *Colloid Science: Principles, Methods and Applications. 2nd Edition,* Chapter 10.

Riley, A.L., Pepper, S.E., Canner, A.J. Brown, S.F., & Ogden, M.D. (2018). Metal recovery from jarosite waste – A resin screening study. *Separation Science and Technology,* 53(1), 22-35.

Roca, A., Patino, F., Vinals, J., & Nunez, C. (1993). Alkaline decomposition – cyanidation kinetics of argentojarosite. *Hydrometallurgy, 33,* 341-358.

Sadowski, Z., Polowczyk, I., Farbiszewska, T., & Farbiszewkska-Kiczma, T. (2001). Adhesion of Jarosite Particles to the Mineral Surface. *Prace Naukowe Instytutu Gornictwa Politechniki Wroclawskiej, 95,* 95-103.

Sasaki, K., & Konno, H. (2000). Morphology of jarosite-group compounds precipitated from biologically and chemically oxidized Fe ions. *The Canadian Mineralogist,* 38, 45-56.

Schempp, C.A. (1923). Argento-Jarosite; a New Silver Mineral. *American Journal of Science, 6(31),* 73-75.

Sewell, D., & Wheatley, C. (1994). The Lerokis and Kali Kuning submarine exhalative gold-silver-barite deposits, Wetar Island, Maluku, Indonesia. *Journal of Geochemical Exploration,* 50, 351-370.

Smeaton, C. (2012). Investigating the Susceptibility of Jarosite Minerals to Reduce Dissolution by a Dissimilatory Metal Reducing Bacterium. *University of Windsor Electronic Thesis and Dissertations*, Paper 450, 1-240.

Smith, A. (2004). Mechanisms and Products of ht eBreakdown of Contaminant Element-Bearing Jarosites. *University of London Doctorate of Philosophy Thesis.*

Smith, A., Hudson-Edwards, K., Dubbin, W., & Wright, K. (2006). Dissolution of Jarosite [$KFe_3(SO_4)_2(OH)_6$] at pH 2 and 8: Insights from Batch Experiments and Computational Modelling. *Geochimica et Cosmochimica Acta*, 70.

Singh, M., Rajesh, V.J., Sajinjumar, K.S., Sajeev, K., & Kumar, S.N. (2016). Spectral and chemical characterization of jarosite in a palaeolacustrine depositional environment in Warkalli Formation in Kerala, South India and its implications. *Spectrochimica Acta Part A: Molecular and Biomolecular Spectroscopy, 168*, 86-97.

Swan, J.M. & Furst, E.M. (2012). A simpler expression for Henry's function describing electrophoretic mobility of spherical colloids. *Journal of Colloid and Interface Science,* 388, 92-94.

Velasco, F., Herrero, J.M., Suarez, S., Yusta, I., Alvaro, A., & Tornos, F. (2013). Supergene features and evolution of gossans capping massive sulphide deposits in the Iberian Pyrite Belt. *Ore Geology Reviews,* 53, 181-203.

Vurdela, R.M. & Laskowski, J.S. (1987) Positively Charged Colloidal Species in Aqueous Anionic Surfactant Solutions. *Colloids and Surfaces*, 22, 77-80.

Wasan, D.T., Ginn, M.E., & Shah, D.O. (1988). Surfactants in Chemical/Process Engineering. *Surfactant Science Series*, 28.

Wang, H., Bigham, J.M., Jones, F.S., & Tuovinen, O.H. (2007). Synthesis and properties of ammoniojarosites prepared with iron-oxidizing acidophilic microorganisms at 22-65ºC. *geochimica et Cosmochimica Acta,* 71, 155-164.

Washburn, E.W. (1921). The dynamics of capillary flow. *Physical Review,* 17(3), 273-283.

Welch, S.A., Kirste, D., Christy, A.G., & Beavis, F.R. (2008). Jarosite dissolution II – Reaction kinetics, stoichiometry, and acid flux. *Chemical Geology*, 254, 73-86.

Xu, Z., Lu, B., Wu, J., Zhou, L., & Lan, Y. (2013). Reduction of Cr(VI) facilitated by biogenetic jarosite and analysis of its influencing factors with response surface methodology. *Materials and Science Engineering C*, 33, 3723-3729.

Yan, H. (2016). Collector Transfer between Bubble and Particle Collision. *University of British Columbia MASc Thesis.* 1-89.

Yuan, Y., & Lee, T. (2013). Contact Angle and Wetting Properties. *Surface Science Techniques,* 51, 3-34.

Zadeh, M.H., Tangestani, M.H., Roldan, F.V., & Yusta, I. (2014). Spectral characteristics of minerals in alteration zones associated with porphyry copper deposits in the middle part of the Kerman copper belt, SE Iran. *Ore Geology Reviews,* 62, 191-198.

Zahrai, S.K., Elwood Madden, M.E., Madden, A.S., & Rimstidt, J.D. (2013). Na-jarosite dissolution rates: The effect of mineral composition on jarosite lifetimes. *Icarus,* 223, 438-443.

Zhang, X., Du, H., Wang, X., & Miller, J.D. (2014). Surface chemistry aspects of bastnaesite flotation with octyl hydroxamate. *International Journal of Mineral Processing,* 133, 29-38.

Zhang, W., & Honaker, R. (2017). A fundamental study of octanohydroxamic acid adsorption on monazite surface. *International Journal of Mineral Processing*, 164, 26-36.

Zhao, R., Yi, L., Chan, C. (2016). Synthesis of Jarosite and Vanadium Jarosite Analogues Using Microwave Hydrothermal Reaction and Evaluation of Composition Dependent Electrochemical Properties. *The Journal of Physical Chemistry,* 120, 9702-9712.

# 8.0 Appendix

## 8.1 Additional SEM Images of Tested Jarosite Samples

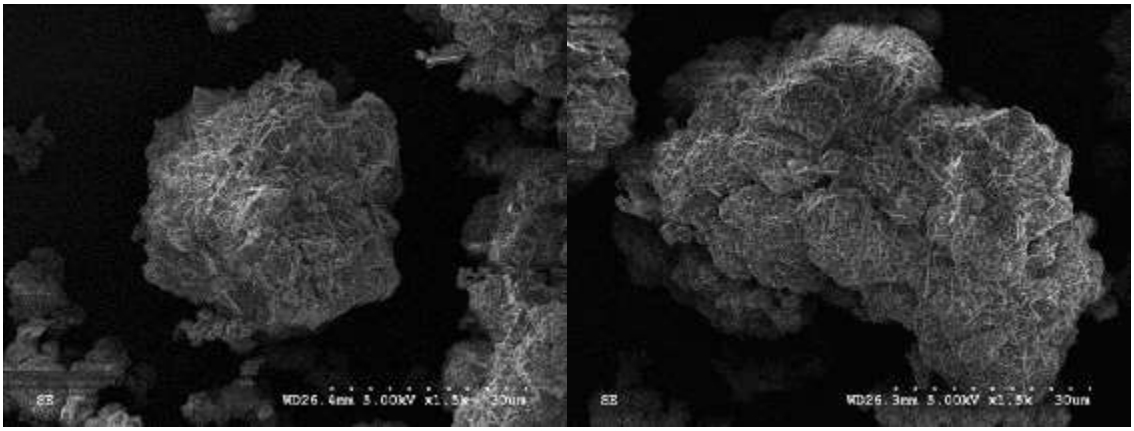

Figure 8-1: SEM images of sodium jarosite (baseline).

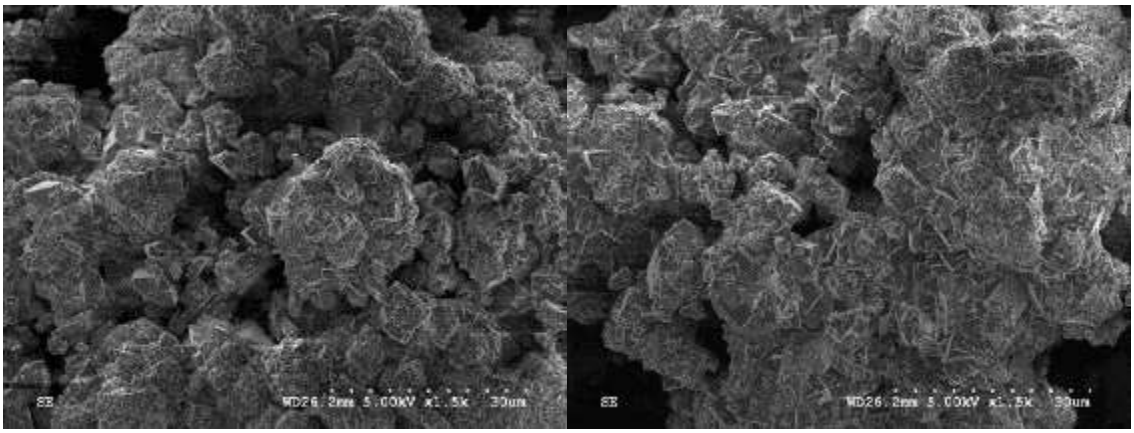

Figure 8-2: SEM images of low-silver sodium jarosite.

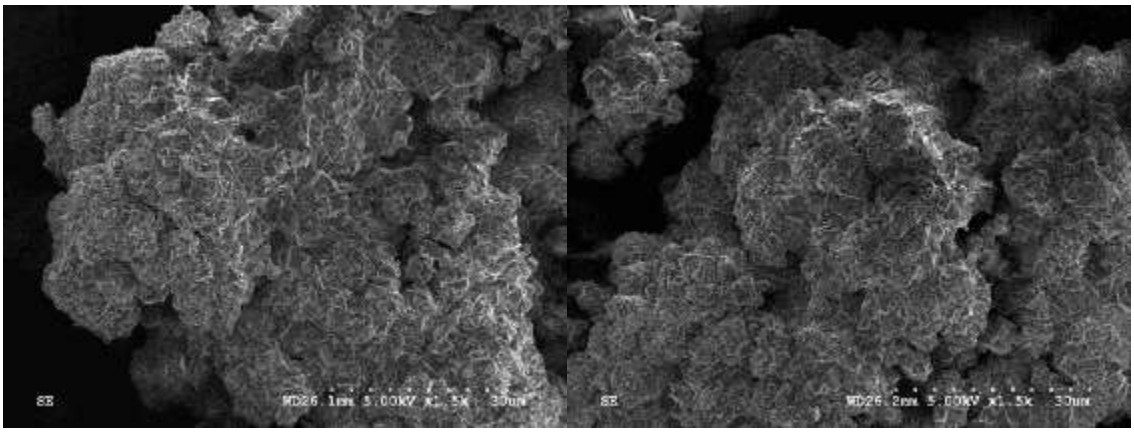

Figure 8-3: SEM images of high-silver sodium jarosite.

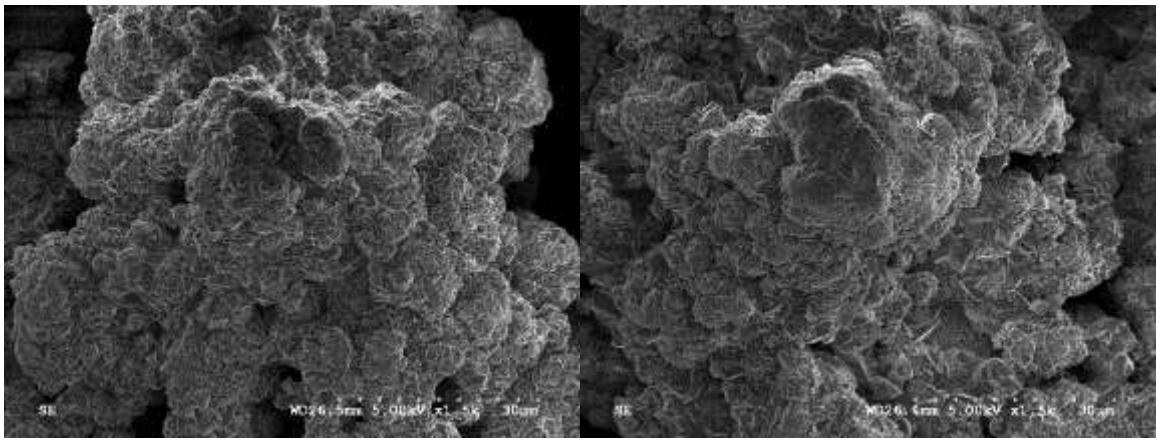

Figure 8-4: SEM images of potassium (baseline) jarosite.

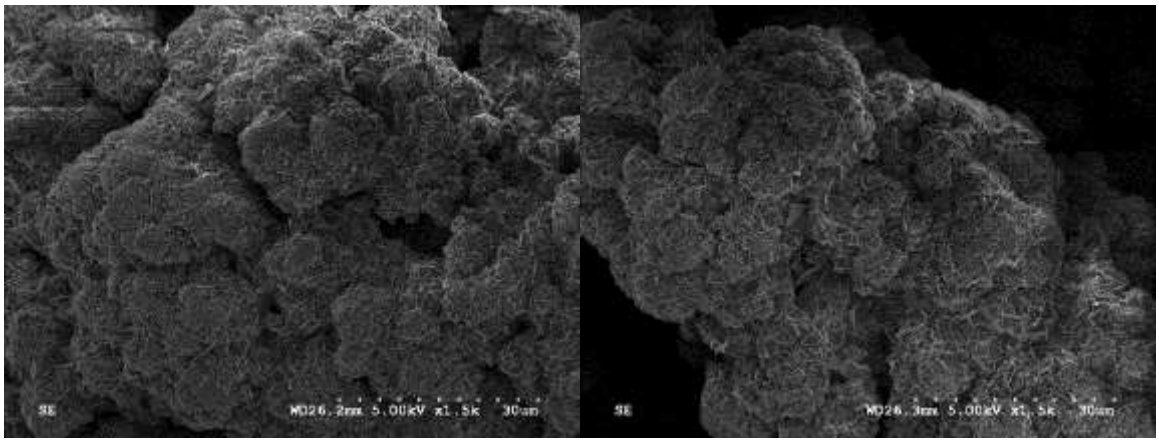

Figure 8-5: SEM images of high-silver potassium jarosite.

## 8.2 X-ray Diffraction Patterns of Jarosite Samples

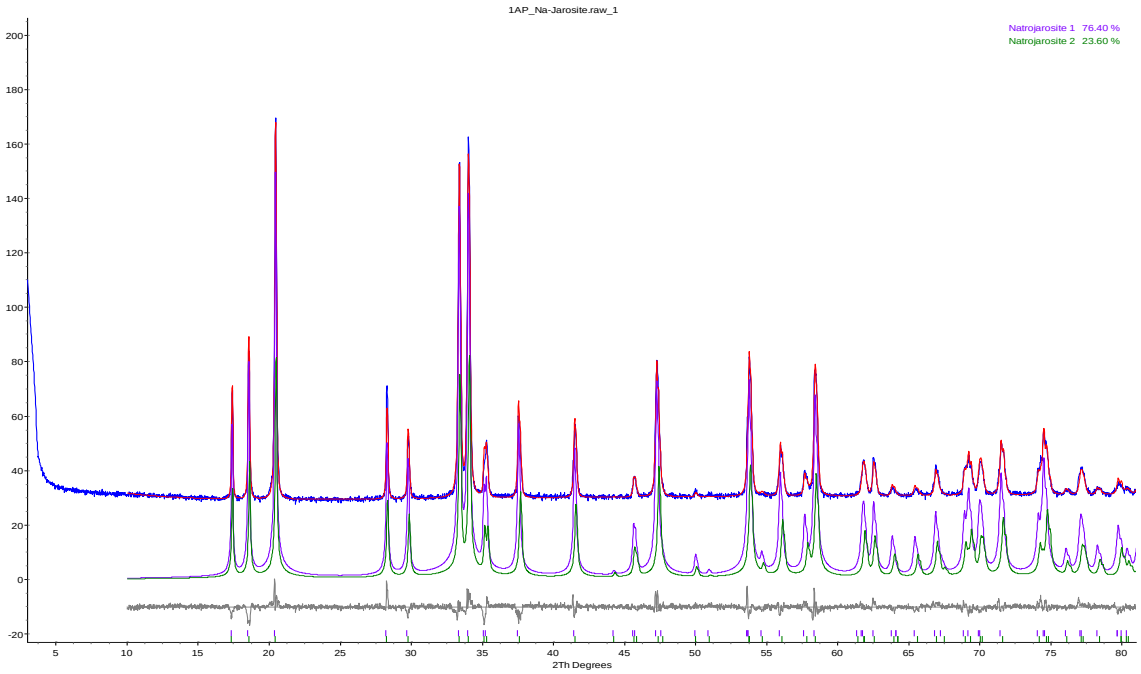


Figure 8-6: Rietveld refinement plot of sodium (baseline) jarosite (blue line – observed intensity at each step; red line – calculated pattern; solid grey line below – difference between observed and calculated intensities; vertical bars – positions of all Bragg reflections). Purple and green lines are individual diffraction patterns of the two individual jarosite phases.

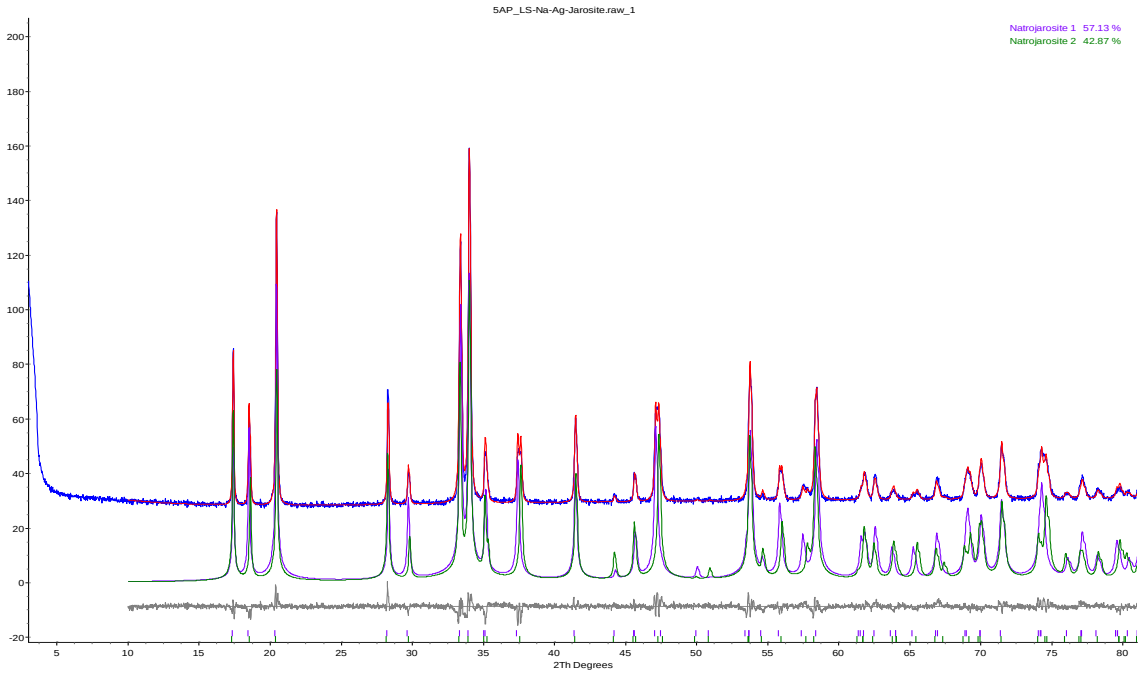


Figure 8-7: Rietveld refinement plot of low-silver sodium jarosite (blue line – observed intensity at each step; red line – calculated pattern; solid grey line below – difference between observed and calculated intensities; vertical bars – positions of all Bragg reflections). Coloured lines are individual diffraction patterns of the two individual jarosite phases.

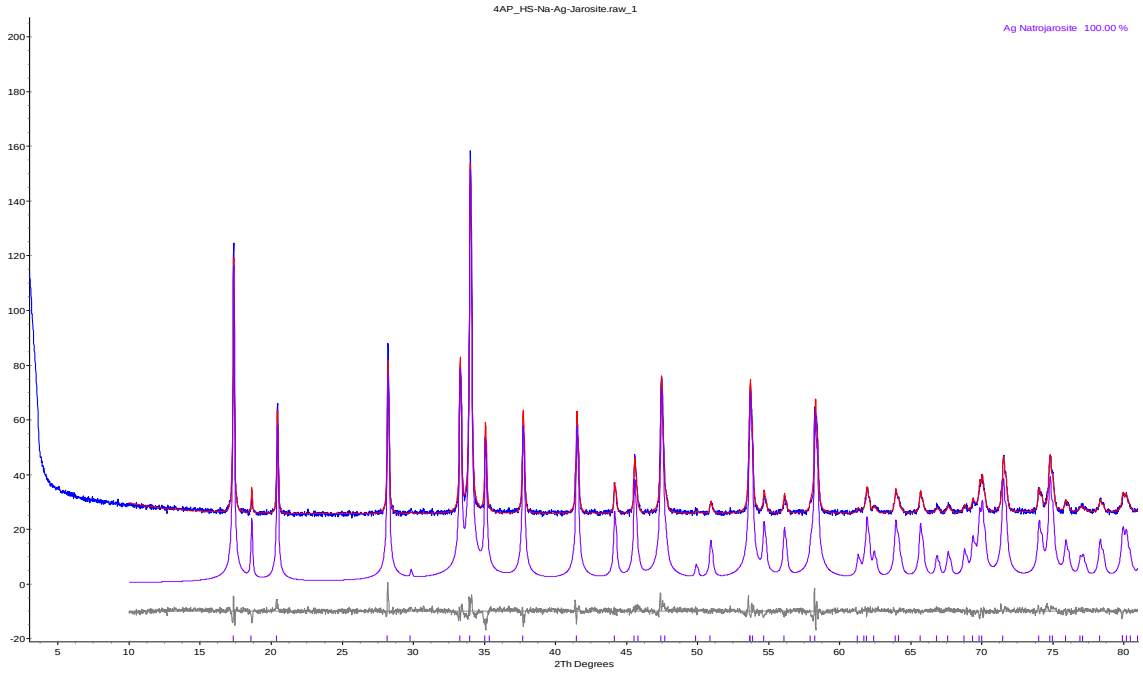


Figure 8-8: Rietveld refinement plot of high-silver sodium jarosite (blue line – observed intensity at each step; red line – calculated intensity; solid grey line below – difference between observed and calculated intensities; purple line – individual diffraction pattern of all phases).

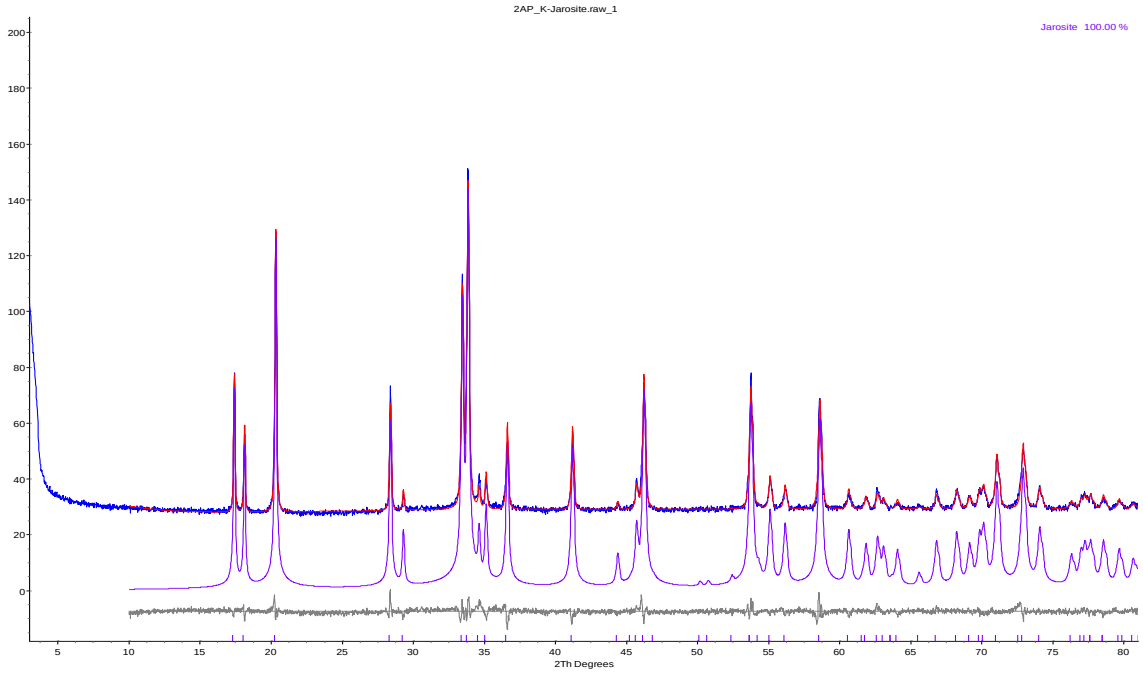


Figure 8-9: Rietveld refinement plot of high-silver sodium jarosite (blue line – observed intensity at each step; red line – calculated intensity; solid grey line below – difference between observed and calculated intensities; purple line – individual diffraction pattern of all phases).

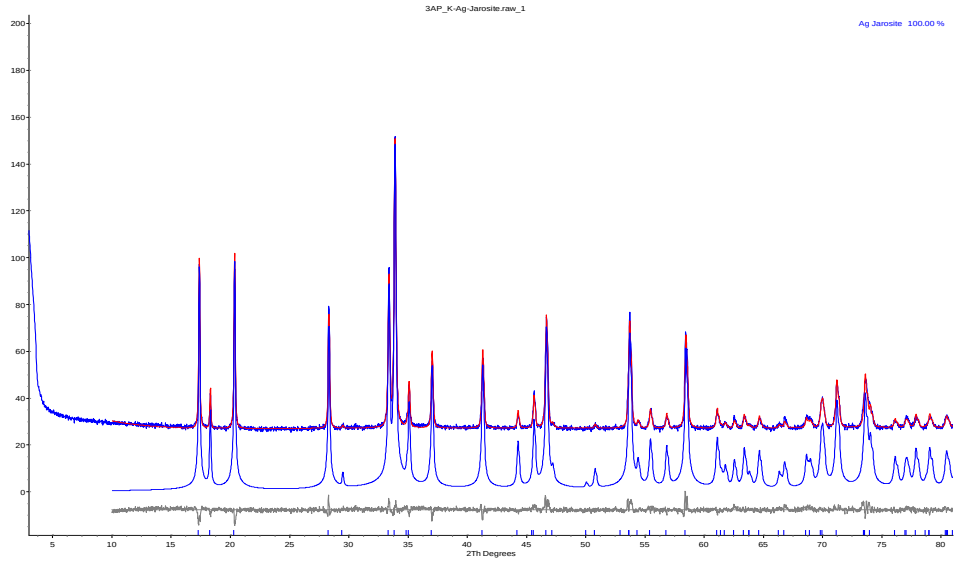


Figure 8-10: Rietveld refinement plot of high-silver potassium jarosite (blue line (upper) – observed intensity at each step; red line – calculated intensity; solid grey line below – difference between observed and calculated intensities; blue line (lower) – individual diffraction pattern of all phases).

Table 8-1: Jarosite Experimental Unit Cell Parameters.

| Sample | M Cation | a (Å) | c (Å) | V (Å$^3$) |
|---|---|---|---|---|
| Baseline Na-jarosite | Na | 7.34 | 16.71 | 779.5 |
| | Na | 7.33 | 16.65 | 774.8 |
| Low silver Na-jarosite | Na/Ag | 7.34 | 16.77 | 782.1 |
| | Na/Ag | 7.35 | 16.68 | 780.5 |
| High silver Na-jarosite | Na/Ag | 7.35 | 16.62 | 777.9 |
| Baseline K-jarosite | K | 7.32 | 17.13 | 795.1 |
| Silver K-jarosite | K/Ag | 7.33 | 16.94 | 789.1 |
| Available literature data | | | | |
| Reference | M Cation | a (Å) | c (Å) | V (Å^3) |
| Najorka et al. (2016) | Na | 7.33 | 16.73 | 777.9 |
| Zhao et al. (2016) | Na | 7.34 | 16.64 | - |
| Brophy (1965) | Na | 7.31 | 16.62 | - |

| Reference | M Cation | a (Å) | c (Å) | V (Å^3) |
|---|---|---|---|---|
| Dutrizac and Kaiman (1976) | Na | 7.33 | 16.70 | - |
| Dutrizac and Jambor (1987) | K | 7.32 | 17.13 | - |
| Kato and Miura (1977) | K | 7.30 | 17.27 | - |
| Dutrizac and Kaiman (1976) | K | 7.32 | 17.12 | - |
| Mukherjee et al. (2016) | Ag | 7.35 | 16.57 | 774.7 |
| | | 7.35 | 16.53 | 773.3 |
| | | 7.35 | 16.54 | 772.9 |
| Sasaki & Konno (2000) | Ag | 7.35 | 16.61 | 771.1 |
| May et al. (1973) | Ag | 7.35 | 16.56 | 774.8 |
| Groat et al. (2003) | Ag | 7.34 | 16.54 | 771.4 |
| Dutrizac and Kaiman (1976) | Ag | 7.35 | 16.55 | - |
| Dutrizac and Jambor (1987) | Ag | 7.34 | 16.56 | - |

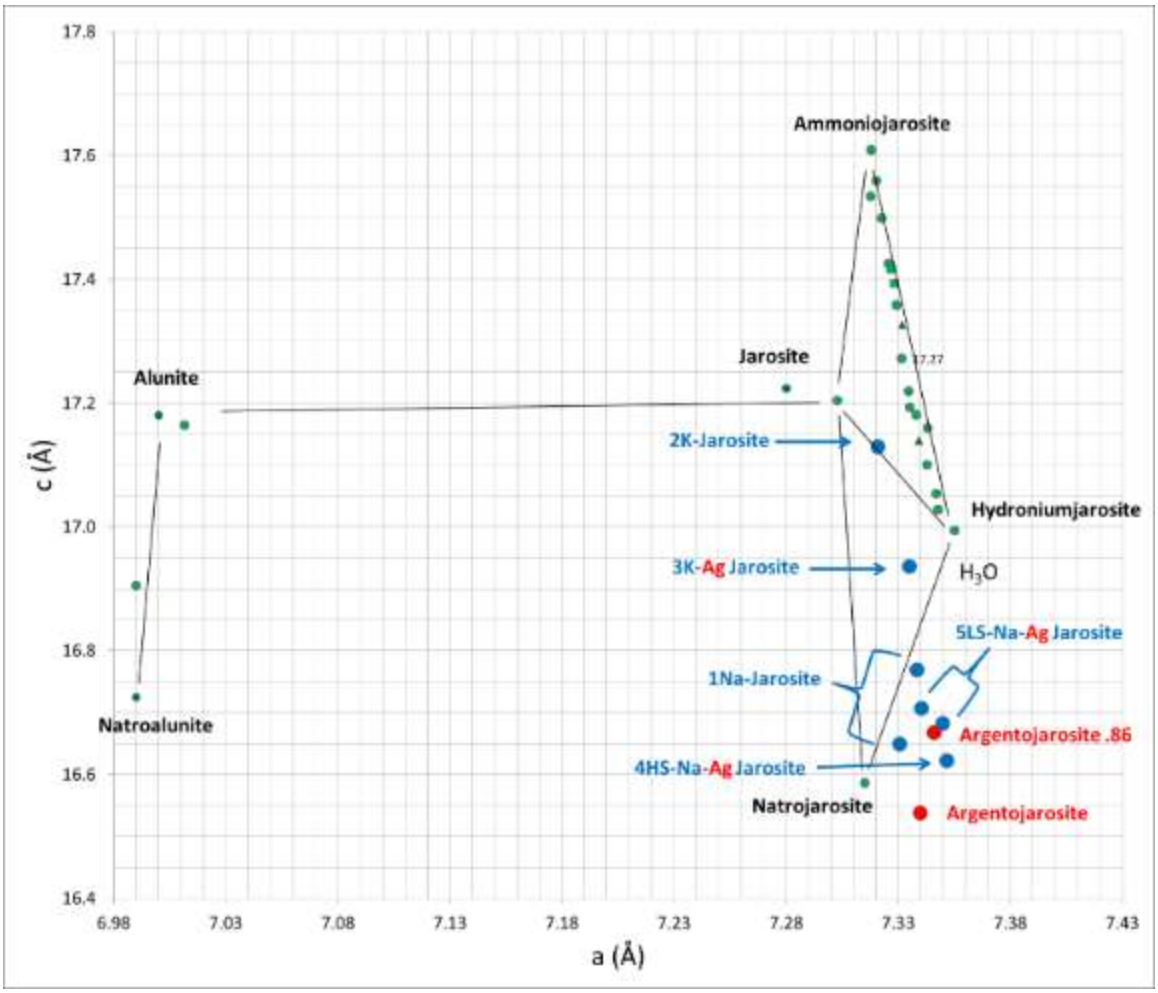


Figure 8-11: Unit cell parameters a vs c of various alunite group solid-solution compositions. Results provided by the Dept. of Earth, Ocean, & Atmospheric Sciences at the University of British Columbia.

Green points are published values for non-silver jarosites

Red points are published data for argentojarosite.

Blue points are from this thesis:

1Na-Jarosite (Baseline sodium)

5LS-Na-Ag (Low-silver sodium)

4HS-Na-Ag (High-silver Sodium)

2K (Baseline potassium)

3K-Ag (High-silver potassium)

## 8.3 Surfactant Adsorption Densities as a Function of Residual Surfactant Concentration

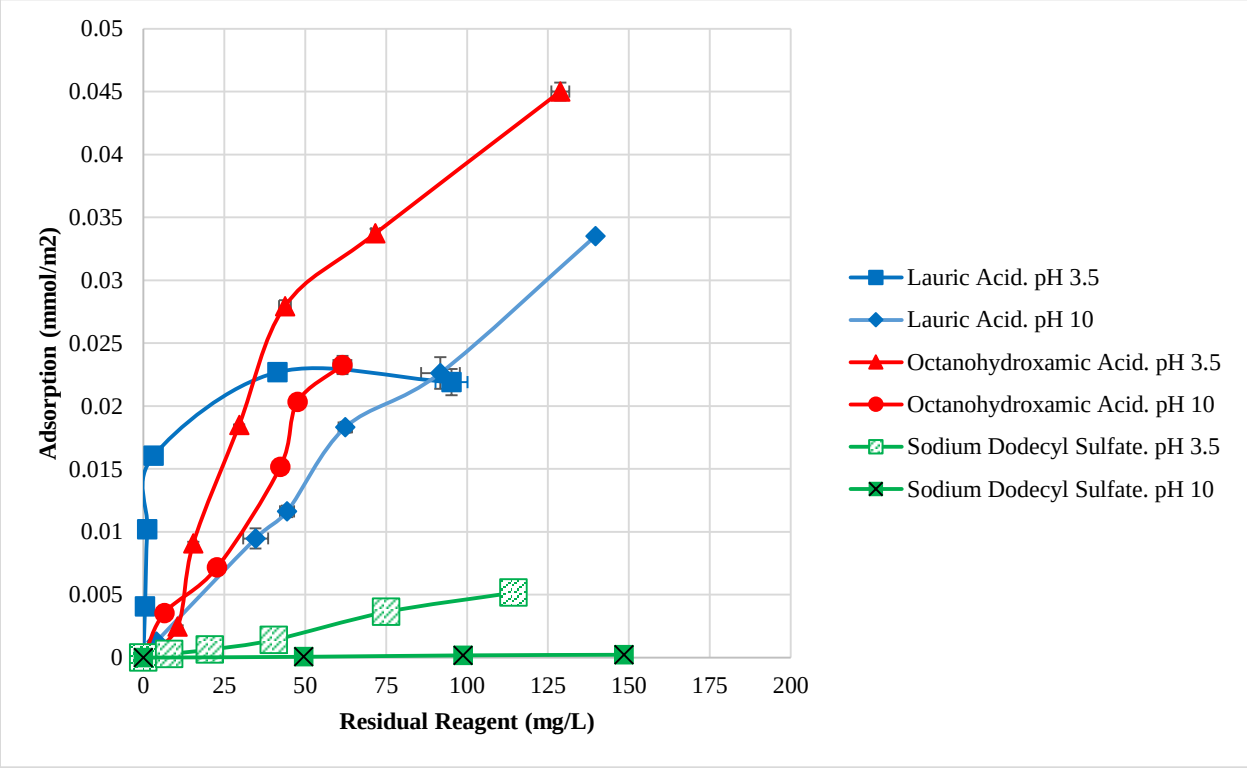


Figure 8-12: Surfactant Adsorption Results for Baseline Sodium Jarosite (Residual Concentrations).

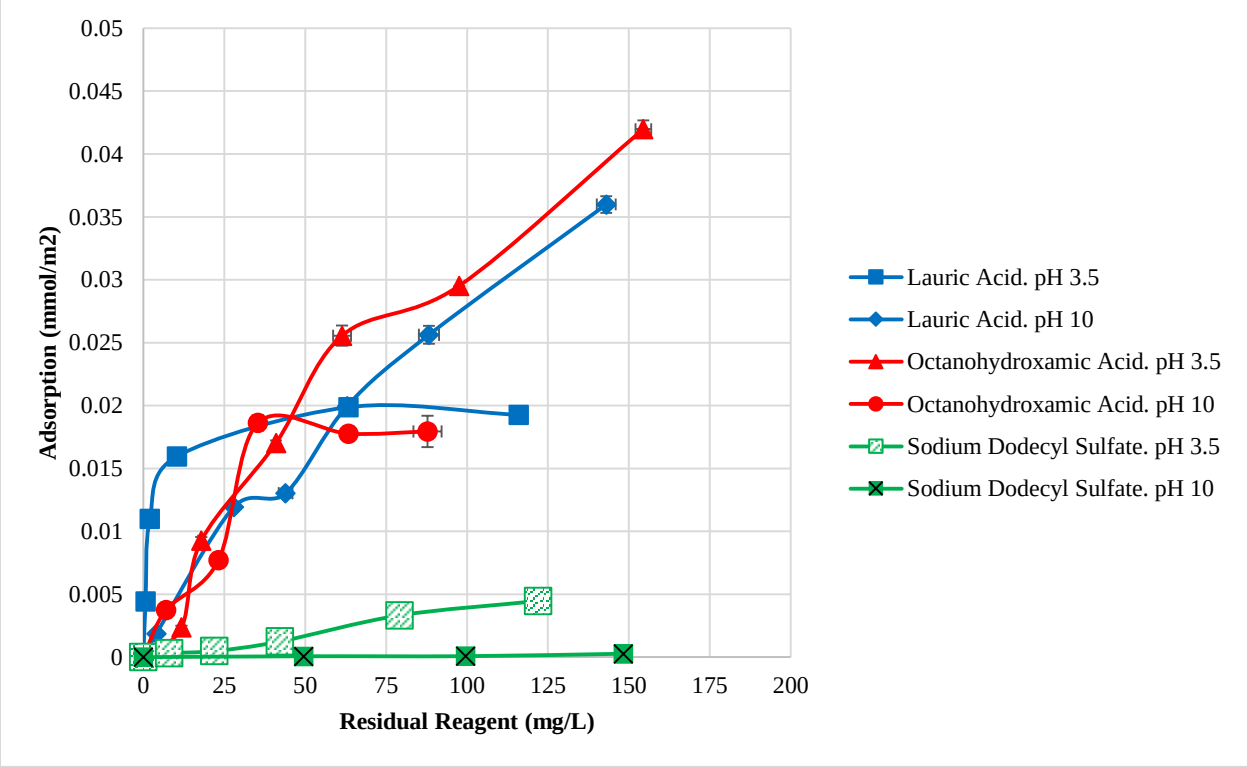


Figure 8-13: Surfactant Adsorption Results for Low-Ag Sodium Jarosite (Residual Concentrations).

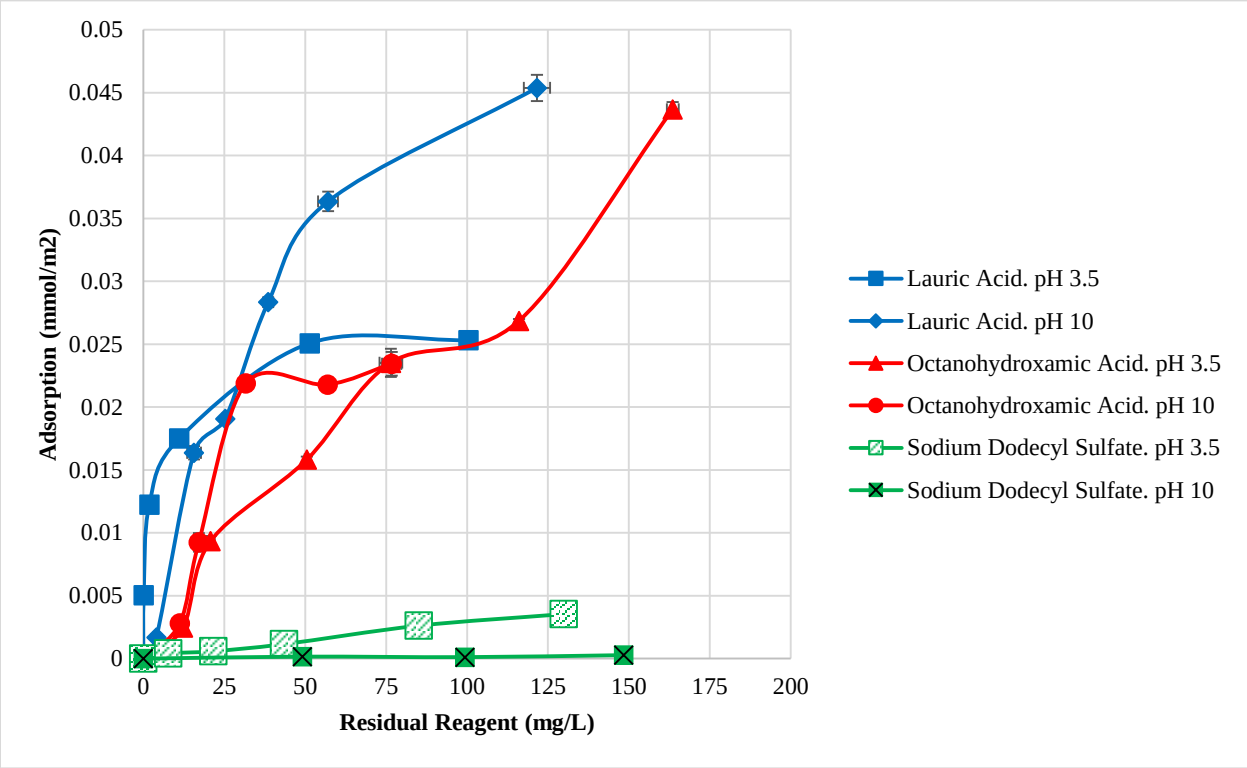


Figure 8-14: Surfactant Adsorption Results for High-Ag Sodium Jarosite (Residual Concentrations).

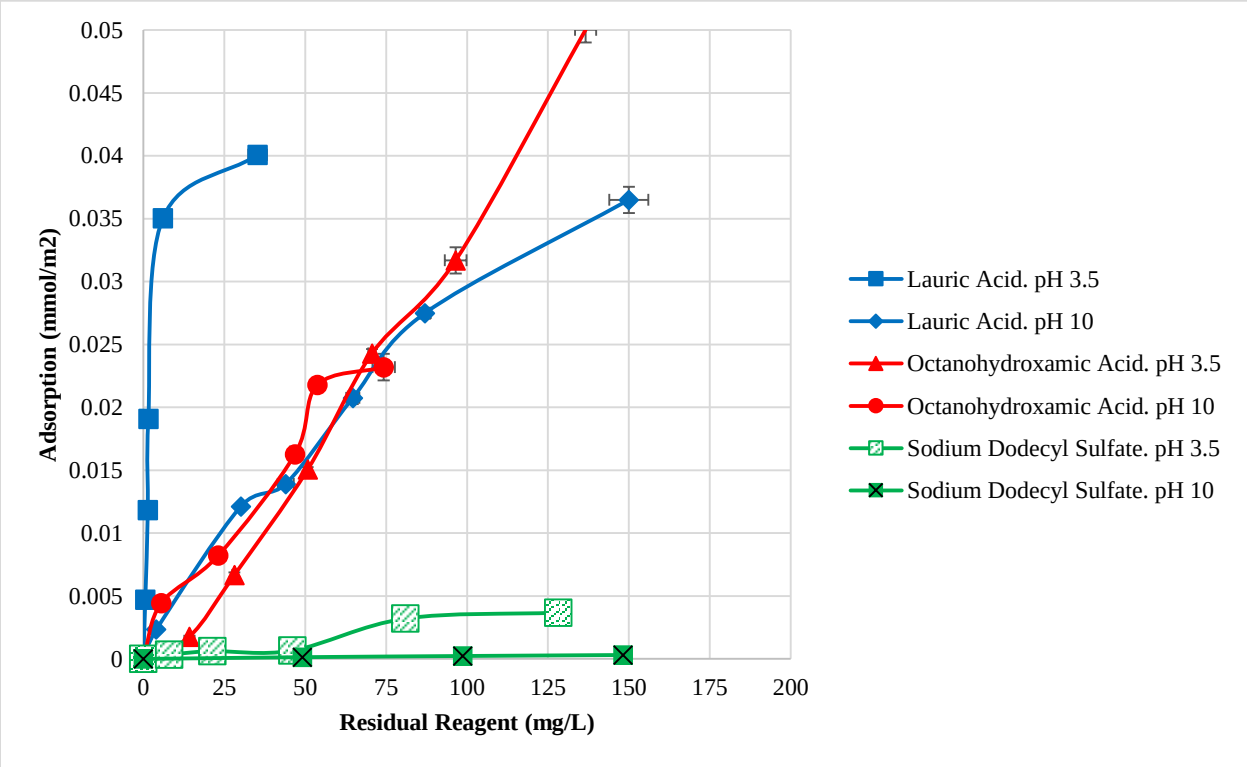


Figure 8-15: Surfactant Adsorption Results for Baseline Potassium Jarosite (Residual Concentrations).

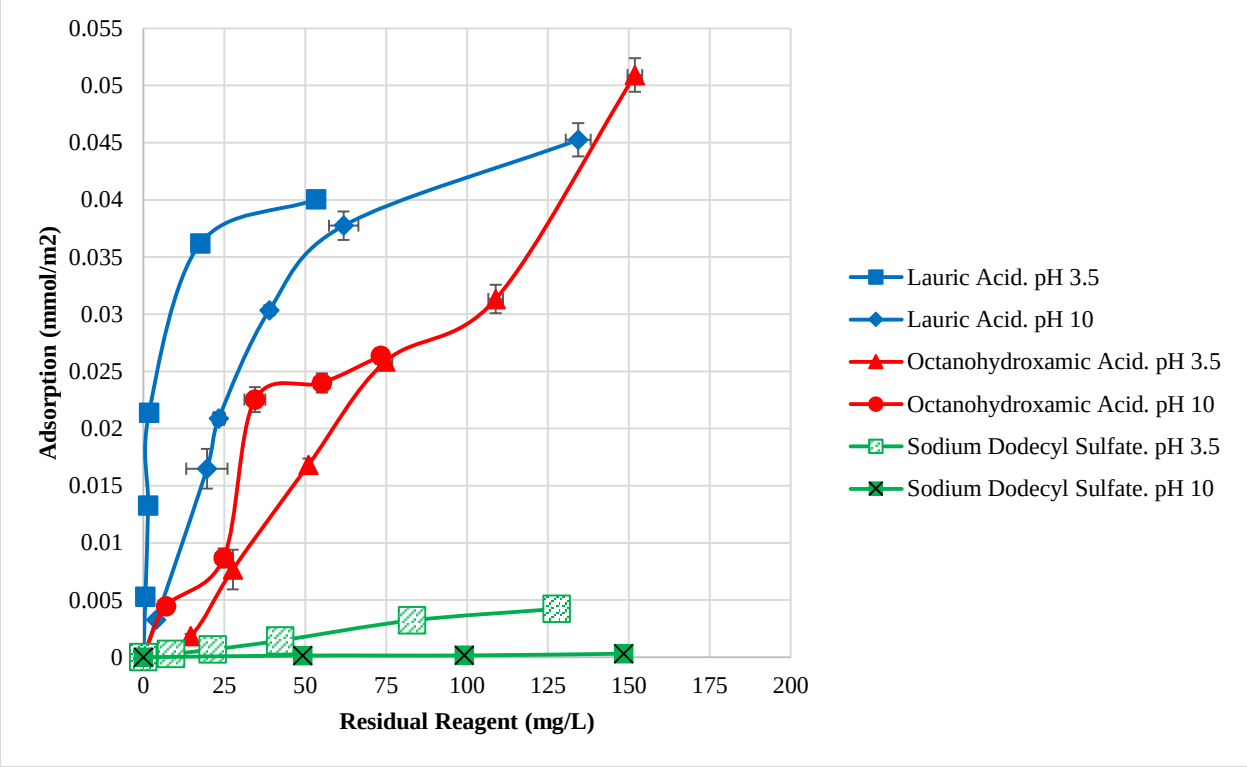


Figure 8-16: Surfactant Adsorption Results for High-Ag Potassium Jarosite.